PULSE PROPAGATION IN HIGH-SPEED DIGITAL CIRCUITS

FINAL REPORT

for

Contract No. N00014-85-K-0619

Office of Naval Research
Department of the Navy
800 North Quincy Street
Arlington, Virginia 22217

Prepared by

R. Mittra

Electromagnetic Communication Laboratory
Department of Electrical and Computer Engineering
Engineering Experiment Station
University of Illinois at Urbana-Champaign
Urbana, Illinois 61801-2991

May 1989

UILU-ENG-89-2541

Electromagnetic Communication Laboratory Report No. 89-3

PULSE PROPAGATION IN HIGH-SPEED DIGITAL CIRCUITS

Final Report

for

Contract No. N00014-85-K-0619

Office of Naval Research
Department of the Navy
800 North Quincy Street
Arlington, Virginia 22217

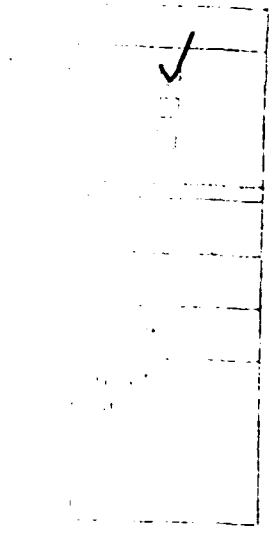

May 1989

A-1

Prepared by

R. Mittra

Electromagnetic Communication Laboratory
Department of Electrical and Computer Engineering
Engineering Experiment Station
University of Illinois at Urbana-Champaign
Urbana, Illinois 61801-2991

UNCLASSIFIED
SECURITY CLASSIFICATION OF THIS PAGE

REPORT DOCUMENTATION PAGE

1a. REPORT SECURITY CLASSIFICATION	1b. RESTRICTIVE MARKINGS
2a. SECURITY CLASSIFICATION AUTHORITY	3. DISTRIBUTION/AVAILABILITY OF REPORT
2b. DECLASSIFICATION/DOWNGRADING SCHEDULE	UNLIMITED
4. PERFORMING ORGANIZATION REPORT NUMBER(S) UILU-ENG-89-2541 EMC 89-3	5. MONITORING ORGANIZATION REPORT NUMBER(S)
6a. NAME OF PERFORMING ORGANIZATION University of Illinois at Urbana-Champaign 6b. OFFICE SYMBOL (*If applicable*)	7a. NAME OF MONITORING ORGANIZATION Office of Naval Research Detachment Chicago
6c. ADDRESS (*City, State, and ZIP Code*) 1406 W. Green St. Urbana, IL 61801	7b. ADDRESS (*City, State, and ZIP Code*) 536 S. Clark St. Chicago, IL 60605-1588
8a. NAME OF FUNDING/SPONSORING ORGANIZATION Department of Navy Office of Naval Research 8b. OFFICE SYMBOL (*If applicable*)	9. PROCUREMENT INSTRUMENT IDENTIFICATION NUMBER
8c. ADDRESS (*City, State, and ZIP Code*) 800 N. Quincy St. Arlington, VA	10. SOURCE OF FUNDING NUMBERS PROGRAM ELEMENT NO. / PROJECT NO NR 613-006 / TASK NO / WORK UNIT ACCESSION NO

11. TITLE (*Include Security Classification*)
PULSE PROPAGATION IN HIGH-SPEED DIGITAL CIRCUITS

12. PERSONAL AUTHOR(S)
R. Mittra

13a. TYPE OF REPORT	13b. TIME COVERED	14. DATE OF REPORT (*Year, Month, Day*)	15. PAGE COUNT
Final	FROM 5-3-85 TO 4-31-89	May 8, 1989	122

16. SUPPLEMENTARY NOTATION

17. COSATI CODES			18. SUBJECT TERMS (*Continue on reverse if necessary and identify by block number*)
FIELD	GROUP	SUB-GROUP	Digital circuits, Pulse propagation, Electromagnetic modeling, Printed circuit boards, Microstrip lines and discontinuities

19. ABSTRACT (*Continue on reverse if necessary and identify by block number*)

In this effort, we have developed several techniques for the computation of the characteristic impedance as well as capacitance and inductance matrices for a number of different types of transmission-line constructions, e.g., stripline, microstrip line, buried microstrip line and orthogonal line. We have also investigated methods for measuring the high frequency characteristics of planar transmission lines which may, in general, be lossy. The capacitance and inductance matrices have been employed in a computer program that analyzes an n-line system terminated with digital devices, both for the lossless and lossy cases.

The finite element method and the method of moments have been applied to the problem of computing the equivalent circuits of connectors, interconnects and other discontinuities in planar transmission lines, e.g., the bend, the tapered line and the through-hole via.

(continued on back...)

20. DISTRIBUTION/AVAILABILITY OF ABSTRACT	21. ABSTRACT SECURITY CLASSIFICATION
☒ UNCLASSIFIED/UNLIMITED ☐ SAME AS RPT. ☐ DTIC USERS	Unclassified

22a. NAME OF RESPONSIBLE INDIVIDUAL	22b. TELEPHONE (*Include Area Code*)	22c. OFFICE SYMBOL
R. Mittra	217-333-1202	

DD FORM 1473, 84 MAR 83 APR edition may be used until exhausted. All other editions are obsolete

SECURITY CLASSIFICATION OF THIS PAGE
UNCLASSIFIED

19. Abstract (continued)

These equivalent circuits have been used to predict the pulse propagation in pc boards involving sections of uniform lines combined with discontinuities mentioned above.

TABLE OF CONTENTS

* (All appendices have their own pagination.)

I. INTRODUCTION

This final report summarizes the progress made on research related to the problem of "Pulse Propagation in High Speed Digital Circuits" covering the period of September 1, 1985 to March 31, 1989.

II. PERSONNEL

Dr. R. Mittra, Professor of Electrical Engineering
Dr. C. Chan, Visiting Assistant Professor
Mr. J. Schutt-Aine, Visiting Assistant Professor
Dr. Z. Pantic, Research Associate
Mr. A. Ali, Air Force Fellow
Mr. Paul Aoyagi, Graduate Teaching Assistant
Mr. T. Blazeck, Graduate Research Assistant
Mr. S. Castillo, Graduate Research Assistant
Mr. Woo-Sung Chi, Graduate Teaching Assistant
Mr. U. Feldman, Graduate Research Assistant
Mr. P. Harms, Graduate Research Assistant
Mr. A. Khebir, Graduate Research Assistant
Mr. A. Kouki, Graduate Student
Mr. M. Mehalic, Air Force Fellow
Mr. G. Salo, Graduate Research Assistant
Mr. J. Sutton, Graduate Research Assistant
Mr. G. Wilkins, Graduate Student Fellow

III. TECHNICAL

A. QUASISTATIC AND FREQUENCY-DEPENDENT ANALYSIS OF DIFFERENT TRANSMISSION-LINE CONFIGURATIONS

We have developed techniques for the computation of the characteristic impedance as well as capacitance and inductance matrices for a number of different types of transmission-line constructions, e.g., stripline, microstrip line, buried microstrip line and orthogonal line. The

numerical techniques we have employed employ the FFT algorithm combined with the iterative techniques and are considerably more efficient than those based upon the conventional moment method that require the inversion of large matrices. The algorithms have been extended to the frequency-dependent case by using full-field solution of Maxwell's equations, rather than the quasi-static approximation.

We have also investigated two experimental techniques for measuring the high frequency characteristics of planar transmission lines which may, in general, be lossy. In this approach, the line parameters, viz., R, L, G and C,are obtained by using an algorithm for reducing these parameters from the S-parameter measurements carried out with a Network Analyzer.

B. FINITE ELEMENT ANALYSIS OF TRANSMISSION LINES

We have developed a general purpose, finite element (FEM) analysis which is capable of handling transmission lines of arbitrary cross-section and with arbitrary fillings. The FEM program requires a mesh generation algorithm. A simple mesh program, that is portable in nature, was developed by us for use with the program. However, we have found that it is more expedient to acquire a commercial version of the mesh generation program, e.g., PATRAN, and combine it with our FEM programs for solving either Laplace's or Maxwell's equations.

The FEM approach calls for a method for mesh truncation whenever open-region problems are analyzed using this method. We have developed an absorbing boundary condition for mesh truncation and have applied it to single and multi-conductor transmission lines. The approach is described in Attachment A.

C. PULSE PROPAGATION AND CROSSTALK IN MULTICONDUCTOR LINES WITH LOSSES

We have generalized the analysis of lossless n-lines, terminated with digital devices, to the lossy case using two different approaches. In the first approach, the frequency-domain Green's function method is used in the transmission line part of the circuit, which is linear, in conjunction

with a nonlinear analysis of the terminating circuits, that include digital devices, directly in the time domain. The line is characterized by per unit values of resistance (r), inductance (1), conductance (g) and capacitance (c). If desired, r can be made to vary with frequency to model the skin effect and g can also be a variable of frequency. The terminal networks that model the nonlinear digital devices consist of capacitors in parallel with nonlinear voltage-controlled resistors.

We have prepared a report (see Attachment B) describing this analysis and have appended it herewith.

The second approach we have developed for the time-domain simulation of n-line structures terminated by logic gate inverters, is based on a state-space approach employed in conjunction with the Scattering Matrix representation of the coupled n-lines. It is designed to treat both the lossless and lossy line cases and has been described in a recent publication a copy of which is appended in Attachment C.

D. CONNECTOR, INTERCONNECT AND DISCONTINUITY MODELING

The finite element method, as well as other analytical and numerical techniques, are being investigated with the objective of modeling connectors, interconnects and discontinuities introduced by a change in the conductor width or the presence of a stub, etc. In general, the connector, the via, and similar other discontinuity problems must be modeled by using a three-dimensional mesh generation program; hence, such modeling is computer intensive. The connector problem has been investigated using the full 3-D mesh and with an approximate 2-D model. It has been shown that in some cases it is possible to use the 2-D approximation, though this is not universally true. A comprehensive report on the connector that describes the analysis, numerical results and the experimental verification of these results has been prepared and a paper summarizing the research has been submitted for publication.

An alternative approach, based on the method of moments (MoM) has been employed for both the bend and the via problems. Numerical results for the inductance and capacitance matrices have been obtained for the single and multiple line bends in microstrip lines. The modeling of of

the via problem is being continued.

Another discontinuity problem being investigated in this effort is the tapered-line problem, which arises in the modeling of interconnects, and has been analyzed using a perturbational approach. Both single and multiple lines with arbitrary tapers have been investigated using the scattering matrix approach. Experimental verification of the theoretical results is currently being carried out.

IV. REFERENCES

Journal Articles

1. Jose E. Schutt-Aine and R. Mittra, "Analysis of pulse propagation in coupled transmission lines," IEEE Trans. on Circuits and Systems, vol. CAS-32, no. 12, pp. 1214-1219, December 1985.

2. R. Mittra and C. Chan, "Iterative approaches to the solution of electromagnetic boundary value problems," Electromagnetics, vol. 5, no. 2-3, pp. 123-146, 1985.

3. E. Farr, C. Chan and R. Mittra, "A frequency-dependent coupled-mode analysis of multiconductor microstrip lines with application to VLSI interconnection problems," IEEE Trans. on Microwave Theory and Techniques, vol. MTT-34, no. 2, pp. 307-310, February 1986.

4. Z. Pantic and R. Mittra, "Quasi-TEM analysis of microwave transmission lines by the finite-element method," IEEE Trans. on Microwave Theory and Techniques, vol. MTT-34, no. 11, pp. 1096-1103, November 1986.

5. C. H. Chan and R. Mittra, "Analysis of a class of cylindrical multiconductor transmission lines using an iterative approach," IEEE Trans. on Microwave Theory and Techniques, vol. MTT-35, no. 4, pp. 415-424, April 1987.

6. C. H. Chan and R. Mittra, "Comparative study of iterative techniques, moment method and spectral Galerkin approach for solving the problem of electro-magnetic scattering by a rectangular plate," IEE Fifth International Conference on Antennas and Propagation ICAP 87, pp. 443-446, held in York, March 30 - April 2, 1987.

7. C. Chan and R. Mittra, "Analysis of MMIC structures using an efficient iterative approach," IEEE Trans. Microwave Theory & Techniques, vol. MTT-36, no. 1, pp. 96-105, January 1988.

8. J. E. Schutt-Aine and R. Mittra, "Scattering parameter transient analysis of transmission lines loaded with nonlinear terminations," IEEE Trans. Microwave Theory & Techniques, vol. MTT-36, no. 3, pp. 529-536, March 1988.

9. C. H. Chan and R. Mittra, "The propagation characteristics of signal lines embedded in a multilayered structure in the presence of a periodically perforated ground plane," IEEE Trans. Microwave Theory & Techniques, vol. MTT-36, no. 6, pp. 968-975, June 1988.

10. Z. Pantic and R. Mittra, "Calculation of characteristic impedance of planar, inhomogeneous transmission lines for digital circuit applications," AEU, Band 42, Heft 5, pp. 325-327, Sept./Oct. 1988.

11. Q. Xu, K. J. Webb and R. Mittra, "Study of modal solution procedures for microstrip step discontinuities," IEEE Trans. Microwave Theory and Techniques, vol. MTT-37, no. 2, pp. 381-387, February 1989.

Technical Reports

1. U. Feldman and R. Mittra, "Characterization of microstrip discontinuities," EMC Technical Report, No. 85-6, University of Illinois, September 1985.

2. G. R. Salo and R. Mittra, "The modeling of connectors for printed circuit boards," EMC Technical Report, No. 85-7, University of Illinois, October 1985.

3. Z. Pantic and R. Mittra, "Quasi-TEM analysis of microwave transmission lines by the finite-element method," DAAG 29-85-K-0183, EMC Report No. 86-2, February 1986.

4. A. S. Ali and R. Mittra, "Time-domain reflectometry using scattering parameters and a de-embedding application," N00014-85-K-0619, EMC Report No. 86-4, May 1986.

5. J. R. Sutton and R. Mittra, "Computer-aided design of nonlinear networks with N-conductor transmission lines systems," N00014-85-K-0619 and Fellowship Grant from Northrop Corporation , EMC Report No. 86-8, November 1986.

6. P. H. Harms and R. Mittra, "Modeling of planar transmission line structures for digital circuit applications," N00014-85-K-0619, EMC Report No. 86-9, November 1986.

7. Z. Pantic and R. Mittra, "Full-wave analysis of isolated and coupled microwave transmission lines using the finite element method," DAAG29-85-K-0183, EMC Report No. 87-1, February 1987.

8. J. E. Schutt-Aine and R. Mittra, "Scattering parameter transient analysis of transmission lines loaded with nonlinear terminations," N00014-85-K-0619, EMC Report No. 87-2, March 1987.

9. S. P. Castillo and R. Mittra, "Electromagnetic modeling of high-speed digital circuits," N00014-85-K-0619, EMC Report No. 87-3, June 1987.

To Be Published

1. S. P. Castillo and R. Mittra, "Analysis of N-conductor transmission line system terminated with non-linear digital devices," submitted to Electromagnetic Compatibility

2. S. Castillo, Z. Pantic and R. Mittra, "Finite element analysis of multiconductor printed circuit transmission lines systems," submitted to MTT.

Thesis

1. "The modeling of connectors for printed circuit boards," Glen R. Salo, M.S. Thesis, May 1985.

2. "Characterization of microstrip discontinuities in the time and frequency domains," Uri Feldman, M. S. Thesis, June 1985.

3. "Time-domain reflectometry using scattering parameters and a de-embedding application," Azar Ali, M. S. Thesis, May 1986.

4. "Computer-aided design of nonlinear networks with N-conductor transmission line systems," J. R. Sutton, M. S. Thesis, November 1986.

5. "Modeling of planar transmission line structures for digital circuit applications," P. H. Harms, M. S. Thesis, November 1986.

6. "Investigation of Iterative and spectral Galerkin Techniques for Solving Electromagnetic Boundary Value Problems," C. H. Chan, Ph.D. Thesis, May 1987.

7. "Electromagnetic Modeling of High-Speed Digital Circuits," S. P. Castillo, Ph.D. Thesis, May 1987.

8. "Transient Analysis of Lossy Multiconductor Transmission Lines in Nonlinear Circuits," T. S. Blazeck, Ph.D. Thesis, May 1989.

APPENDIX A

AN ABSORBING BOUNDARY CONDITION FOR QUASI-TEM ANALYSIS OF MICROWAVE TRANSMISSION LINES VIA THE FINITE ELEMENT METHOD

A. Khebir, A. B. Kouki, and R. Mittra

Electromagnetic Communication Laboratory

Electrical & Computer Engineering Department

University of Illinois

Urbana, IL 61801

Abstract

Open microwave transmission line structures are analyzed in this paper in the quasi-TEM regime using the finite element method. An absorbing boundary condition(ABC) for an arbitrary outer boundary is introduced for the purpose of truncating the unbounded region surrounding the transmission line in an efficient manner. The application of the boundary condition is illustrated for three different microstrip line configurations, viz., a single line, two coupled lines, and a six-conductor line. Numerical results are compared with those published elsewhere and good agreement is found.

I. Introduction

Microwave transmission lines have been investigated by many researchers who have employed a variety of methods to study the problem of computing the characteristic impedance and propagation constant along these lines. Some of these techniques include the Fourier transform method [1-2], variational method [3-4], spectral domain method [5-7], Green's function technique [8-13], conformal mapping [14-16], boundary element method [17-18], and finite-element method [19-20]. All but the last two approaches mentioned above are limited to thin strips and/or to structures containing dielectrics with planar interfaces. Although the finite element method method (FEM) is very general, and can handle any arbitrary configuration of conductors and dielectrics, it must deal with the practical problems of mesh truncation and the need for a large number of mesh nodes when applied to an open region problem. One approach to circumventing this difficulty is to truncate the mesh by introducing a fictitious conducting enclosure[19, 21]. This approach yields satisfactory results only if the actual field decays sufficiently well as it reaches the outer boundary. Typically, this requires one to recede the outer boundary far away from the structure in order to achieve acceptable accuracy and, this, in turn, results in a large mesh. An alternative approach is to use "infinite" elements [20], that extend to infinity, and cover the region outside of a fictitious boundary surrounding the structure. Although superior to the artificial p.e.c boundary method, this approach nonetheless has its own drawbacks. First, the infinite elements require special care during the filling of the FEM matrix. Second, one needs to assume a certain asymptotic behavior of the field within the infinite elements, and this behavior may not be convenient to obtain.

In this paper, we introduce an absorbing boundary condition(ABC) which provides us with an efficient means for dealing with the open region problems in the quasi-static regime. This absorbing boundary condition does not suffer from the complications associated with the infinite elements, and yet enables us to bring the outer boundary much closer to the structure

than would be possible with the p.e.c. artificial boundary. Furthermore, unlike many of the available ABC's that are restricted to separable outer boundaries, the one presented in this paper is useful for an arbitrarily-shaped outer boundary. We will demonstrate the versatility of this new absorbing boundary condition by considering the examples of one, two, and six conductor microstrip lines.

II. Derivation of the Absorbing Boundary Condition

Figure 1 depicts the geometry of an open region problem consisting of N arbitrarily-shaped conductors embedded in a multilayered medium above a ground plane. Let Ω_T denote the region exterior to the conductors. For the finite mathematics techniques [22-23], the unbounded outer region Ω_T must be truncated and enclosed with an outer boundary Γ_2. The strategy for deriving an absorbing boundary condition is to find an operator which, when applied on the outer boundary, would mimic the asymptotic behavior of the wave function at infinity and would thus yield accurate results in the interior region without the need of an exorbitantly large number of mesh points. The problem at hand can be described in terms of the following set of equations:

$$\nabla^2 u = 0 \qquad \text{in } \Omega_T \tag{1}$$

$$u = g_i \text{ on the } i^{th} \text{ conductor} \tag{2}$$

$$B_m u = 0 \text{ on } \Gamma_2 \tag{3}$$

where u is the potential function and B_m is the m^{th} order absorbing boundary condition operator.

An asymptotic form of the solution, valid for large ρ can be written as:

$$u(\rho,\phi) = \sum_{n=1}^{\infty} \frac{a_n}{\rho^n} \cos n\phi \tag{4}$$

Equation (4) can be used to obtain an absorbing boundary condition on an artificial boundary. Manipulating (4) one can obtain the first-order absorbing boundary condition operator, which reads

$$B_1 u \equiv \frac{\partial u}{\partial \rho} + \frac{u}{\rho} = O\left(\frac{1}{\rho^3}\right) \tag{5}$$

Similarly, the second-order absorbing boundary condition operator takes the form

$$B_2 u \equiv \left(\frac{\partial}{\partial \rho} + \frac{3}{\rho}\right)\left(\frac{\partial u}{\partial \rho} + \frac{u}{\rho}\right) = O\left(\frac{1}{\rho^5}\right) \tag{6}$$

As will be seen later, the finite element formulation of the problem involves an integral over the outer boundary, Γ_2, and the normal derivative of u appears in this integrand. Hence, for our purposes, it it is more desirable to find an asymptotic representation for the normal derivative of u rather than make direct use of the operator B_2. For a circular outer boundary, the normal derivative will simply be the radial one which can readily be obtained from (6). Mittra and Ramahi [30] have presented a procedure for deriving an absorbing boundary condition operator for the dynamic case in terms of the field and its second-order angular derivative that can be conveniently adapted to the quasi-static case of interest here. We begin by expressing the radial derivative of u in a manner similar to the one described in [30]. Next, we use (1) to exchange the second-order derivative in ρ, $u_{\rho\rho}$, with the second-order angular derivative, $u_{\phi\phi}$, to obtain the desired absorbing boundary condition:

$$u_\rho = \alpha(\rho)\, u + \beta(\rho)\, u_{\phi\phi} \tag{7}$$

where $\alpha(\rho)$ and $\beta(\rho)$ are given by

$$\alpha(\rho) = -\frac{2}{3\rho} \tag{8}$$

$$\beta(\rho) = \frac{1}{3\rho} \tag{9}$$

For a general, noncircular outer boundary it is necessary to generalize (7) and derive an expression for the normal derivative operator u_n in the local coordinate system (t,n) where t and n are tangent and normal to the boundary, respectively. An approximate expression for this derivative can be obtained by following the procedure described in [24] and is given by

$$\frac{\partial u}{\partial n} = \overline{\alpha}\, u + \overline{\gamma}\, u_t + \overline{\beta}\, u_{tt} \tag{10}$$

where

$$\overline{\alpha} = (x_0 \sin\theta_0 - y_0 \cos\theta_0)\left(-\frac{2}{3\rho^2}\right) \tag{11}$$

$$\overline{\gamma} = \frac{-t\,(x_0 \sin\theta_0 - y_0 \cos\theta_0) + \frac{1}{2}\sin 2\theta_0\,(y_0^2 - x_0^2) + x_0 y_0 \cos 2\theta_0}{\rho^2} \tag{12}$$

$$\overline{\beta} = (x_0 \sin\theta_0 - y_0 \cos\theta_0)^3\left(\frac{1}{3\rho^2}\right) \tag{13}$$

$$\rho = \sqrt{t^2 + x_0^2 + y_0^2 + 2t\,(x_0 \cos\theta_0 + y_0 \sin\theta_0)} \tag{14}$$

and θ_0, x_0, y_0, and t are as shown in Fig. 2.

III. Finite Element Implementation of the Absorbing Boundary Condition

The problem at hand is to solve for the potential u satisfying the Laplace's equation:

$$\nabla\cdot(\varepsilon\nabla u) = 0 \tag{15}$$

Multiplying (15) by a testing function v and integrating over the domain of the problem Ω_T, we obtain

$$\int_{\Omega_T} v\, \nabla\cdot(\varepsilon\nabla u)\, ds = 0 \tag{16}$$

From Green's identity we have

$$\int_{\Omega_T} v\,\nabla\cdot(\varepsilon\nabla u)\,ds = -\int_{\Omega_T} \varepsilon\nabla u\cdot\nabla v\,ds + \int_{\Gamma_2} v\,\varepsilon\frac{\partial u}{\partial n}\,dt \qquad (17)$$

Inserting the above in (16), we get

$$\int_{\Omega_T} \varepsilon\nabla u\cdot\nabla v\,ds = \int_{\Gamma_2} v\,\varepsilon\frac{\partial u}{\partial n}\,dt \qquad (18)$$

In the finite element formulation, one sets up a mesh in the region Ω_T, typically using triangular elements. The edges of the outermost elements prescribe Γ_2. Hence, considering one element at a time, the absorbing boundary condition given in (10) may be incorporated into (18) to yield

$$\int_{\Omega_T} \varepsilon\nabla u\cdot\nabla v\,ds = \int_{\Gamma_2} v\,\varepsilon\,(\overline{\alpha}\,u + \overline{\gamma}\,u_t + \overline{\beta}\,u_{tt})\,dt \qquad (19)$$

Since ε is constant over each element, we can integrate (19) by parts to obtain

$$\int_{\Omega_T} \varepsilon\nabla u\cdot\nabla v\;\,ds = \int_{\Gamma_2} \varepsilon\,(\overline{\alpha}\,vu + \overline{\gamma}\,vu_t - \overline{\beta}\,v_t u_t - \overline{\zeta}\,vu_t)\,dt \qquad (20)$$

where

$$\overline{\zeta} = (x_0\sin\theta_0 - y_0\cos\theta_0)^3(t + x_0\cos\theta_0 + y_0\sin\theta_0)\left(-\frac{2}{3\rho^4}\right) \qquad (21)$$

The form given in (20) is well-suited for numerical implementation for any arbitrary conductor configuration enclosed by any arbitrarily-shaped outer boundary.

IV. Numerical Results

a. One Conductor

The microstrip line, shown in Fig. 3, is enclosed by a rectangular outer boundary. We first solved the potential problem by applying the absorbing boundary condition, given in equation (7), on a rectangular outer boundary. Next, we introduced a perfectly electric conducting shield at the outer boundary and solved the problem once again using the same mesh. As Table 1 indicates, the relative error between the absorbing boundary condition and the published results [12, 26, 27] is between 0.053 and 2.56 percent, whereas the error between the shield and the published results is between 14.55 and 30.04 percent.

b. Two conductors:

Two coupled microstrips, shown in Fig. 4, are enclosed by a rectangular outer boundary. Table 2 presents some results for the same problem that have been published elsewhere[12, 28, 29], together with those obtained by using a p.e.c. shield and the absorbing boundary condition in (10). The relative error in the self-terms is 0.27 percent for the absorbing boundary condition and 18.31 percent for the shield. Likewise, the error in the mutual terms is 5.2 percent for the absorbing boundary condition and 44.59 percent for the shield.

c.Six conductors:

The six conductor system, shown in Fig. 5, is enclosed, once again, by a rectangular outer boundary. To the best of our knowledge, there are no published results for this configuration. However, we have compared our results with those derived by using the computer program developed by Chan [25], which uses an integral equation formulation and an iterative method of solution. As Table 3 indicates, the relative error for the capacitance matrix is between 0.84 and 14.52 percent for the absorbing boundary condition and between

3.96 and 74.10 percent for the p.e.c shield when compared to the results obtained with the iterative solution. For the inductance matrix, the error is between 0.02 and 11.46 percent for the absorbing boundary condition and between 39.74 and 96.72 percent for the p.e.c shield. In addition, the relative error between the absorbing boundary condition and the shield reached 69.69 percent in the capacitance matrix and 97.01 percent in the inductance matrix.

In all of the three numerical examples considered thus far, we have chosen a rectangular outer boundary because it facilitates the meshing procedure and because it is conformal to the structures considered. This meshing is done in a manner such that none of the triangular elements have more than one edge on the outer boundary. Since the finite element scheme considers one element at a time, the problem of the undefined normal at the rectangular corners is circumvented when the procedure described above is followed.

In order to illustrate the fact that the formulation described in this paper is also applicable to an arbitrary outer boundary, we reconsider the two-conductor example described earlier. Figure 6 illustrates the coupled microstrips problem with an arbitrary outer boundary. Table 4 shows that the results obtained for this case are almost identical to those derived with the rectangular boundary.

Finally, before closing, we point out that no special treatment is needed at the dielectric interfaces because in the finite element formulation the medium is modeled as being homogeneous within each element and, consequently, the line integral in equation (20) is always confined to within a homogeneous region inside the element.

V. Conclusions

We have shown how an absorbing boundary condition for quasi-static fields can be applied to a potential field at distances quite close to a transmission line configuration to derive

an FEM-based solution in a numerically efficient manner. It is evident from the numerical results that the absorbing boundary condition consistently yields more accurate results than those obtainable with a perfectly conducting shield placed at the same location. However, in some situations, the accuracy obtained with the approximate ABC presented in this paper may still not be adequate, as for instance in the off-diagonal terms of the capacitance matrix in the six-conductor configuration. This aspect of the problem is being investigated further by attempting to derive improved versions of the absorbing boundary condition. Also planned is an extension to the full-wave FEM formulation where a dynamic version of the absorbing boundary condition is needed.

References:

[1] R. Mittra and T. Itoh, "Charge and potential distributions in shielded striplines," **IEEE Trans. Microwave Theory Tech.**, vol. MTT-18, pp. 149-156, Mar. 1970.

[2] A. El-Sherbiny, "Exact analysis of shielded microstrip lines and bilateral fin lines," **IEEE Trans. Microwave Theory Tech.**, vol. MTT-29, pp. 669-675, July 1981.

[3] E. Yamashita and R. Mittra, "Variational method for the analysis of microstrip lines," **IEEE Trans. Microwave Theory Tech.**, vol. MTT-16, pp. 251-256, Apr. 1968.

[4] S. K. Koul and B. Bhat, "Generalized analysis of microstrip-like transmission lines and coplanar strips with anisotropic substrates for MIC, electrooptic modulator, and SAW applications," **IEEE Trans. Microwave Theory Tech.**, vol. MTT-31, pp. 1051-1058, Dec. 1983.

[5] T. Itoh and A. S. Herbert, "A generalized spectral domain analysis for coupled suspended microstriplines with tunning septums," **IEEE Trans. Microwave Theory Tech.**, vol. MTT-26, pp. 820-826, Oct. 1978.

[6] T. Itoh, "Generalized spectral domain method for multiconductor printed lines and its application to tunable suspended microstrips," **IEEE Trans. Microwave Theory Tech.**, vol. MTT-26, pp. 983-987, Dec. 1978.

[7] D. M. Syahkal and J. B. Davies, "Accurate solution of microstrip and coplanar structures for dispersion and for dielectric conductor losses," **IEEE Trans. Microwave Theory Tech.**, vol. MTT-27, pp. 694-699, July 1979.

[8] P. Silvester, "TEM wave properties of microstrip transmission lines," **Proc. Inst. Elec. Eng.**, vol. 115, pp. 43-48, Jan. 1968.

[9] T. G. Bryant and T. A. Weiss, "Parameters of microstrip transmission lines and of coupled pairs of microstrip lines," **IEEE Trans. Microwave Theory Tech.**, vol. MTT-16, pp. 1021-1027, Dec. 1968.

[10] E. Yamashita and K. Atsuki, "Analysis of thick-strip transmission lines," **IEEE Trans. Microwave Theory Tech.**, vol. MTT-19, pp. 120-122, Jan. 1971.

[11] R. Crampagne, M. Ahmadpanah, and T. Guirand, "A simple method for determining the Green's function for a large class of MIC lines having multilayered dielectric structures," **IEEE Trans. Microwave Theory Tech.**, vol. MTT-26, pp. 82-87, Feb. 1978.

[12] C. Wei, R. Harrington, L. Mautz, and T. Sarkar, "Multiconductor lines in multilayered dielectric media," **IEEE Trans. Microwave Theory Tech.**, vol. MTT-32, pp. 439-449, Apr. 1984.

[13] R. Mittra and C. Chan, "Iterative approaches to the solution of electromagnetic boundary value problems," **Electromagnetics**, vol. 5, pp. 123-146, 1985.

[14] S. Cohn, "Characteristic impedances of broadside-coupled strip transmission lines," **IRE Trans. Microwave Theory Tech.**, vol. MTT-8, pp. 633-637, Nov. 1960.

[15] T. Chen, "Determination of the capacitance inductance and characteristic impedance of rectangular lines," **IRE Trans. Microwave Theory Tech.**, vol. MTT-8, pp. 510-519, Sept. 1960.

[16] H. A. Wheeler, "Transmission-line properties of parallel strips separated by a dielectric sheet," **IEEE Trans. Microwave Theory Tech.,** vol. MTT-13, pp. 172-185, Mar. 1965.

[17] R. F. Harrington et al.,"Computation of Laplacian potentials by an equivalent source method," **Proc. Inst. Elec. Eng.,** vol. 116, no. 10, pp. 1715-1720, Oct. 1969.

[18] B. E. Spielman, "Dissipation loss effects in isolated and coupled transmission lines," **IEEE Trans. Microwave Theory Tech.,** vol. MTT-25, pp. 648-655, Aug. 1977.

[19] P. Daly, "Hybrid-mode analysis of microstrip by finite-element method," **IEEE Trans. Microwave Theory Tech.,** vol. MTT-19, pp. 19-25, Jan. 1971.

[20] Z. Pantic and R. Mittra, "Quasi-TEM analysis of microwave transmission lines by the finite-element method," **IEEE Trans. Microwave Theory Tech.,** vol. MTT-34, pp. 1096-1103, Nov. 1986.

[21] M. Ikeuchi, H. Sawami, and H. Niki, "Analysis of open-type dielectric waveguides by the finite-element iterative method," **IEEE Trans. Microwave Theory Tech.,** vol. MTT-29, pp. 243-239, Mar. 1981.

[22] B. Engquist and A. Majda, "Absorbing boundary conditions for the numerical simulation of waves," **Math. Comp.,** vol. 31, pp. 629-651, 1977.

[23] S. I. Hariharan, "Absorbing boundary conditions for exterior problems," **ICASE,** ICASE Report-85-33.

[24] A. Khebir, O. Ramahi, and R. Mittra, " An efficient partial differential equation technique for solving the problem of scattering by objects of arbitrary shape," (to appear).

[25] P. H. Harms, C. H. Chan, and R. Mittra, "Modeling of planar transmission line structures for digital circuit applications," (to appear in AEU)

[26] A. Farrar and A. T. Adams, "Characteristic impedance of microstrip by the method of moments," **IEEE Trans. Microwave Theory Tech.**, vol. MTT-18, pp. 65-66, Jan. 1970.

[27] H. Sobol, "Extending IC technology to microwave equipment," **Electronics**, vol. 40, pp. 112-124, Mar 20, 1967.

[28] C. Wei and R. F. Harrington, "Computation of the parameters of multiconductor transmission lines in two dielectric layers above a ground plane," **Dept. Electrical Computer Eng.**, Syracuse Univer., Rep. TR-82-12, Nov. 1982.

[29] W. T. Weeks, "Calculation of coefficients of capacitance of multiconductor transmission lines in the presence of a dielectric interface," **IEEE Trans. Microwave Theory Tech.**, vol. MTT-18, pp. 35-43, Jan. 1970.

[30] R. Mittra and O. Ramahi, " Absorbing boundary conditions for the direct solution of partial differential equations arising in electromagnetic scattering problems," in **Differential Methods in Electromagnetic Scattering**, vol. II, M. Morgan, Ed New York, N.Y.: Elsevier Science, Inc., 1989 (to appear).

w/h	ABC	Shield	Reference [12]	Reference [26]	Reference [27]	Boundary location=d	Error ABC-[27]	Error Shield-[27]
0.4	90.797	62.892	92.278	91.172	89.909	0.65	0.987%	30.049%
0.7	73.000	53.543	73.962	73.613	71.995	0.75	1.396%	25.630%
1.0	62.531	45.650	62.811	62.713	60.970	0.75	2.560%	25.127%
2.0	41.922	34.778	42.998	43.149	41.510	1.20	0.992%	16.218%
4.0	26.047	22.018	26.971	27.301	26.027	1.50	0.077%	15.403%

Table 1a: Characteristic impedance in Ohms for the microstrip line of Fig. 3 ($\varepsilon_r = 6.0$)

w/h	ABC	Shield	Reference [12]	Reference [26]	Reference [27]	Boundary location=d	Error ABC-[27]	Error Shield-[27]
0.4	73.380	51.513	74.897	73.702	73.290	0.65	0.123%	29.713%
0.7	58.955	43.841	59.910	59.379	58.502	0.75	0.774%	25.061%
1.0	50.453	37.395	50.810	50.501	49.431	0.75	2.067%	24.350%
2.0	33.766	28.322	34.674	34.592	33.493	1.20	0.815%	15.439%
4.0	20.917	17.863	21.668	21.763	20.906	1.50	0.053%	14.556%

Table 1b: Characteristic impedance in Ohms for the microstrip line of Fig. 3 ($\varepsilon_r = 9.5$)

	ABC	Shield	Reference [12]	Reference [28]	Reference [29]	Error ABC-[29]	Error Shield-[29]
C(1,1)	0.9249×10^{-10}	0.1091×10^{-9}	0.9165×10^{-10}	0.9017×10^{-10}	0.9224×10^{-10}	0.271%	18.310%
C(1,2)	-0.8061×10^{-11}	-0.4712×10^{-11}	-0.8220×10^{-11}	-0.8059×10^{-11}	-0.8504×10^{-11}	5.203%	44.591%
C(2,1)	-0.8061×10^{-11}	-0.4712×10^{-11}	-0.8220×10^{-11}	-0.8059×10^{-11}	-0.8504×10^{-11}	5.203%	44.591%
C(2,2)	0.9249×10^{-10}	0.1091×10^{-9}	0.9165×10^{-10}	0.9017×10^{-10}	0.9224×10^{-10}	0.271%	18.310%

Table 2: Capacitance matrix for the coupled microstrips of Fig. 4.

Table 3a: Capacitance matrix for the six-condutor structure of Fig. 5.

	Iterative [25]	ABC	Shield	Error ABC-[25]	Error Shield-[25]
C(1,1)	0.668×10^{-10}	0.686×10^{-10}	0.848×10^{-10}	2.620%	26.83%
C(1,2)	-0.279×10^{-10}	-0.315×10^{-10}	-0.264×10^{-10}	13.05%	5.340%
C(1,3)	-0.549×10^{-11}	-0.600×10^{-11}	-0.371×10^{-11}	9.240%	32.56%
C(1,4)	-0.208×10^{-11}	-0.225×10^{-11}	-0.117×10^{-11}	8.320%	43.71%
C(1,5)	-0.999×10^{-12}	-0.101×10^{-11}	-0.456×10^{-12}	0.840%	54.30%
C(1,6)	-0.704×10^{-12}	-0.602×10^{-12}	-0.182×10^{-12}	14.52%	74.10%
C(2,1)	-0.279×10^{-10}	-0.315×10^{-10}	-0.264×10^{-10}	13.05%	5.34%
C(2,2)	0.789×10^{-10}	0.848×10^{-10}	0.876×10^{-10}	7.480%	11.03%
C(2,3)	-0.256×10^{-10}	-0.284×10^{-10}	-0.266×10^{-10}	11.10%	3.960%
C(2,4)	-0.465×10^{-11}	-0.487×10^{-11}	-0.385×10^{-11}	4.740%	17.23%
C(2,5)	-0.173×10^{-11}	-0.181×10^{-11}	-0.122×10^{-11}	4.610%	29.03%
C(2,6)	-0.999×10^{-12}	-0.101×10^{-11}	-0.456×10^{-12}	0.920%	54.30%
C(3,1)	-0.549×10^{-11}	-0.600×10^{-11}	-0.371×10^{-11}	9.240%	32.56%
C(3,2)	-0.256×10^{-10}	-0.284×10^{-10}	-0.266×10^{-10}	11.10%	3.960%
C(3,3)	0.794×10^{-10}	0.855×10^{-10}	0.874×10^{-10}	7.680%	10.14%
C(3,4)	-0.254×10^{-10}	-0.282×10^{-10}	-0.267×10^{-10}	10.91%	4.870%
C(3,5)	-0.465×10^{-11}	-0.487×10^{-11}	-0.385×10^{-11}	4.750%	17.23%
C(3,6)	-0.208×10^{-11}	-0.226×10^{-11}	-0.117×10^{-11}	8.410%	43.71%
C(4,1)	-0.208×10^{-11}	-0.225×10^{-11}	-0.117×10^{-11}	8.320%	43.71%
C(4,2)	-0.465×10^{-11}	-0.487×10^{-11}	-0.385×10^{-11}	4.740%	17.23%
C(4,3)	-0.254×10^{-10}	-0.282×10^{-10}	-0.267×10^{-10}	10.91%	4.870%
C(4,4)	0.794×10^{-10}	0.855×10^{-10}	0.874×10^{-10}	7.680%	10.14%
C(4,5)	-0.256×10^{-10}	-0.284×10^{-10}	-0.266×10^{-10}	11.10%	3.960%

Table 3a (continued): Capacitance matrix for the six-condutor structure of Fig. 5.

	Iterative [25]	ABC	Shield	Error ABC-[25]	Error Shield-[25]
C(4,6)	-0.549×10^{-11}	-0.601×10^{-11}	-0.371×10^{-11}	9.310%	32.56%
C(5,1)	-0.999×10^{-12}	-0.101×10^{-11}	-0.456×10^{-12}	0.840%	54.30%
C(5,2)	-0.173×10^{-11}	-0.181×10^{-11}	-0.122×10^{-11}	4.610%	29.03%
C(5,3)	-0.465×10^{-11}	-0.487×10^{-11}	-0.385×10^{-11}	4.750%	17.23%
C(5,4)	-0.256×10^{-10}	-0.284×10^{-10}	-0.266×10^{-10}	11.10%	3.960%
C(5,5)	0.789×10^{-10}	0.848×10^{-10}	0.876×10^{-10}	7.480%	11.03%
C(5,6)	-0.279×10^{-10}	-0.316×10^{-10}	-0.264×10^{-10}	13.08%	5.340%
C(6,1)	-0.704×10^{-12}	-0.602×10^{-12}	-0.182×10^{-12}	14.52%	74.10%
C(6,2)	-0.999×10^{-12}	-0.101×10^{-11}	-0.456×10^{-12}	0.920%	54.30%
C(6,3)	-0.208×10^{-11}	-0.226×10^{-11}	-0.117×10^{-11}	8.410%	43.71%
C(6,4)	-0.549×10^{-11}	-0.601×10^{-11}	-0.371×10^{-11}	9.310%	32.56%
C(6,5)	-0.279×10^{-10}	-0.316×10^{-10}	-0.264×10^{-10}	13.08%	5.340%
C(6,6)	0.668×10^{-10}	0.685×10^{-10}	0.848×10^{-10}	2.550%	26.83%

Table 3b: Inductance matrix for the six-condutor structure of Fig. 5.

	Iterative [25]	ABC	Shield	Error ABC-[25]	Error Shield-[25]
L(1,1)	0.843×10^{-6}	0.884×10^{-6}	0.475×10^{-6}	4.830%	43.60%
L(1,2)	0.439×10^{-6}	0.486×10^{-6}	0.136×10^{-6}	10.66%	68.99%
L(1,3)	0.309×10^{-6}	0.344×10^{-6}	0.542×10^{-7}	11.26%	82.44%
L(1,4)	0.235×10^{-6}	0.260×10^{-6}	0.242×10^{-7}	10.72%	89.68%
L(1,5)	0.186×10^{-6}	0.205×10^{-6}	0.113×10^{-7}	9.830%	93.92%
L(1,6)	0.153×10^{-6}	0.167×10^{-6}	0.501×10^{-8}	9.640%	96.72%
L(2,1)	0.439×10^{-6}	0.486×10^{-6}	0.136×10^{-6}	10.66%	68.99%
L(2,2)	0.837×10^{-6}	0.836×10^{-6}	0.497×10^{-6}	0.070%	40.52%
L(2,3)	0.436×10^{-6}	0.455×10^{-6}	0.147×10^{-6}	4.300%	66.18%
L(2,4)	0.307×10^{-6}	0.325×10^{-6}	0.598×10^{-7}	5.950%	80.55%
L(2,5)	0.234×10^{-6}	0.252×10^{-6}	0.265×10^{-7}	7.650%	88.69%
L(2,6)	0.186×10^{-6}	0.205×10^{-6}	0.113×10^{-7}	9.960%	93.91%
L(3,1)	0.309×10^{-6}	0.344×10^{-6}	0.542×10^{-7}	11.26%	82.44%
L(3,2)	0.436×10^{-6}	0.455×10^{-6}	0.147×10^{-6}	4.300%	66.18%
L(3,3)	0.835×10^{-6}	0.816×10^{-6}	0.503×10^{-6}	2.260%	39.74%
L(3,4)	0.436×10^{-6}	0.446×10^{-6}	0.150×10^{-6}	2.350%	65.59%
L(3,5)	0.307×10^{-6}	0.325×10^{-6}	0.598×10^{-7}	6.020%	80.55%
L(3,6)	0.235×10^{-6}	0.261×10^{-6}	0.242×10^{-7}	10.91%	89.68%
L(4,1)	0.235×10^{-6}	0.260×10^{-6}	0.242×10^{-7}	10.72%	89.68%
L(4,2)	0.307×10^{-6}	0.325×10^{-6}	0.598×10^{-7}	5.950%	80.55%
L(4,3)	0.436×10^{-6}	0.446×10^{-6}	0.150×10^{-6}	2.350%	65.59%
L(4,4)	0.835×10^{-6}	0.817×10^{-6}	0.503×10^{-6}	2.250%	39.74%
L(4,5)	0.436×10^{-6}	0.455×10^{-6}	0.147×10^{-6}	4.370%	66.17%

Table 3b (continued): Inductance matrix for the six-condutor structure of Fig. 5.

	Iterative [25]	ABC	Shield	Error ABC-[25]	Error Shield-[25]
L(4,6)	0.309×10^{-6}	0.344×10^{-6}	0.542×10^{-7}	11.46%	82.44%
L(5,1)	0.186×10^{-6}	0.205×10^{-6}	0.113×10^{-7}	9.830%	93.92%
L(5,2)	0.234×10^{-6}	0.252×10^{-6}	0.265×10^{-7}	7.650%	88.69%
L(5,3)	0.307×10^{-6}	0.325×10^{-6}	0.598×10^{-7}	6.020%	80.55%
L(5,4)	0.436×10^{-6}	0.455×10^{-6}	0.147×10^{-6}	4.370%	66.17%
L(5,5)	0.837×10^{-6}	0.836×10^{-6}	0.497×10^{-6}	0.020%	40.52%
L(5,6)	0.439×10^{-6}	0.487×10^{-6}	0.136×10^{-6}	10.82%	68.99%
L(6,1)	0.153×10^{-6}	0.167×10^{-6}	0.501×10^{-8}	9.640%	96.72%
L(6,2)	0.186×10^{-6}	0.205×10^{-6}	0.113×10^{-7}	9.960%	93.91%
L(6,3)	0.235×10^{-6}	0.261×10^{-6}	0.242×10^{-7}	10.91%	89.68%
L(6,4)	0.309×10^{-6}	0.344×10^{-6}	0.542×10^{-7}	11.46%	82.44%
L(6,5)	0.439×10^{-6}	0.487×10^{-6}	0.136×10^{-6}	10.82%	68.99%
L(6,6)	0.843×10^{-6}	0.885×10^{-6}	0.475×10^{-6}	4.940%	43.60%

	ABC with rectangular outer boundary	Reference [29]	ABC with arbitrary outer boundary
C(1,1)	0.9249×10^{-10}	0.9224×10^{-10}	0.9284×10^{-10}
C(1,2)	-0.8061×10^{-11}	-0.8504×10^{-11}	-0.8036×10^{-11}
C(2,1)	-0.8061×10^{-11}	-0.8504×10^{-11}	-0.8036×10^{-11}
C(2,2)	0.9249×10^{-10}	0.9224×10^{-10}	0.9284×10^{-10}

Table 4: Capacitance matrix for the coupled microstrips of Figures 4 and 6.

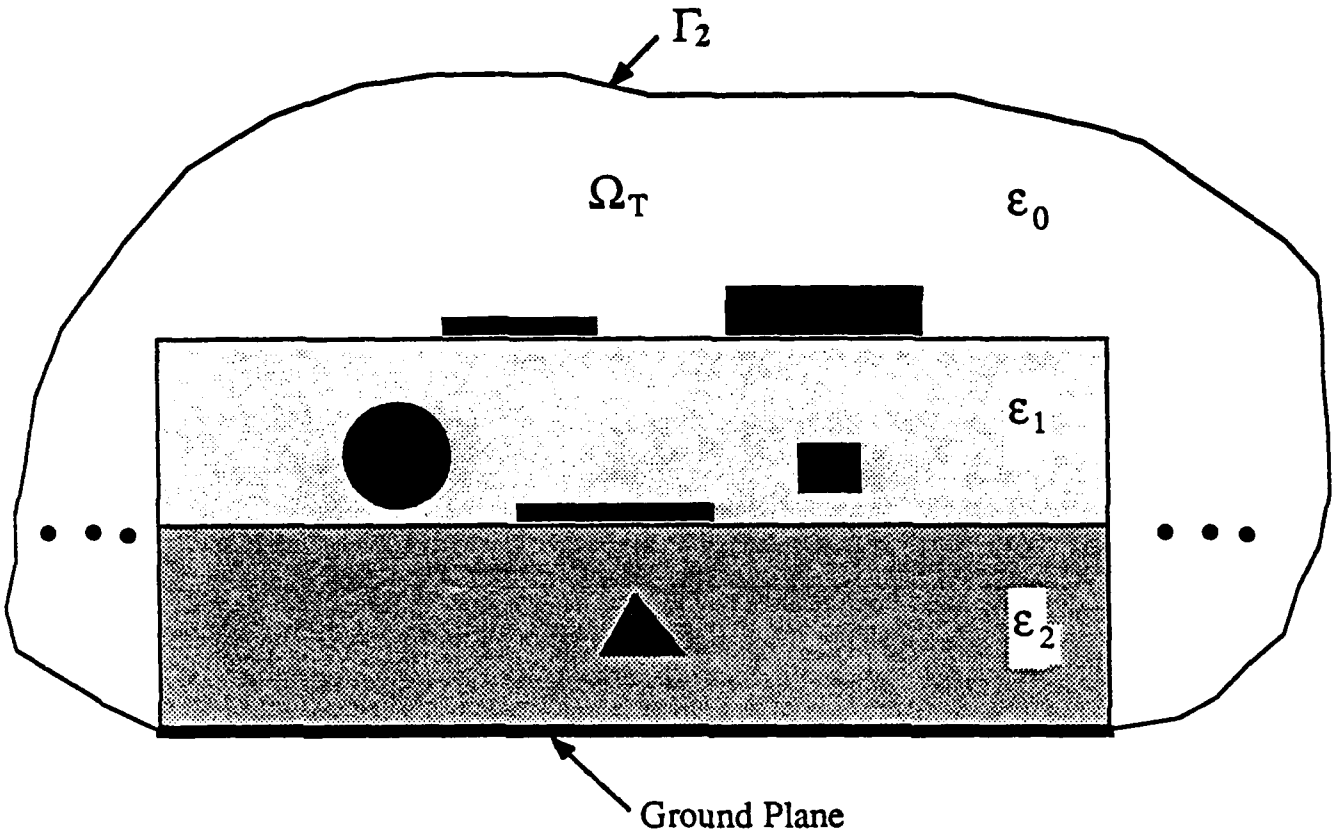

Figure 1. Multi-conductor transmission line in a multi-layered dielectric region above a ground plane.

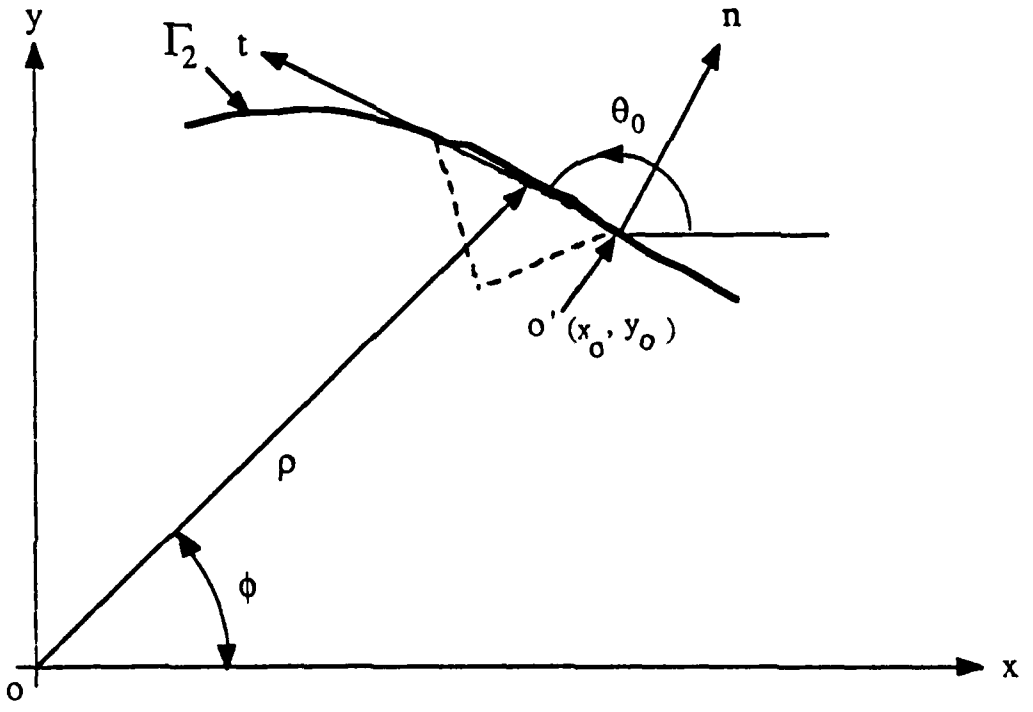

Figure 2. A triangular element residing on the arbitrary outer boundary and its local coordinates

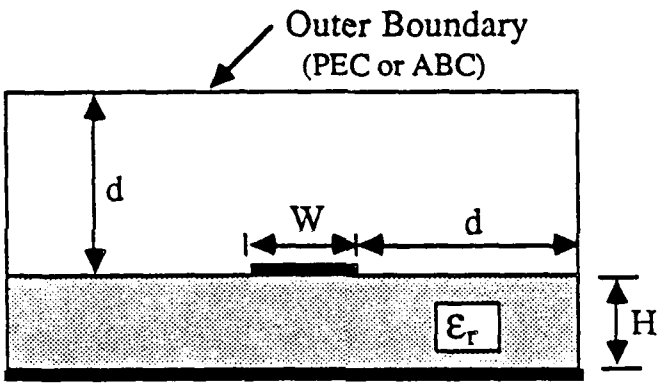

Figure 3. Microstrip line

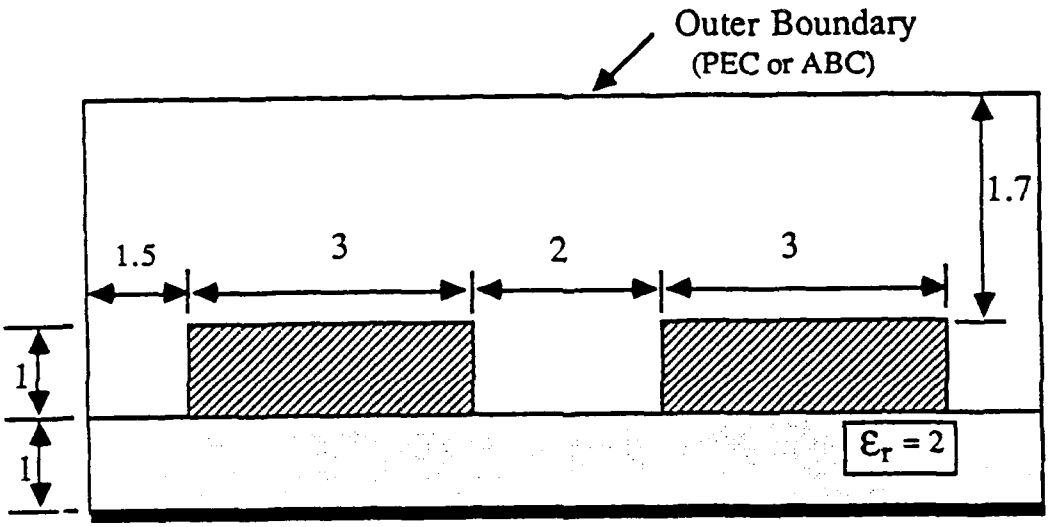

Figure 4. Coupled microstrips with rectangular outer boundary.

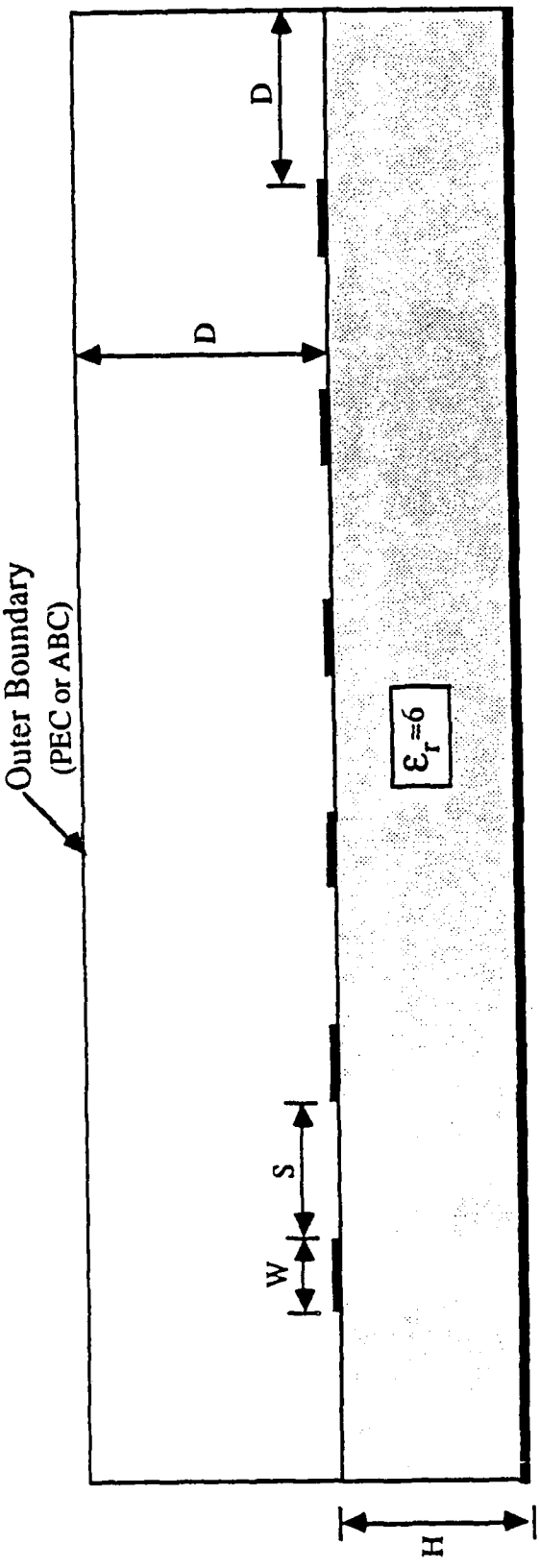

Figure 5. Six-conductor geometry.

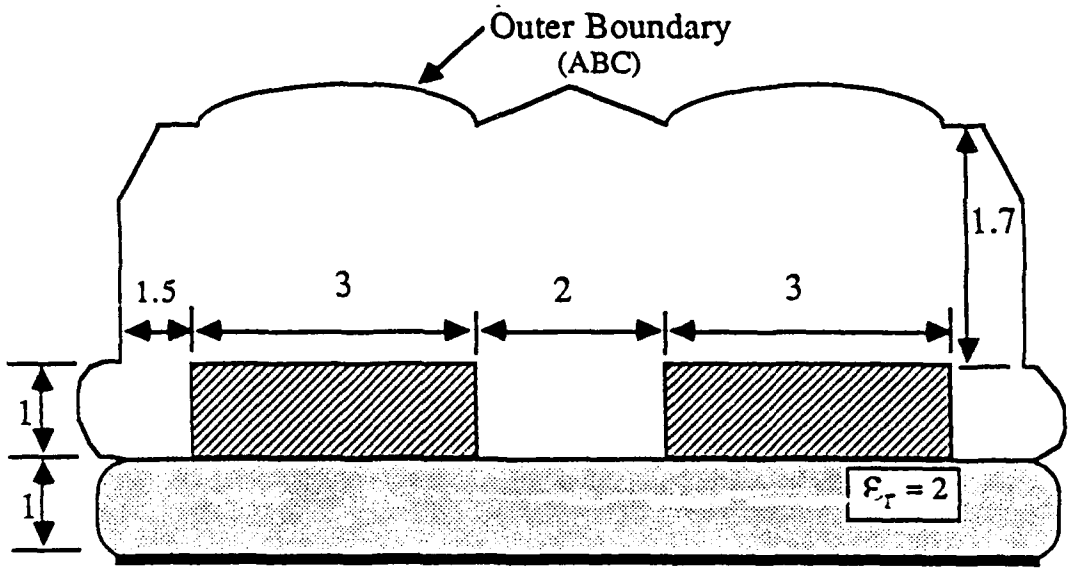

Figure 6. Coupled microstrips with arbitrary outer boundary.

APPENDIX B

TRANSIENT ANALYSIS OF LOSSY MULTICONDUCTOR TRANSMISSION LINES IN NONLINEAR CIRCUITS

by

T. S. Blazeck and R. Mittra

TABLE OF CONTENTS

CHAPTER 1

INTRODUCTION

Signal propagation along multiconductor transmission lines is of interest in the design of digital computers and communication networks. With the increase in switching speeds and denser packaging of digital devices, it has become necessary to consider transmission line effects in the interconnection of high-speed circuits. Reflections from unmatched terminations or discontinuities, or crosstalk from neighboring lines, may degrade pulses sufficiently to cause false logic levels. Skin-effect and dielectric losses cause dispersion and attenuation that can increase pulse rise and fall times, and interconnection lengths introduce signal delays that can limit overall system speed. These are among the problems confronting designers of transmission systems that propagate pulses with short rise and fall times and narrow widths.

High-speed interconnects can be metal or polysilicon lines on integrated circuit chips, printed wires on printed circuit boards, or microstrip lines between boards. In addition, it may be necessary to consider the effects of connectors, bends, junctions, crossovers, and other discontinuities in the transmission line structure. The logic circuits that terminate the lines are composed of highly nonlinear active devices such as transistors and diodes. The result can be a very complicated network consisting of lumped linear and nonlinear elements in combination with lossy coupled transmission lines. The goal of this research is to develop analytical and numerical methods for predicting the transient response of complex networks of this type. Current computer-aided design tools for nonlinear circuits have the ability to model single lossless lines or use *RC* ladders to model single resistive lines. They cannot accurately portray the multiline coupling and frequency-dependent losses that arise when high-speed signals propagate between digital circuits. Although the techniques presented herein can be applied to the transient analysis of other

multiconductor transmission lines, such as power lines under short-circuit or power-on conditions, the principal concern here is with the high-speed interconnect lines.

Early researchers of multiple parallel transmission lines used transform or operator techniques to arrive at analytical solutions for lossless or lossy lines with linear terminations [1]-[5]. Carson and Hoyt [1] formulated the multiconductor transmission line equations in the frequency domain. Their formulation was sufficiently general to allow for the frequency dependence of the resistance and inductance that results from the skin and proximity effects [6]-[7]. Shortly thereafter, Bewley [2] included the concept of multivelocity waves in a comprehensive analysis of lossless and lossy multiconductor transmission lines. Later, Pipes [3] and Rice [4] used a matrix formulation to simplify the mechanics of solving transmission line problems. And more recently, Wedepohl [5] investigated the properties of the characteristic impedance matrix, modal transformation matrices, and propagation modes associated with the steady-state solution of lossy multiconductor transmission lines.

The early sixties saw the introduction of digital-computer methods to aid in the solution of transmission line problems. Transient analysis of single and multiple lossy lines with linear loads was accomplished by using the Fourier transform to switch to the time domain [8]-[10]. However, as previously noted, the interconnections of digital circuits are themselves best modeled as multiconductor transmission lines, and digital circuits add to the problem because they are nonlinear. Initial concerns dealt with signal delays, reflections, and coupling in lossless two-line configurations [11]-[14]. Experimental and analytical investigations were carried out that increased the qualitative understanding of these effects.

Several studies of lossless n-conductor transmission lines with arbitrary nonlinear terminations were conducted in the late sixties and early seventies [15]-[19]. Amemiya [15] decoupled the propagating signals into forward and backward modal waves and then employed the generalized Thevenin or Norton equivalent circuits associated with the

method of characteristics to model the multiconductor line at its endpoints. Dommel [16] included this procedure in an electromagnetic transients program. Chang [17] used congruence transformers to decouple n-conductor transmission lines into n single lines. Recently, Tripathi and Rettig [20] implemented this method in the popular SPICE program. Ho [18] and Marx [19] analyzed the properties of the propagation modes, equivalent circuits, and characteristic resistance and conductance matrices for lossless multiconductor transmission lines. Ho also presented some numerical techniques for variable time step control during computer solution of the transmission line equations.

Lossy multiple parallel transmission lines with nonlinear terminations first received attention in the late sixties [21]-[24]. Silverberg and Wing [21] outlined a methodology for solving circuits containing lumped nonlinear elements and distributed linear elements. Their idea consisted of first characterizing the distributed part of the network in the frequency domain, then converting this characterization to the time domain, and finally solving the whole system in a time-stepping manner by matching boundary conditions at the interface. Short circuit admittance parameters (Y parameters) were used to characterize the distributed elements. In the time domain, these become impulse responses that must be convolved with the line voltages. Budner [22] used Y parameters to show results for a symmetric two-line configuration, and Snelson [23] modified the method of characteristics to get impulse responses of shorter duration than those for the Y parameters. Shorter impulse responses reduce the problem of aliasing encountered when taking the inverse transform and lessen the number of calculations that need to be computed in the time domain. Meyer and Dommel [24] made several numerical improvements to Snelson's work.

If at least one of the functions in the convolution consists entirely of exponentials, then the integration can be performed recursively. This can result in significant savings of computer time. Several authors approximated the time-domain impulse responses by finite sums of exponentials [25]-[26], while others utilized a direct frequency-domain fitting of

the transfer functions by rational polynomials [27]-[28]. With direct frequency-domain fitting, the need to perform an inverse transform is eliminated.

In the past decade there have been a number of attempts to solve the most general problem of lossy multiconductor transmission lines with nonlinear terminations [29]-[32]. Triezenberg [29] developed a state-variable transmission line model by approximating the spatial variation of the line with a finite Fourier cosine series. Gruodis and Chang [30] combined the decoupled-mode transformation, the method of characteristics, and the rational polynomial approximations together with a state variable solution. Djordjevic et al. [31] used quasi-matched Y-parameters to represent the multiconductor lines. The introduction of the quasi-matched parameters necessitated the adding of negative resistances to the terminal networks. Schutt-Aine [32] avoided this problem by using scattering parameters (S parameters) to characterize the line. Although all of these techniques are theoretically correct, results have only been shown for the simplest case of two symmetric conductors over a ground plane. In this particular case, the modal transformation matrices result in an even and odd mode no matter what the frequency; as a consequence, the most general case is avoided.

In this study time-domain models for lossy, linear, uniform multiconductor transmission lines are developed based on discretized Thevenin and Norton equivalent circuits. The analysis is quasi-TEM in that the models are derived from the (possibly frequency-dependent) per-unit-length resistance, inductance, conductance, and capacitance matrices which are assumed to be available. These models are then incorporated into a general circuit analysis program for simulating dynamic nonlinear circuits. Using the per-unit-length line parameters, the exponential propagation matrix and the characteristic impedance or admittance matrix are calculated for a range of frequencies. The exponential propagation matrix is first calculated in the decoupled-mode form (along with the modal transformation matrices), but is then recombined in the frequency domain to the full-matrix form. In the full-matrix form of the exponential propagation matrix, all impulse responses have a

physical meaning. The fast Fourier transform is utilized to convert the transfer functions to time-domain impulse responses; then, direct integration of the convolution integrals is carried out during the time-stepping procedure. Results are shown for networks of sufficient generality to fully test the method.

In Chapter 2 a general method for computer-aided analysis of dynamic nonlinear circuits is presented. The theoretical and numerical development of the time-domain models for lossy multiconductor transmission lines is described in Chapter 3. In order to verify the simulation technique, a computer program compatible with the analysis method of Chapter 2 has been written incorporating the lossy line models of Chapter 3. This program is demonstrated in Chapter 4 for several circuit configurations. Conclusions drawn from this study are discussed in Chapter 5.

CHAPTER 2

COMPUTER-AIDED ANALYSIS OF DYNAMIC NONLINEAR CIRCUITS

2.1 Introduction

Lumped-element networks are completely characterized by Kirchhoff's current law (KCL), Kirchhoff's voltage law (KVL), and the branch element equations. In general, when energy-storage and nonlinear elements are present in a circuit (i.e., a dynamic nonlinear circuit), a set of nonlinear implicit differential-algebraic equations results. Unfortunately, because there are usually no closed-form solutions to these equations, numerical methods must be used.

In this chapter common techniques are combined to form a method of computer-aided analysis of dynamic nonlinear circuits. The objective is: if circuits that contain lossy multiconductor transmission lines can be included in this method, then they can be included in similar circuit analysis programs that currently exist. The technique presented herein utilizes modified nodal analysis to formulate the circuit equations, the trapezoidal algorithm (with a fixed time step) for discrete integration, and the Newton-Raphson algorithm to iteratively solve systems of nonlinear equations.

2.2 Modified Nodal Analysis of Dynamic Nonlinear Circuits

Modified nodal analysis (MNA) [33] is an extension of nodal analysis. It is a completely general method for analyzing dynamic nonlinear networks. In nodal analysis KCL is formulated, using node voltages as variables, at each circuit node except for an arbitrarily chosen reference node. This is possible only if the current through each element is expressible as a function of the voltage across it. Voltage sources and nonlinear current-

controlled elements, for instance, do not meet this requirement. Therefore, in its most basic form, nodal analysis may be inadequate for even very simple circuits. In MNA, whenever an element is encountered that is not voltage controlled, the current through the element is introduced as a variable in the node equation, and the branch equation for that element is appended to the system of equations to be solved. The end effect is a set of equations in which the unknowns are the node voltages and some selected branch currents.

For circuits that contain nonlinear and dynamic elements, the network equations have the following functional form [34]:

$$f_1(x_1,x_2,\ldots,x_m,\dot{x}_1,\dot{x}_2,\ldots,\dot{x}_l,t) = 0 \tag{2.1a}$$

$$f_2(x_1,x_2,\ldots,x_m,\dot{x}_1,\dot{x}_2,\ldots,\dot{x}_l,t) = 0 \tag{2.1b}$$

$$\vdots \qquad\qquad \vdots$$

$$f_m(x_1,x_2,\ldots,x_m,\dot{x}_1,\dot{x}_2,\ldots,\dot{x}_l,t) = 0 \tag{2.1m}$$

where t is the temporal variable and the x_i's are the unknown circuit variables. Also, $l \leq m$ and the dot above the x_i's indicates the derivative with respect to time. Defining vectors $\mathbf{x}$ and $\dot{\mathbf{x}}$ as

$$\mathbf{x} = [x_1 \;\; x_2 \;\; \cdots \;\; x_m]^T$$

$$\dot{\mathbf{x}} = [\dot{x}_1 \;\; \dot{x}_2 \;\; \cdots \;\; \dot{x}_m]^T$$

where the T indicates transpose, Eq. (2.1) can be expressed concisely as

$$\mathbf{f}(\mathbf{x},\dot{\mathbf{x}},t) = \mathbf{0} \tag{2.2}$$

in which $\mathbf{0}$ is a vector of zeros.

Chua and Lin [34] provide detailed procedures for solving the implicit differential-algebraic (IDA) system specified by Eq. (2.2). A brief overview is given here. Suppose

that the solution $\mathbf{x}(t)$ of Eq. (2.2) had been found at time $t = t_k = kh$ (and all previous times t_j for $j = 0,1,2,...,k\text{-}1$), where h is the time step. Denoting $\mathbf{x}(t_j)$ by $\mathbf{x}_j$, the solution $\mathbf{x}_{k+1}$ at $t = t_{k+1}$ must satisfy

$$\mathbf{f}(\mathbf{x}_{k+1},\dot{\mathbf{x}}(t_{k+1}),t_{k+1}) = \mathbf{0} \tag{2.3}$$

The trapezoidal algorithm can be used to approximate the next value of $\dot{\mathbf{x}}(t_{k+1})$, the time derivative of $\mathbf{x}(t)$ evaluated at $t = t_{k+1}$, in terms of $\mathbf{x}(t_{k+1})$, $\mathbf{x}(t_k)$, and past values of $\mathbf{x}(t)$. However, this integration technique cannot be applied to Eq. (2.3) in its present form; instead, the trapezoidal rule must be applied directly to the branch equations. Introducing the vector $\mathbf{u}$ of branch currents and voltages, the branch equations can be expressed analytically as

$$\dot{\mathbf{u}} = \mathbf{g}(\mathbf{u},t) \tag{2.4}$$

where

$$\mathbf{u} = [u_1 \;\; u_2 \;\; \cdots \;\; u_{2\beta}]^T$$
$$\dot{\mathbf{u}} = [\dot{u}_1 \;\; \dot{u}_2 \;\; \cdots \;\; \dot{u}_{2\beta}]^T$$

and β is the number of branches. Applying the trapezoidal integration algorithm to the system of differential equations specified by Eq. (2.4) results in the following formula:

$$\mathbf{u}_{k+1} = \mathbf{u}_k + \frac{h}{2}[\mathbf{g}(\mathbf{u}_k,t_k) + \mathbf{g}(\mathbf{u}_{k+1},t_{k+1})] \tag{2.5}$$

With the branch equations in the form of Eq. (2.5), the modified nodal equations are recast with $\mathbf{x}_{k+1}$ as the unknown variable. This results in $\dot{\mathbf{x}}(t_{k+1})$ being replaced by $\mathbf{x}_{k+1}$ and $\mathbf{x}_k$, and functions that depend on them. Since the variable $\mathbf{x}_k$ is known at time t_{k+1}, Eq. (2.3) may then be rewritten as

$$\mathbf{f}(\mathbf{x}_{k+1},t_{k+1}) = \mathbf{0} \tag{2.6}$$

Observe that Eq. (2.6) is a system of nonlinear algebraic equations in terms of the unknown variable $\mathbf{x}_{k+1}$. The most common technique for solving systems of nonlinear equations is the Newton-Raphson (N-R) algorithm. Using the N-R algorithm, $\mathbf{x}_{k+1}$ is iterated to a solution via the following recursive relation:

$$\mathbf{J}(\mathbf{x}_{k+1}^{(j)})\mathbf{x}_{k+1}^{(j+1)} = \mathbf{J}(\mathbf{x}_{k+1}^{(j)})\mathbf{x}_{k+1}^{(j)} - \mathbf{f}(\mathbf{x}_{k+1}^{(j)}, t_{k+1}) \tag{2.7}$$

where the superscript indicates the current iteration and

$$\mathbf{J}(\mathbf{x}_{k+1}^{(j)}) = \frac{\partial \mathbf{f}(\mathbf{x},t)}{\partial \mathbf{x}} \Big|_{\mathbf{x} = \mathbf{x}_{k+1}^{(j)}}$$

is the Jacobian matrix of $\mathbf{f}(\mathbf{x},t)$ evaluated at $\mathbf{x} = \mathbf{x}_{k+1}^{(j)}$. Equation (2.7) is a linear algebraic system of equations of the form $\mathbf{Ax} = \mathbf{b}$, where $\mathbf{A}$ is a constant matrix, $\mathbf{b}$ is a constant vector, and $\mathbf{x}$ is a vector of unknowns. There are several efficient numerical algorithms for its solution.

Summarizing, the method just outlined requires three steps. First, the circuit equations are formulated using the MNA procedure. This results in a nonlinear implicit differential-algebraic system of equations. Next, the IDA equations are discretized by applying the trapezoidal rule to the branch equations. This leads to a system of nonlinear algebraic equations that must be solved at each time step. And last, the nonlinear equations are linearized using the N-R technique. This leaves a set of linear algebraic equations to be solved at each iteration.

2.3 Companion Models and Element Stamps

In computer implementation of MNA, KCL and the branch equations are not assembled one at a time as they are in hand calculations. Instead each element of the circuit is modeled by first discretizing (if necessary) and then linearizing (again if necessary) the branch equation(s) for that element. The resulting equivalent circuit, which depends on the

given integration and nonlinear iteration schemes, is commonly referred to as the element's companion model. The discretizing of the elements generates a nonlinear static (resistive) circuit, instead of the nonlinear dynamic circuit originally given. The linearization changes the nonlinear resistive circuit into a linear resistive circuit. The network equations are then formulated using the rules previously outlined for MNA. Since the network now consists solely of sources and resistors, the circuit equations are of the form $\mathbf{Ax} = \mathbf{b}$. The overall solution of the network amounts to solving a sequence of nonlinear resistive circuits by iterating a sequence of linear resistive circuits. The derivation of companion models for a number of common circuit elements will now be considered.

2.3.1 Linear reactive elements

A linear capacitor is illustrated in Fig. 2.1(a). The branch equations for the capacitor are

$$q = Cv \qquad \frac{dq}{dt} = i$$

where C is the capacitance, v is the voltage across the capacitor, q is the charge on one of its plates, and i is the current through the capacitor from node y to node z. Using the trapezoidal method to discretize $\dot{q} = i$ at time t_{k+1} results in

$$q_{k+1} = q_k + \frac{h}{2}(i_k + i_{k+1})$$

Substituting Cv for q and solving for i_{k+1} yield

$$i_{k+1} = \frac{2}{h}Cv_{k+1} - \left(\frac{2}{h}Cv_k + i_k\right) \tag{2.8}$$

As shown in Fig. 2.1(b), Eq. (2.8) can be realized as a resistor with conductance $2C/h$ in parallel with a current source of value $2Cv_k/h + i_k$. The conductance value is fixed because the time step h is constant, but due to the memory inherent in this energy-storage element,

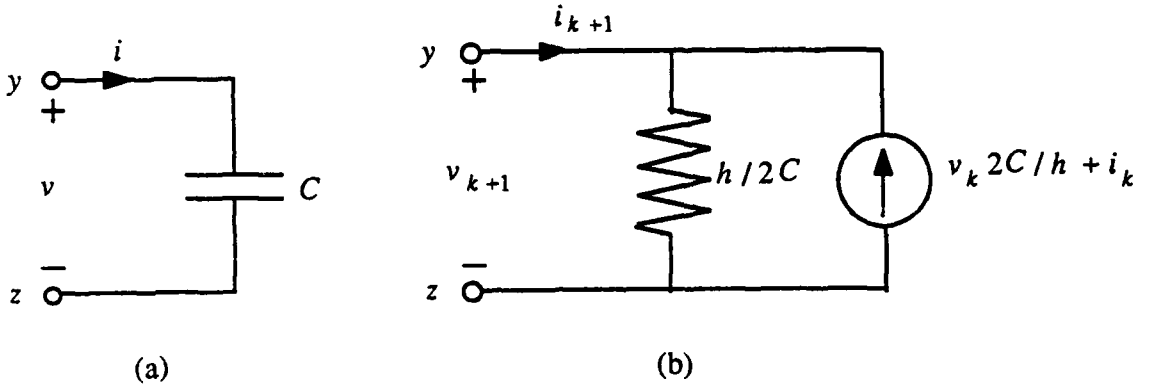

$$
\begin{array}{c} \\ y \\ z \end{array}
\begin{array}{c} \begin{array}{ccccc} & y & & z & \end{array} \\ \begin{bmatrix} \vdots & & \vdots & & \\ \cdots & \frac{2C}{h} & \cdots & -\frac{2C}{h} & \cdots \\ \vdots & & \vdots & & \\ -\frac{2C}{h} & \cdots & \frac{2C}{h} & \cdots & \\ & & \vdots & & \end{bmatrix} \end{array}
\begin{bmatrix} \vdots \\ v_{y\,k+1} \\ \vdots \\ v_{z\,k+1} \\ \vdots \end{bmatrix}
=
\begin{bmatrix} \vdots \\ \frac{2C}{h}v_k + i_k \\ \vdots \\ -\left(\frac{2C}{h}v_k + i_k\right) \\ \vdots \end{bmatrix}
$$

A **x** **b**

(c)

$$
\begin{array}{c} \\ y \\ z \\ \text{branch} \\ \text{equation} \end{array}
\begin{array}{c} \begin{array}{ccccc} y & & z & & \text{“}i\text{”} \end{array} \\ \begin{bmatrix} \vdots & & & & \\ \cdots & & & +1 & \\ & & & \vdots & \\ & & & -1 & \\ & & & \vdots & \\ & \frac{2C}{h} & \cdots & -1 & \cdots \\ & & & \vdots & \end{bmatrix} \end{array}
\begin{bmatrix} \vdots \\ v_{y\,k+1} \\ \vdots \\ v_{z\,k+1} \\ \vdots \\ i_{k+1} \\ \vdots \end{bmatrix}
=
\begin{bmatrix} \vdots \\ \\ \vdots \\ \\ \vdots \\ \frac{2C}{h}v_k + i_k \\ \vdots \end{bmatrix}
$$

A **x** **b**

(d)

Figure 2.1 Linear capacitor: (a) symbol and definitions, (b) companion model at time t_{k+1}, (c) element stamp, (d) element stamp with branch current as a variable.

the current source depends on the previous capacitor voltage and current. This means that the current source will have to be updated at each time step.

Following the rules of MNA, one can visualize writing KCL at nodes y and z to arrive at the nonzero entries, shown in Fig. 2.1(c), of the coefficient matrix **A** and source vector **b**. Since the current through the capacitor is expressible as a function of the voltage across it, it was not necessary to introduce the current as a variable when implementing KCL. However, it is sometimes convenient to do so, particularly when the current is desired as an output variable, or when it is needed for a current-controlled element. In such cases KCL is written at each node with the current as the variable, and then the discretized branch equation, Eq. (2.8), is appended to get the nonzero entries of **A** and **b** indicated in Fig. 2.1(d).

An analogous procedure is used to derive the companion model for a linear inductor and its corresponding element stamp. The necessary equations for the inductor depicted in Fig. 2.2(a) are

$$\phi = Li \qquad \frac{d\phi}{dt} = v$$

where L is the inductance, v is the voltage across the inductor, ϕ is the flux linking the inductor coils, and i is the current through the inductor from node y to node z. Following steps identical to those just used for the capacitor, the discretized branch equation for the inductor at time t_{k+1} is easily found to be

$$v_{k+1} = \frac{2}{h}Li_{k+1} - \left(\frac{2}{h}Li_k + v_k\right) \tag{2.9}$$

This equation leads to the companion model illustrated in Fig. 2.2(b). Since a voltage source is contained in the model, the stamp for this element is derived by writing KCL at each terminal of the element using the current through the inductor as the variable, and then Eq. (2.9) is added to get the **A** and **b** entries shown in Fig. 2.2(c).

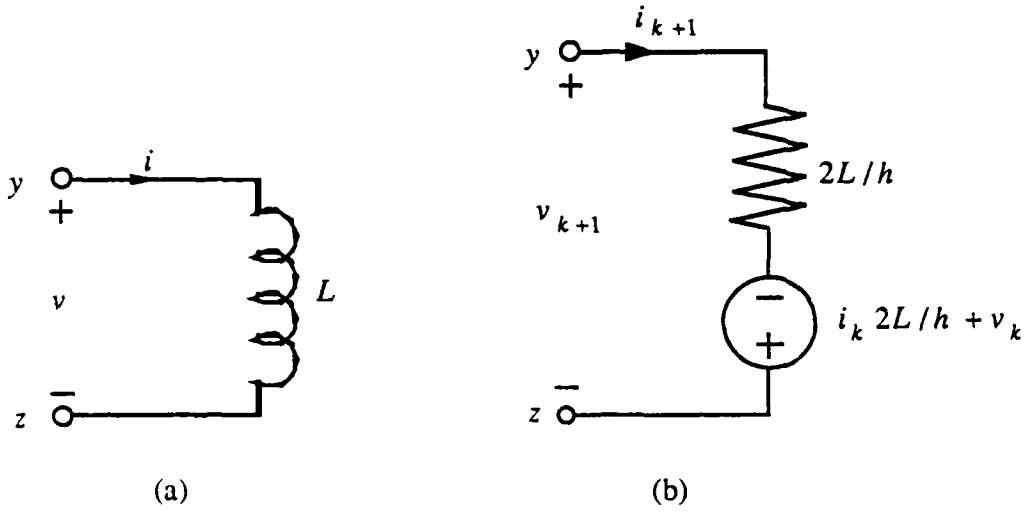

$$
\begin{array}{c}
\\
y \\
z \\
\text{branch} \\ \text{equation}
\end{array}
\begin{array}{c}
\begin{array}{cccccc} y & & z & & \text{“}i\text{”} & \end{array} \\
\begin{bmatrix}
\vdots & & & & & \\
\cdots & & & & +1 & \\
 & & & & \vdots & \\
 & & & & -1 & \\
 & & & & \vdots & \\
 & +1 & \cdots & -1 & \cdots & -\frac{2L}{h} \quad \cdots \\
 & & & & \vdots &
\end{bmatrix}
\end{array}
\begin{bmatrix} \vdots \\ v_{y\,k+1} \\ \vdots \\ v_{z\,k+1} \\ \vdots \\ i_{k+1} \\ \vdots \end{bmatrix}
=
\begin{bmatrix} \vdots \\ \\ \vdots \\ \\ \vdots \\ -\left(\frac{2L}{h} i_k + v_k\right) \\ \vdots \end{bmatrix}
$$

$$\mathbf{A} \qquad \mathbf{x} \qquad \mathbf{b}$$

(c)

Figure 2.2 Linear inductor: (a) symbol and definitions, (b) companion model at time t_{k+1}, (c) element stamp.

2.3.2 Controlled sources and coupled elements

Controlled sources are easily included in computer-aided circuit analysis programs that utilize the modified nodal approach. The current-controlled current source (CCCS) is employed as an example here.

The symbol for the CCCS is illustrated in Fig. 2.3(a). The branch equation for this element is $i = \alpha\, i_a$, where i_a is the controlling current through some element a, and α is the gain of the source. The CCCS is a memoryless element; consequently, its companion model at any time step is just the source itself. This model is shown in Fig. 2.3(b) and the corresponding element stamps are depicted in Figs. 2.3(c) and 2.3(d). When constructing these stamps, the controlling current i_a was assumed to be available as a circuit variable. The stamps of other types of controlled sources are derived in much the same manner.

Coupled elements can generally be characterized by some combination of linear resistors and controlled sources. Take for instance the coupled inductors illustrated in Fig. 2.4(a). The equations for this element can be written compactly in matrix form as

$$\boldsymbol{\varphi} = \mathbf{L}\mathbf{i} \qquad \frac{d\boldsymbol{\varphi}}{dt} = \mathbf{v}$$

where $\mathbf{v}$ is a vector of branch voltages, $\boldsymbol{\varphi}$ a vector of related fluxes, $\mathbf{i}$ a vector of branch currents, and $\mathbf{L}$ the inductance matrix. Discretizing $\dot{\boldsymbol{\varphi}} = \mathbf{v}$ at time t_{k+1}, substituting $\mathbf{L}\mathbf{i}$ for $\boldsymbol{\varphi}$, and solving for $\mathbf{v}_{k+1}$ yield

$$\mathbf{v}_{k+1} = \frac{2}{h}\mathbf{L}\mathbf{i}_{k+1} - \left(\frac{2}{h}\mathbf{L}\mathbf{i}_k + \mathbf{v}_k\right) \tag{2.10}$$

Expanding Eq. (2.10), the following is obtained:

$$v_{1\,k+1} = \frac{2}{h}L_{11}i_{1\,k+1} + \frac{2}{h}Mi_{2\,k+1} - \left(\frac{2}{h}L_{11}i_{1\,k} + \frac{2}{h}Mi_{2\,k} + v_{1\,k}\right) \tag{2.11a}$$

$$v_{2\,k+1} = \frac{2}{h}Mi_{1\,k+1} + \frac{2}{h}L_{22}i_{2\,k+1} - \left(\frac{2}{h}Mi_{1\,k} + \frac{2}{h}L_{22}i_{2\,k} + v_{2\,k}\right) \tag{2.11b}$$

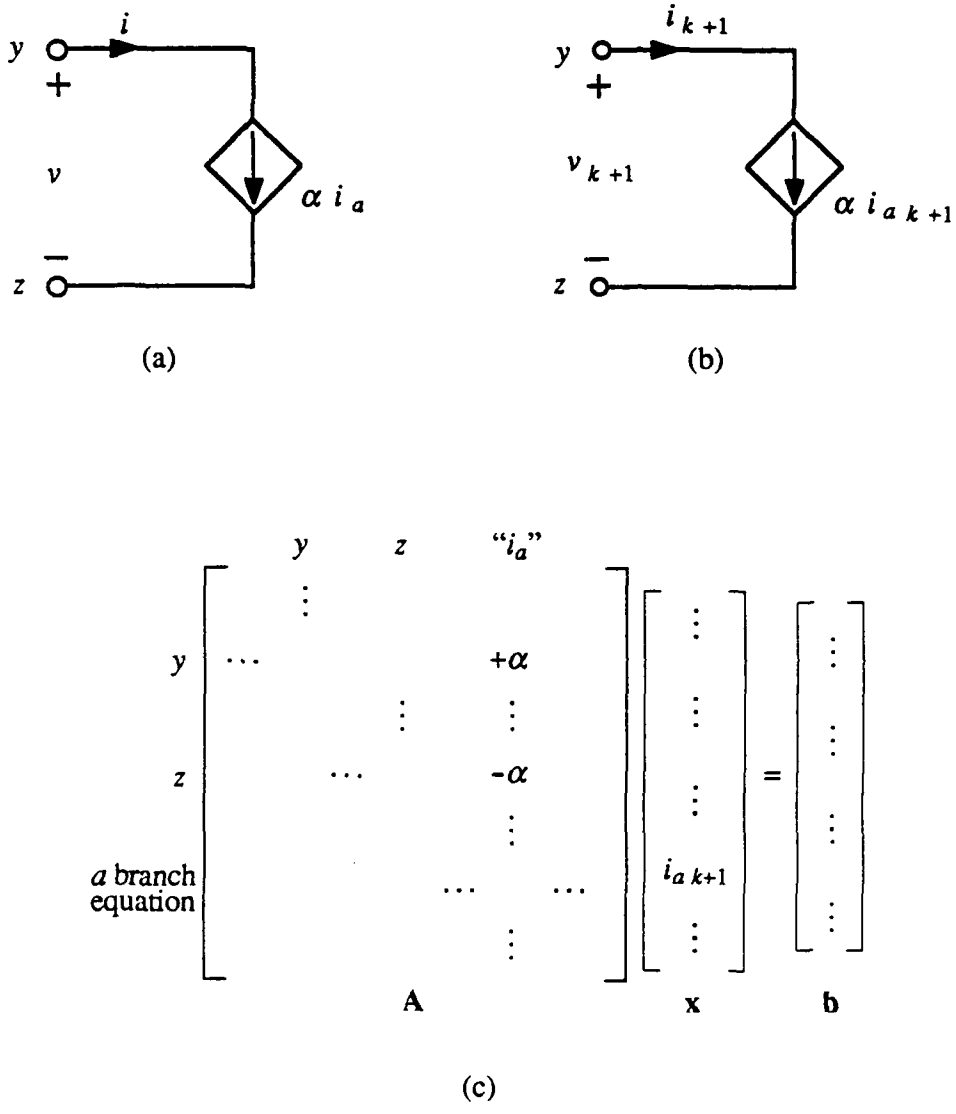

Figure 2.3 Linear current-controlled current source: (a) symbol and definitions, (b) companion model at time t_{k+1}, (c) element stamp.

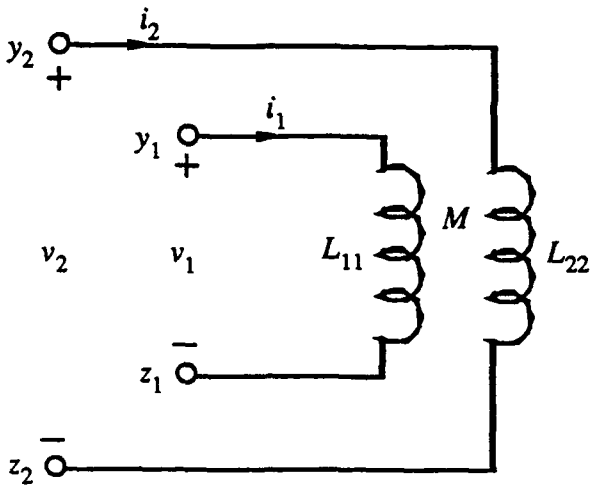

(a)

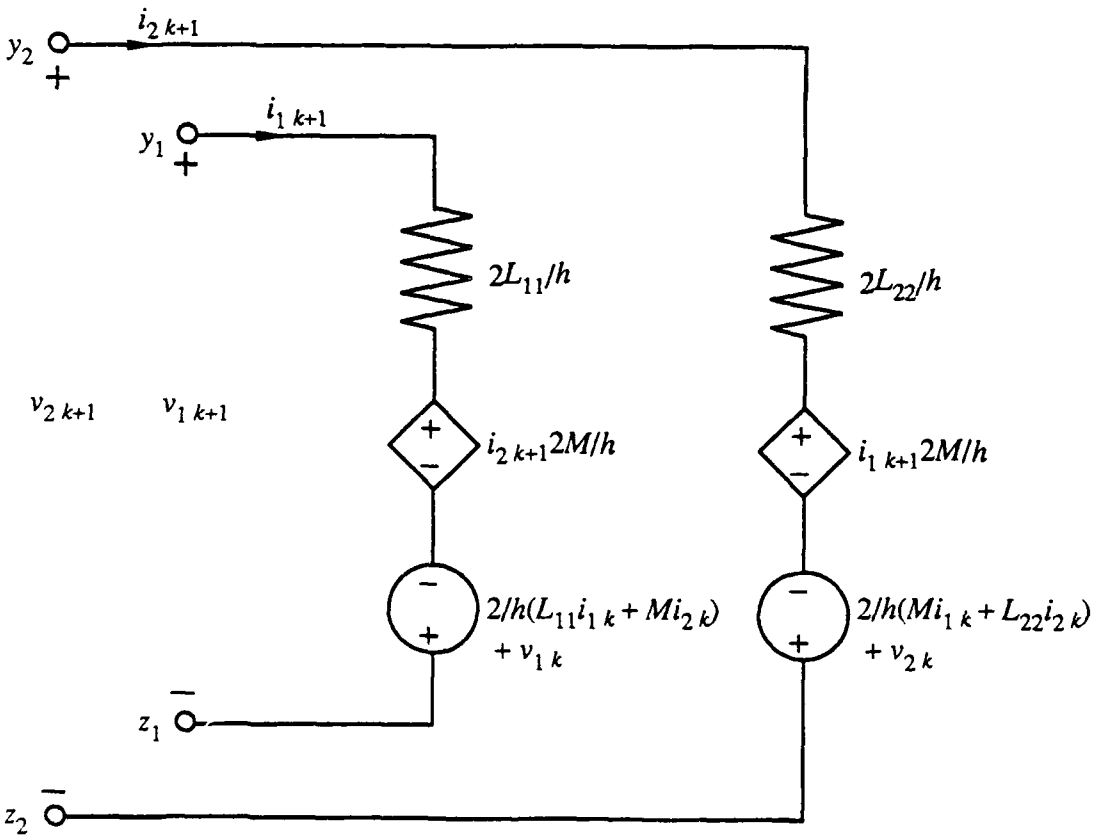

(b)

Figure 2.4 Linear coupled inductors: (a) symbol and definitions, (b) companion model at time t_{k+1}.

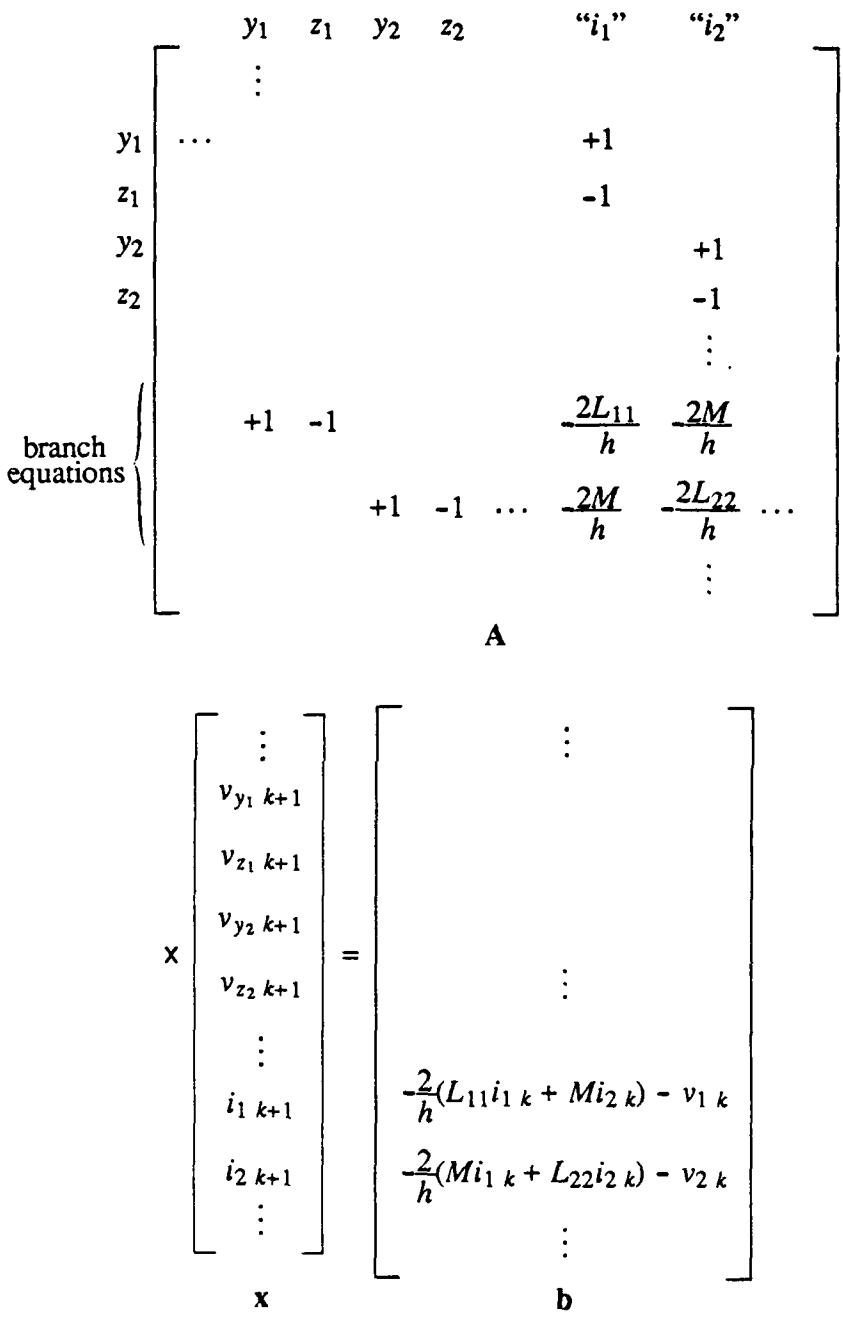

(c)

Figure 2.4 (cont.) Linear coupled inductors: (c) element stamp.

From Eq. (2.11) one can see that the diagonal elements of **L** multiplied by $2/h$ are resistance values, while the off-diagonal elements multiplied by $2/h$ are transresistance values of gain for current-controlled voltage sources. The last terms on the right-hand sides of Eqs. (2.11a) and (2.11b) can be represented by independent voltage sources.

The companion model for the coupled inductors is shown in Fig. 2.4(b). The stamp is constructed in a manner similar to that for a single inductor and is presented in Fig. 2.4(c).

2.3.3 The nonlinear capacitor

Nonlinear resistors and capacitors are the nonlinear elements most needed when modeling digital devices. Since the nonlinear capacitor actually contains a nonlinear resistor in its companion model, the capacitor will be used as the demonstration element here.

Figure 2.5(a) shows a nonlinear capacitor. Most nonlinear capacitors encountered are voltage controlled and can be represented analytically by the following equations:

$$q = q(v) \qquad \frac{dq}{dt} = i$$

where q, v, and i are charge, voltage, and current, respectively, and $q(v)$ indicates that the charge is some nonlinear function of the voltage. Discretizing the time derivative of the charge using the trapezoidal rule and solving for i_{k+1} result in

$$i_{k+1} = \frac{2}{h}q(v_{k+1}) - \left(\frac{2}{h}q(v_k) + i_k\right) \tag{2.12}$$

This equation can be represented by the equivalent circuit shown in Fig. 2.5(b). It is similar to the model for the linear capacitor of Fig. 2.1(b), except that now the resistor is nonlinear.

From Eq. (2.12) and Fig. 2.5(b), one can see that the current through the nonlinear resistor obeys the equation $i_R = 2q(v)/h$. A sample v-i_R curve for this function has been

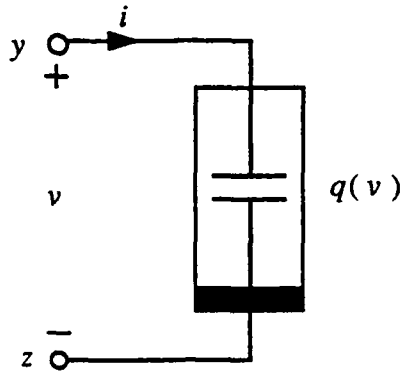

(a)

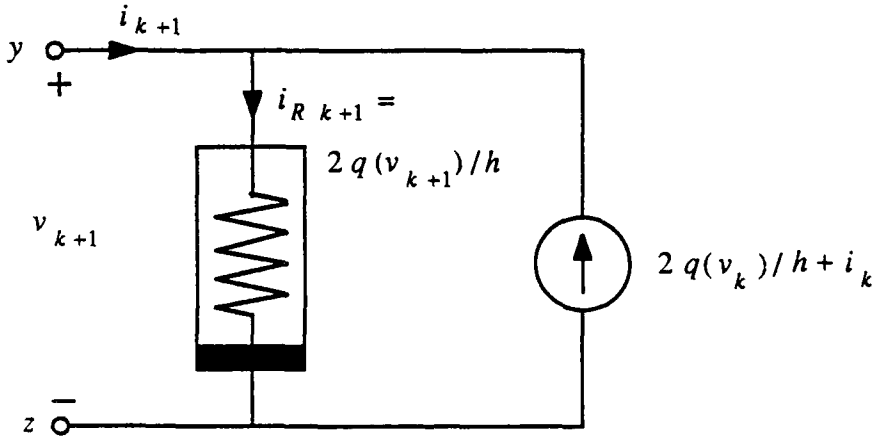

(b)

Figure 2.5 Nonlinear capacitor: (a) symbol and definitions, (b) companion model at time t_{k+1}, which consists of a nonlinear resistor in parallel with a current source.

drawn in Fig. 2.6(a). Suppose that the solution for the network had been found at time t_k. This result can be used to initiate an iteration scheme to find the solution at time t_{k+1}. After the (j)th iteration, the solution for the nonlinear resistor will be a particular point on its v-i_R curve. Designating this point as $P^{(j)}$ on the sample curve of Fig. 2.6(a), the operation of the resistor can be approximated by the line drawn tangent to the curve at that point. The equation for this line is

$$i_{R\,k+1}^{(j)} = g_{k+1}^{(j)} v_{k+1}^{(j)} + I_{S\,k+1}^{(j)} \tag{2.13}$$

where

$$g_{k+1}^{(j)} = \frac{2}{h} \frac{\partial q(v)}{\partial v} \Big|_{v = v_{k+1}^{(j)}}$$

is the slope at point $P^{(j)}$ and $I_{S\,k+1}^{(j)}$ is the i_R intercept. Solving Eq. (2.13) for this intercept yields

$$I_{S\,k+1}^{(j)} = i_{R\,k+1}^{(j)} - g_{k+1}^{(j)} v_{k+1}^{(j)}$$

Now substituting $I_{S\,k+1}^{(j)}$ back into Eq. (2.13), and updating the iteration count on the unknown variables $i_{R\,k+1}$ and v_{k+1}, the following recursive formula is obtained:

$$i_{R\,k+1}^{(j+1)} = g_{k+1}^{(j)} v_{k+1}^{(j+1)} + I_{S\,k+1}^{(j)} \tag{2.14}$$

Equation (2.14) can be modeled by the parallel combination of resistor and current source shown in Fig. 2.6(b). Substituting Eq. (2.14) into Eq. (2.12) yields (since $i_R = 2q(v)/h$)

$$i_{k+1}^{(j+1)} = g_{k+1}^{(j)} v_{k+1}^{(j+1)} + I_{S\,k+1}^{(j)} - \left(\frac{2}{h} q(v_k) + i_k \right) \tag{2.15}$$

Equation (2.15) leads to the overall companion model of Fig. 2.7(a) for the nonlinear capacitor. This model characterizes the capacitor for iteration $(j+1)$ at time t_{k+1}. The

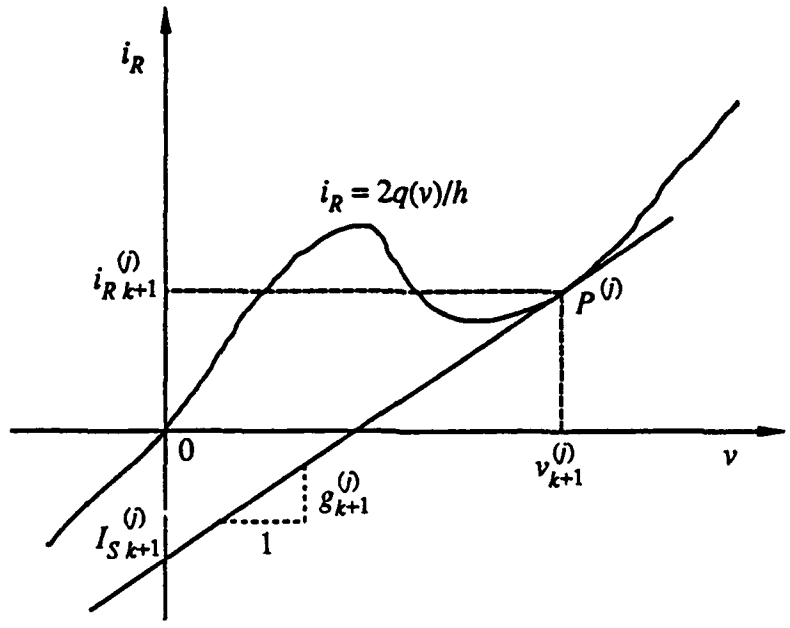

(a)

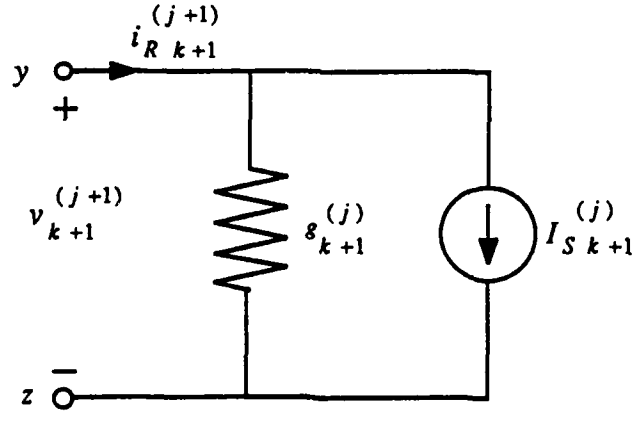

(b)

Figure 2.6 Nonlinear resistor of Eq. (2.12) and Fig. 2.5(b): (a) sample v-i_R curve, (b) companion model for iteration $(j+1)$ at time t_{k+1}.

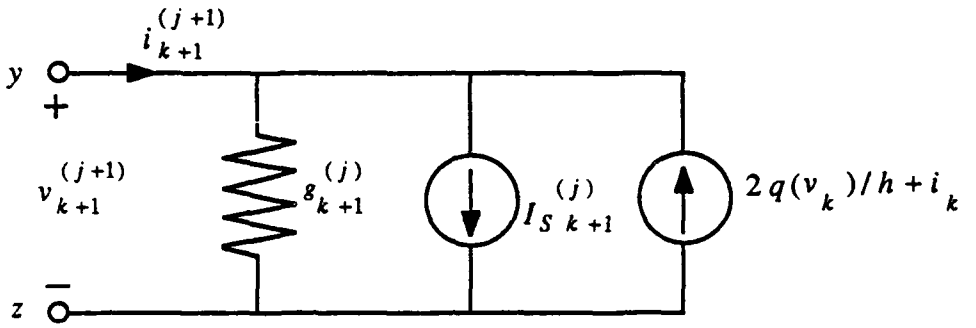

(a)

$$
\begin{array}{c} \\ y \\ \\ z \\ \\ \end{array}
\begin{array}{c} \begin{array}{cccc} \quad & y & \quad & z \end{array} \\
\begin{bmatrix} \vdots & & \vdots & \\ \cdots & g_{k+1}^{(j)} & \cdots & -g_{k+1}^{(j)} \\ \vdots & & \vdots & \\ \cdots & -g_{k+1}^{(j)} & \cdots & g_{k+1}^{(j)} \\ & & & \vdots \end{bmatrix} \\ \mathbf{A} \end{array}
\begin{array}{c} \\ \begin{bmatrix} \vdots \\ v_{y\,k+1} \\ \vdots \\ v_{z\,k+1} \\ \vdots \end{bmatrix} \\ \mathbf{x} \end{array}
=
\begin{array}{c} \\ \begin{bmatrix} \vdots \\ 2q(v_k)/h + i_k - I_{S\,k+1}^{(j)} \\ \vdots \\ I_{S\,k+1}^{(j)} - 2q(v_k)/h + i_k \\ \vdots \end{bmatrix} \\ \mathbf{b} \end{array}
$$

(b)

$$
\begin{array}{c} \\ y \\ \\ z \\ \\ \text{branch} \\ \text{equation} \end{array}
\begin{array}{c} \begin{array}{cccc} \quad & y & \quad & z \end{array} \\
\begin{bmatrix} \vdots & & & \\ \cdots & & & +1 \\ & & & \vdots \\ & & & -1 \\ & & & \vdots \\ & g_{k+1}^{(j)} & \cdots & -g_{k+1}^{(j)} \end{bmatrix} \\ \mathbf{A} \end{array}
\begin{array}{c} \begin{array}{c} \quad \\ \quad \\ \quad \\ \quad \\ \quad \\ \quad \\ \quad \end{array} \\
\begin{bmatrix} \vdots \\ v_{y\,k+1} \\ \vdots \\ v_{z\,k+1} \\ \vdots \\ i_{k+1} \\ \vdots \end{bmatrix} \\ \mathbf{x} \end{array}
=
\begin{array}{c} \begin{array}{c} \quad \\ \quad \\ \quad \\ \quad \\ \quad \\ \quad \\ \quad \end{array} \\
\begin{bmatrix} \vdots \\ \vdots \\ \vdots \\ 2q(v_k)/h + i_k - I_{S\,k+1}^{(j)} \\ \vdots \end{bmatrix} \\ \mathbf{b} \end{array}
$$

(c)

Figure 2.7 Nonlinear capacitor: (a) companion model for iteration (j+1) at time t_{k+1}, (b) element stamp, (c) element stamp with branch current as a variable.

linearization method presented here can be shown to be identical to the Newton-Raphson method discussed in Section 2.2 [34].

Comparing the companion model for the nonlinear capacitor here with that of the linear capacitor of Fig. 2.1(b), it can be seen that they have the same form. This being the case, the element stamps for the nonlinear capacitor are easily constructed and are illustrated in Figs. 2.7(b) and 2.7(c). When using the stamp of Fig. 2.7(b), convergence of the voltage within the prescribed limits does not always mean that sufficient convergence of the current has occurred. For this reason, the stamp of Fig. 2.7(c) is generally preferred for nonlinear elements since the current is available as a variable and may be subjected to the same convergence requirements as the voltage.

2.4 Conclusions

In this chapter, a commonly used and completely general method of computer-aided circuit analysis was presented. Implementation of a particular element in a circuit analysis program consists of developing a companion model for that element and substituting the element's stamp into the coefficient matrix **A** and source vector **b**. The overall solution of a network amounts to solving a sequence of nonlinear resistive circuits by iterating a sequence of linear resistive circuits. In the following chapter, two different companion models and their corresponding element stamps are developed for a lossy multiconductor transmission line in order that it may be included in a circuit analysis program of the type discussed in this chapter.

CHAPTER 3

LOSSY MULTICONDUCTOR TRANSMISSION LINES

3.1 Introduction

The analysis of nonlinear circuits, in the general case, can be performed only in the time domain. On the other hand, the analysis of lossy transmission lines, particularly those with frequency-dependent parameters, is handled most conveniently in the frequency domain. Therefore, in order to devise a method of analysis for lossy multiconductor transmission lines in nonlinear circuits, it is necessary to combine solutions from the two domains. Assuming that the transmission lines are linear, the inverse Fourier transform can be used to convert frequency-domain characterizations of the lines to the time domain. Boundary conditions at the interface of the lossy distributed lines and lumped nonlinear networks can then be matched at discrete time steps. [31]

In this chapter, the lossy multiconductor transmission line equations are first solved in the frequency domain; then, the inverse Fourier transform is utilized to switch to the time domain where two different companion models are developed to represent the multiconductor line at its endpoints. One of the models consists of a discretized Thevenin equivalent circuit for each end of the line, while the other model consists of discretized Norton equivalent circuits. Depending on the properties of the line, it may be advantageous to use one or the other. In addition, numerical issues are discussed for calculating and implementing the models in a general circuit analysis program.

3.2 Frequency-Domain Solutions

A lossy (n+1)-conductor transmission line of length d is shown in Fig. 3.1. The telegrapher's equations for this transmission line can be expressed in matrix form as [35]

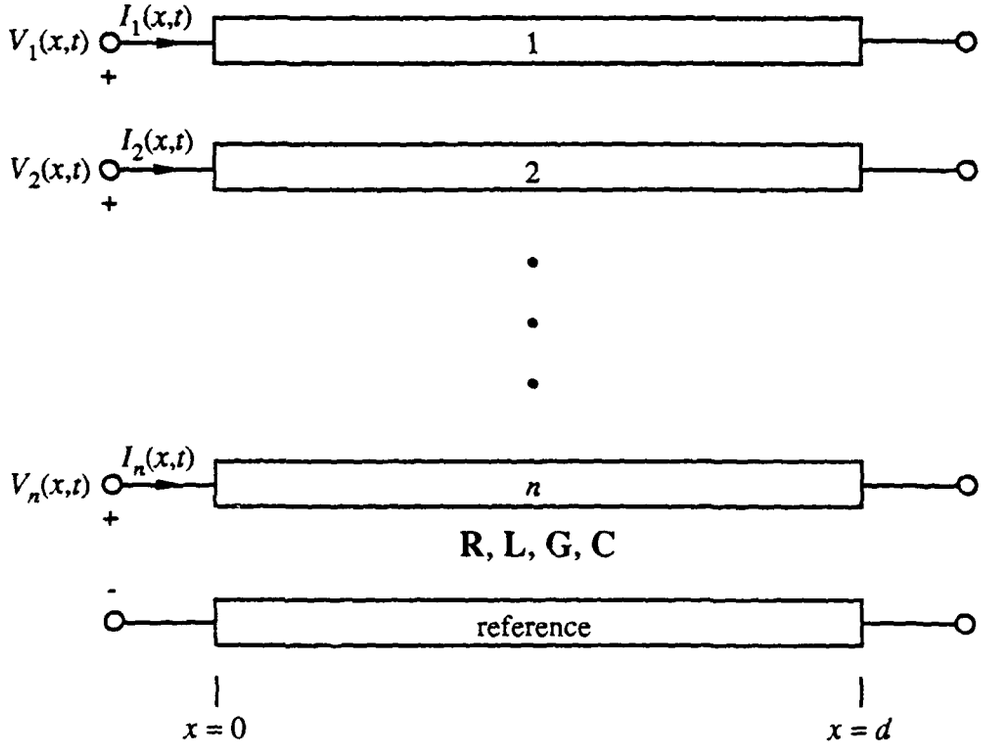

Figure 3.1 Lossy (n+1)-conductor transmission line of length d.

$$-\frac{\partial \mathbf{V}(x,t)}{\partial x} = \mathbf{R}\mathbf{I}(x,t) + \mathbf{L}\frac{\partial \mathbf{I}(x,t)}{\partial t} \tag{3.1a}$$

$$-\frac{\partial \mathbf{I}(x,t)}{\partial x} = \mathbf{G}\mathbf{V}(x,t) + \mathbf{C}\frac{\partial \mathbf{V}(x,t)}{\partial t} \tag{3.1b}$$

where x and t are the spacial and temporal variables, respectively; $\mathbf{V}(x,t)$ is an $n \times 1$ vector of line voltages; $\mathbf{I}(x,t)$ is an $n \times 1$ vector of line currents; and $\mathbf{R}$, $\mathbf{L}$, $\mathbf{G}$, and $\mathbf{C}$ are the $n \times n$ per-unit-length resistance, inductance, conductance, and capacitance matrices, respectively. The jth element of $\mathbf{V}(x,t)$, $V_j(x,t)$, and the jth element of $\mathbf{I}(x,t)$, $I_j(x,t)$, are the voltage and current, respectively, on line j. In the formulation above, the line-parameter matrices are constant; this is of limited usefulness since for even relatively slowly varying signals the relationship between voltage and current on most transmission systems is actually more complicated [35]. Once Eq. (3.1) has been transformed into the frequency domain, this restriction on the time rate of change of voltages and currents can be overcome in many cases by allowing the line-parameter matrices $\mathbf{R}$, $\mathbf{L}$, $\mathbf{G}$, and $\mathbf{C}$ to be frequency dependent. Proceeding in this manner, the Fourier transform of Eq. (3.1) with respect to time t yields

$$-\frac{\partial \mathbf{V}(x,\omega)}{\partial x} = (\mathbf{R} + j\omega\mathbf{L})\mathbf{I}(x,\omega)$$

$$-\frac{\partial \mathbf{I}(x,\omega)}{\partial x} = (\mathbf{G} + j\omega\mathbf{C})\mathbf{V}(x,\omega)$$

where ω is the radian frequency; then, explicitly showing the frequency dependence of the line-parameter matrices leads to

$$-\frac{\partial \mathbf{V}(x,\omega)}{\partial x} = [\mathbf{R}(\omega) + j\omega\mathbf{L}(\omega)]\mathbf{I}(x,\omega) = \mathbf{Z}(\omega)\mathbf{I}(x,\omega) \tag{3.2a}$$

$$-\frac{\partial \mathbf{I}(x,\omega)}{\partial x} = [\mathbf{G}(\omega) + j\omega\mathbf{C}(\omega)]\mathbf{V}(x,\omega) = \mathbf{Y}(\omega)\mathbf{V}(x,\omega) \tag{3.2b}$$

where the impedance per unit length, $\mathbf{Z}(\omega) = \mathbf{R}(\omega) + j\omega\mathbf{L}(\omega)$, and the admittance per unit length, $\mathbf{Y}(\omega) = \mathbf{G}(\omega) + j\omega\mathbf{C}(\omega)$, have been introduced. As a consequence of reciprocity,

$\mathbf{R}(\omega)$, $\mathbf{L}(\omega)$, $\mathbf{G}(\omega)$, and $\mathbf{C}(\omega)$ are symmetric; therefore, so are $\mathbf{Z}(\omega)$ and $\mathbf{Y}(\omega)$. A physical interpretation of $\mathbf{R}(\omega)$, $\mathbf{L}(\omega)$, $\mathbf{G}(\omega)$, and $\mathbf{C}(\omega)$ is given later in Sec. 3.2.1. The calculation of these matrices is not a part of this work. In this study, for any simulation, values for $\mathbf{R}(\omega)$, $\mathbf{L}(\omega)$, $\mathbf{G}(\omega)$, and $\mathbf{C}(\omega)$ will be assumed to be available for each transmission line encountered; they can be measured or calculated by one of the several available techniques [36]-[41].

In order to characterize multiconductor systems by the line-parameter matrices, the modes of propagation must be transverse electromagnetic (TEM) or quasi-TEM. In multiconductor transmission line systems with conductor losses, whether the systems are constructed with homogeneous or nonhomogeneous dielectrics, the existence of purely TEM modes is not possible; however, as long as the losses are small, quasi-TEM modes can propagate. In fact, as long as the wavelength of the highest frequency under consideration is long compared to the greatest cross-sectional distance of the system, only quasi-TEM modes can propagate. In addition to these implicit constraints, it also will be assumed that the line is of uniform cross section throughout its length; that is, $\mathbf{R}$, $\mathbf{L}$, $\mathbf{G}$, and $\mathbf{C}$ are assumed to be constant with respect to the spacial variable x.

Proceeding now to the solution of Eq. (3.2), substituting Eq. (3.2b) into the derivative of Eq. (3.2a) and Eq. (3.2a) into the derivative of Eq. (3.2b) yields one equation in terms of the line voltages and another in terms of the line currents:

$$\frac{\partial^2 \mathbf{V}}{\partial x^2} = \mathbf{ZYV} = \Gamma^2 \mathbf{V} \tag{3.3a}$$

$$\frac{\partial^2 \mathbf{I}}{\partial x^2} = \mathbf{YZI} = \mathbf{Y}^T \mathbf{Z}^T \mathbf{I} = (\mathbf{ZY})^T \mathbf{I} = (\Gamma^2)^T \mathbf{I} \tag{3.3b}$$

where the propagation matrix Γ has been introduced. In Eq. (3.3a), $\Gamma^2 = \mathbf{ZY}$ has been defined, and due to the symmetry of $\mathbf{Z}$ and $\mathbf{Y}$, $\mathbf{YZ}$ then equals $(\Gamma^2)^T$ as shown in Eq. (3.3b). In general, even though $\mathbf{Z}$ and $\mathbf{Y}$ are symmetric, Γ^2 is not. If the existence of two

nonsingular square matrices $\mathbf{E}$ and $\mathbf{J}$ is assumed, then left-multiplying both sides of Eq. (3.3a) by $\mathbf{E}^{-1}$ and both sides of Eq. (3.3b) by $\mathbf{J}^{-1}$ results in

$$\frac{\partial^2 \mathbf{E}^{-1}\mathbf{V}}{\partial x^2} = \mathbf{E}^{-1}\Gamma^2\mathbf{E}\mathbf{E}^{-1}\mathbf{V} \tag{3.4a}$$

$$\frac{\partial^2 \mathbf{J}^{-1}\mathbf{I}}{\partial x^2} = \mathbf{J}^{-1}(\Gamma^2)^T\mathbf{J}\mathbf{J}^{-1}\mathbf{I} \tag{3.4b}$$

where the identity matrix has been inserted in the right-hand sides of Eqs. (3.4a) and (3.4b) as $\mathbf{E}\mathbf{E}^{-1}$ and $\mathbf{J}\mathbf{J}^{-1}$, respectively. The matrix products $\mathbf{E}^{-1}\Gamma^2\mathbf{E}$ and $\mathbf{J}^{-1}(\Gamma^2)^T\mathbf{J}$ in Eq. (3.4) represent similarity transformations of Γ^2 and $(\Gamma^2)^T$, respectively. If there exists n independent eigenvectors of Γ^2 and n independent eigenvectors of $(\Gamma^2)^T$, and the columns of $\mathbf{E}$ and $\mathbf{J}$ are chosen, respectively, to be these eigenvectors, then the aforementioned similarity transformations result in diagonal matrices. The existence of eigenvectors that diagonalize Γ^2 and $(\Gamma^2)^T$ will be assumed throughout this investigation. In fact, it is well known that a matrix and its transpose are similar to the same diagonal matrix [42]; designating this matrix as Λ^2 yields

$$\Lambda^2 = \mathbf{E}^{-1}\Gamma^2\mathbf{E} = \mathbf{J}^{-1}(\Gamma^2)^T\mathbf{J} \tag{3.5}$$

The diagonal elements of Λ^2 are the eigenvalues of Γ^2 and $(\Gamma^2)^T$. Their square roots are the complex quasi-TEM propagation modes of the lossy multiconductor transmission line; for this reason, Λ will be referred to as the modal propagation matrix. The jth columns of $\mathbf{E}$ and $\mathbf{J}$ are the voltage and current eigenvectors, respectively, associated with the jth eigenvalue of Λ^2. Now substituting Eq. (3.5) into Eq. (3.4) and defining the modal variables $\mathbf{V}_m = \mathbf{E}^{-1}\mathbf{V}$ and $\mathbf{I}_m = \mathbf{J}^{-1}\mathbf{I}$ lead to

$$\frac{\partial^2 \mathbf{V}_m}{\partial x^2} = \Lambda^2\mathbf{V}_m \tag{3.6a}$$

$$\frac{\partial^2 \mathbf{I}_m}{\partial x^2} = \Lambda^2 \mathbf{I}_m \tag{3.6b}$$

The modal voltage equation, Eq. (3.6a), and the modal current equation, Eq. (3.6b), can be solved independently of one another. First, the solution to the voltage equation will be derived. Since Λ^2 is diagonal, the individual equations in Eq. (3.6a) are decoupled. This means, for instance, that modal voltage V_{jm}, the jth element of $\mathbf{V}_m$, depends only on the derivative of V_{jm} and no other modal voltages; therefore, Eq. (3.6a) is actually n separate scalar equations of the form

$$\frac{\partial^2 V_{jm}}{\partial x^2} = \lambda_j^2 V_{jm}$$

where λ_j is the jth diagonal element of Λ and is the propagation constant for mode j. The solution of this equation is

$$V_{jm} = e^{-\lambda_j x} V_{jm}^{+} + e^{\lambda_j x} V_{jm}^{-}$$

where V_{jm}^{+} and V_{jm}^{-} are scalar constants that depend on the boundary conditions. Consequently, the solution of Eq. (3.6a) can be written in matrix form as

$$\mathbf{V}_m = e^{-\Lambda x} \mathbf{V}_m^{+} + e^{\Lambda x} \mathbf{V}_m^{-} \tag{3.7}$$

where $e^{-\Lambda x}$, the modal exponential propagation matrix, is a diagonal matrix whose jth diagonal element is $e^{-\lambda_j x}$, and $\mathbf{V}_m^{+}$ and $\mathbf{V}_m^{-}$ are vector constants. Multiplying each side of Eq. (3.7) on the left by $\mathbf{E}$ and inserting the identity matrix as $\mathbf{E}^{-1}\mathbf{E}$ in each term on the right-hand side result in

$$\mathbf{E}\mathbf{V}_m = \mathbf{E}e^{-\Lambda x}\mathbf{E}^{-1}\mathbf{E}\mathbf{V}_m^{+} + \mathbf{E}e^{\Lambda x}\mathbf{E}^{-1}\mathbf{E}\mathbf{V}_m^{-}$$

Making use of a previous definition relating modal voltages and line voltages [$\mathbf{V} = \mathbf{E}\mathbf{V}_m$] and the fact from matrix algebra that $\mathbf{E}e^{-\Lambda x}\mathbf{E}^{-1} = e^{-\mathbf{E}\Lambda\mathbf{E}^{-1}x}$ [42] yields

$$\mathbf{V} = e^{-\mathbf{E}\Lambda\mathbf{E}^{-1}x}\mathbf{V}^{+} + e^{\mathbf{E}\Lambda\mathbf{E}^{-1}x}\mathbf{V}^{-}$$

where line-voltage constants $\mathbf{V}^{+} = \mathbf{E}\mathbf{V}_m^{+}$ and $\mathbf{V}^{-} = \mathbf{E}\mathbf{V}_m^{-}$ have been defined. Now utilizing the definition of Λ from Eq. (3.5), the solution for the voltage as a function of x is obtained:

$$\mathbf{V} = e^{-\Gamma x}\mathbf{V}^{+} + e^{\Gamma x}\mathbf{V}^{-} \tag{3.8}$$

where $e^{-\Gamma x}$, the exponential propagation matrix, has been introduced. The first term on the right-hand side of Eq. (3.8) describes a vector of positive traveling waves, while the second term represents a vector of negative traveling waves. To find the solution for the current, Eq. (3.8) is substituted into Eq. (3.2a). Taking the derivative and rearranging some terms lead to

$$\mathbf{Z}_0\mathbf{I} = e^{-\Gamma x}\mathbf{V}^{+} - e^{\Gamma x}\mathbf{V}^{-} \tag{3.9}$$

where

$$\mathbf{Z}_0 = \Gamma^{-1}\mathbf{Z} \tag{3.10}$$

is called the characteristic impedance matrix. From Eqs. (3.8) and (3.9), it can be seen that $\mathbf{Z}_0$ relates the positive and negative traveling voltage waves to the positive and negative traveling current waves, respectively. As shown in Sec. 3.2.2, the characteristic impedance matrix $\mathbf{Z}_0$ is symmetric. Equations (3.8) and (3.9) are the solution to the lossy multiconductor transmission line equation, Eq. (3.2). Note that the solution has $2n$ independent constants $\mathbf{V}^{+}$ and $\mathbf{V}^{-}$ that depend on the boundary conditions.

A different form of the solution of Eq. (3.2) can be obtained by solving the modal current equation, Eq. (3.6b). If this is done, the solutions for the current and voltage are obtained as

$$\mathbf{I} = e^{-\Gamma^T x}\mathbf{I}^+ - e^{\Gamma^T x}\mathbf{I}^- \tag{3.11a}$$

$$\mathbf{Y}_0\mathbf{V} = e^{-\Gamma^T x}\mathbf{I}^+ + e^{\Gamma^T x}\mathbf{I}^- \tag{3.11b}$$

where

$$\mathbf{Y}_0 = (\Gamma^T)^{-1}\mathbf{Y} \tag{3.12}$$

is the characteristic admittance matrix and $\mathbf{I}^+$ and $\mathbf{I}^-$ are constant vectors. The minus sign preceding the second term in Eq. (3.11a) arises from the fact that $\mathbf{I}^-$ is defined as positive in the opposite direction of $\mathbf{I}^+$, which has the same reference direction as the total current $\mathbf{I}$ (see Fig. 3.1). As might be expected, $\mathbf{Y}_0$ is the inverse of $\mathbf{Z}_0$. This is shown to be the case in Sec. 3.2.2. Note that this means that $\mathbf{Y}_0$ is also symmetric.

Equations (3.8), (3.9), (3.11a), and (3.11b) will be used in Sec. 3.3 to derive two time-domain models for a lossy multiconductor transmission line. But first, in the next two subsections, a discussion of the line-parameter matrices and several auxiliary proofs are given.

3.2.1 Interpretation of the line-parameter matrices

A physical interpretation of $\mathbf{R}(\omega)$, $\mathbf{L}(\omega)$, $\mathbf{G}(\omega)$, and $\mathbf{C}(\omega)$ may be obtained by generalizing the definitions of their corresponding scalar-valued parameters. Referring to Fig. 3.1, say that line j has been charged to one volt (in the time-harmonic sense) with all other lines held at a voltage of zero; then, C_{ij}, the ijth entry of $\mathbf{C}$, is equal to the charge per unit length induced on line i. The off-diagonal elements of $\mathbf{C}$, sometimes called electrostatic inductance coefficients, are always negative. The diagonal entries, on the other hand, are always positive and are the self-capacitances of the individual lines of the n-line system.

The conductance matrix **G** can be analyzed in a similar manner. Again, with line j charged to one volt and all other lines at zero volts, the net current leaving line i per unit length is entry G_{ij} of **G**. As is the case with the capacitance entries, $G_{ij} < 0$ for $i \neq j$, while $G_{jj} > 0$. As one might expect, an entry in **L**, such as L_{ij}, measures the flux per unit length linking the loop formed by line i and the reference conductor due to a one-amp current flowing in line j. Of course, diagonal entries represent self-inductances while off-diagonal entries are referred to as mutual inductances. Entry R_{ij} of **R** measures the voltage drop along line i per unit length due to a one-amp current flowing in line j. For $i = j$, this is simply the usual line resistance. For $i \neq j$, it may seem impossible that current in a conductor can cause a voltage drop in a conductor other than itself. Strictly speaking it cannot; however, just as the skin effect of an isolated conductor can cause a redistribution of current that results in an effective increase in resistance of that conductor, the time-varying current in a line can also cause a redistribution of current in a neighboring line. Therefore, the effective resistance of a conductor in the neighborhood of other current-carrying conductors depends on those currents. This dependency is modeled by the off-diagonal elements of **R**.

3.2.2 Proof that $\mathbf{Z}_0 = \mathbf{Z}_0^T$ and $\mathbf{Y}_0 = \mathbf{Z}_0^{-1}$

That $\mathbf{Z}_0$ is symmetric and its inverse equal to $\mathbf{Y}_0$ are commonly used facts; nevertheless, complete and efficient proofs are hard to find. For instance, the symmetry of $\mathbf{Z}_0$ has been argued based on reciprocity [4] even though such reasoning should be reserved for fundamental physical relations such as the line-parameter matrices; other proofs have been either incomplete [5] or, in the corresponding lossless-line case, inefficient [18].

First, it must be shown that the matrix product $\mathbf{E}^{-1}\mathbf{Z}\mathbf{J}$ commutes with Λ^{-1}, that is,

$$\mathbf{E}^{-1}\mathbf{Z}\mathbf{J}\Lambda^{-1} = \Lambda^{-1}\mathbf{E}^{-1}\mathbf{Z}\mathbf{J} \tag{3.13}$$

The starting point is the definition of Λ^2 from Eq. (3.5):

$$\mathbf{E}^{-1}\Gamma^2\mathbf{E} = \mathbf{J}^{-1}(\Gamma^2)^T\mathbf{J} = \Lambda^2$$

Substituting $\mathbf{ZY}$ for Γ^2 and remembering that $\mathbf{Z}$ and $\mathbf{Y}$ are symmetric yield

$$\mathbf{E}^{-1}\mathbf{ZYE} = \mathbf{J}^{-1}\mathbf{YZJ} = \Lambda^2$$

Inserting the identity matrix as $\mathbf{JJ}^{-1}$ into one definition of Λ^2 and as $\mathbf{EE}^{-1}$ into the other definition results in

$$\mathbf{E}^{-1}\mathbf{ZJJ}^{-1}\mathbf{YE} = \mathbf{J}^{-1}\mathbf{YEE}^{-1}\mathbf{ZJ} = \Lambda^2$$

Defining $\mathbf{A_Z} = \mathbf{E}^{-1}\mathbf{ZJ}$ and $\mathbf{A_Y} = \mathbf{J}^{-1}\mathbf{YE}$, the preceding equation can be rewritten as

$$\mathbf{A_Z A_Y} = \mathbf{A_Y A_Z} = \Lambda^2$$

Now, since $\mathbf{A_Z}$ and $\mathbf{A_Y}$ commute with each other, they also commute with their product Λ^2 and its inverse Λ^{-2}. Also, since Λ^{-2} is diagonal, its square root Λ^{-1} is diagonal. Therefore, $\mathbf{A_Z}$ and $\mathbf{A_Y}$ also commute with Λ^{-1}, and Eq. (3.13) is proved.

To show that $\mathbf{Z}_0 = \mathbf{Z}_0^T$, one begins with $\mathbf{Z}_0 = \Gamma^{-1}\mathbf{Z}$ [Eq. (3.10)]; then,

$$\mathbf{Z}_0^T = (\Gamma^{-1}\mathbf{Z})^T = \mathbf{Z}(\Gamma^T)^{-1} = \mathbf{ZJ}\Lambda^{-1}\mathbf{J}^{-1} = \mathbf{EE}^{-1}\mathbf{ZJ}\Lambda^{-1}\mathbf{J}^{-1}$$

Using Eq. (3.13) yields the desired result:

$$\mathbf{Z}_0^T = \mathbf{E}\Lambda^{-1}\mathbf{E}^{-1}\mathbf{ZJJ}^{-1} = \mathbf{E}\Lambda^{-1}\mathbf{E}^{-1}\mathbf{Z} = \Gamma^{-1}\mathbf{Z} = \mathbf{Z}_0$$

Next, multiplying $\mathbf{Z}_0 = \Gamma^{-1}\mathbf{Z}$ by $\mathbf{Y}_0 = (\Gamma^T)^{-1}\mathbf{Y}$ [Eq. (3.12)], one obtains

$$\mathbf{Z}_0\mathbf{Y}_0 = \Gamma^{-1}\mathbf{Z}(\Gamma^T)^{-1}\mathbf{Y} = \mathbf{E}\Lambda^{-1}\mathbf{E}^{-1}\mathbf{ZJ}\Lambda^{-1}\mathbf{J}^{-1}\mathbf{Y}$$

Using Eq. (3.13) again leads to

$$\mathbf{Z}_0\mathbf{Y}_0 = \mathbf{E}\Lambda^{-1}\Lambda^{-1}\mathbf{E}^{-1}\mathbf{ZJJ}^{-1}\mathbf{Y} = \Gamma^{-2}\Gamma^2 = \mathbf{1}$$

where $\mathbf{1}$ is the identity matrix, and so $\mathbf{Y}_0 = \mathbf{Z}_0^{-1}$.

3.3 Time-Domain Models

In this section, two time-domain models for a lossy multiconductor transmission line are developed. One of these is based on Eqs. (3.8) and (3.9), the solution to the modal voltage equation, and results in a discretized Thevenin equivalent circuit for each end of the transmission line; the other is based on Eqs. (3.11a) and (3.11b), the solution to the modal current equation, and leads to discretized Norton equivalent circuits. The Thevenin equivalent model will be developed first. Both the space dependence and frequency/time dependence of the equations will be needed; consequently, they will be shown explicitly in the following derivation. Equations (3.8) and (3.9) are rewritten here for convenience:

$$\mathbf{V}(x,\omega) = e^{-\Gamma(\omega)x}\mathbf{V}^{+}(\omega) + e^{\Gamma(\omega)x}\mathbf{V}^{-}(\omega) \tag{3.14a}$$

$$\mathbf{Z}_0(\omega)\mathbf{I}(x,\omega) = e^{-\Gamma(\omega)x}\mathbf{V}^{+}(\omega) - e^{\Gamma(\omega)x}\mathbf{V}^{-}(\omega) \tag{3.14b}$$

Defining $\mathbf{V}^{+}(x,\omega) = e^{-\Gamma(\omega)x}\mathbf{V}^{+}(\omega)$ and $\mathbf{V}^{-}(x,\omega) = e^{\Gamma(\omega)x}\mathbf{V}^{-}(\omega)$ and evaluating these equations at $x = 0$ yield

$$\mathbf{V}^{+}(x,\omega) = e^{-\Gamma(\omega)x}\mathbf{V}^{+}(0,\omega) \tag{3.15a}$$

$$\mathbf{V}^{-}(x,\omega) = e^{\Gamma(\omega)x}\mathbf{V}^{-}(0,\omega) \tag{3.15b}$$

Substituting Eq. (3.15) into Eq. (3.14) and evaluating the result at $x = 0$ lead to

$$\mathbf{V}(0,\omega) = \mathbf{V}^{+}(0,\omega) + \mathbf{V}^{-}(0,\omega) \tag{3.16a}$$

$$\mathbf{Z}_0(\omega)\mathbf{I}(0,\omega) = \mathbf{V}^{+}(0,\omega) - \mathbf{V}^{-}(0,\omega) \tag{3.16b}$$

From Eq.(3.15b), one notices that $\mathbf{V}^{-}(0,\omega)$ can be expressed as $\mathbf{V}^{-}(d,\omega)e^{-\Gamma(\omega)d}$ where d is the length of the multiconductor line. If this expression is substituted into Eqs. (3.16a) and (3.16b), then adding the respective sides of the two resulting equations and rearranging terms yield

$$\mathbf{V}(0,\omega) = 2e^{-\Gamma(\omega)d}\mathbf{V}^{-}(d,\omega) + \mathbf{Z}_0(\omega)\mathbf{I}(0,\omega) \tag{3.17}$$

Equation (3.17) expresses the near-end ($x = 0$) voltage in terms of the near-end current, the far-end ($x = d$) reflected voltages, and the transfer function matrices $\mathbf{Z}_0(\omega)$ and $e^{-\Gamma(\omega)d}$. Similarly, starting with Eq. (3.14) evaluated at the far end:

$$\mathbf{V}(d,\omega) = e^{-\Gamma(\omega)d}\mathbf{V}^{+}(0,\omega) + e^{\Gamma(\omega)d}\mathbf{V}^{-}(0,\omega) \tag{3.18a}$$

$$-\mathbf{Z}_0(\omega)\mathbf{I}(d,\omega) = e^{-\Gamma(\omega)d}\mathbf{V}^{+}(0,\omega) - e^{\Gamma(\omega)d}\mathbf{V}^{-}(0,\omega) \tag{3.18b}$$

an equation is obtained that expresses the voltage at the far end in terms of the far-end currents, the near-end reflected voltages, and the transfer function matrices:

$$\mathbf{V}(d,\omega) = 2e^{-\Gamma(\omega)d}\mathbf{V}^{+}(0,\omega) + \mathbf{Z}_0(\omega)\mathbf{I}(d,\omega) \tag{3.19}$$

Note that a negative sign appears on the left-hand side of Eq. (3.18b) where its seems there should be none. In the original lossy multiconductor transmission line equations, Eq. (3.2), the reference direction for the current was chosen in the positive x direction as depicted in Fig. 3.1. For symmetry purposes, it is more convenient to choose the reference direction for the current at each end of the line to be into the line. This necessitates the introduction of the negative sign in Eq. (3.18b).

Before transforming Eqs. (3.17) and (3.19) to the time domain, a modification will be made to the characteristic impedance matrix $\mathbf{Z}_0$. In general, as ω approaches infinity, $\mathbf{Z}_0(\omega)$ approaches a real constant matrix; therefore, $\mathbf{Z}_0$ will be separated into the sum of two terms as shown below:

$$\mathbf{Z}_0(\omega) = \mathbf{Z}_{0s}(\omega) + \mathbf{R}_0 \tag{3.20}$$

where $\mathbf{R}_0$ is defined as the limit of $\mathbf{Z}_0(\omega)$ as ω goes to infinity:

$$\mathbf{R}_0 = \lim_{\omega\to\infty} \mathbf{Z}_0(\omega) \tag{3.21}$$

Equations (3.20) and (3.21) can be taken to define the "shifted" characteristic impedance matrix $\mathbf{Z}_{0s}(\omega)$. The time-domain Thevenin companion model for the lossy multiconductor transmission line can now be constructed. Since Eqs. (3.17) and (3.19) have the same form, it will be necessary to show a detailed derivation for only one end of the line. Working with the far end, Eq. (3.20) is substituted into Eq. (3.19) to obtain

$$\mathbf{V}(d,\omega) = 2e^{-\Gamma(\omega)d}\mathbf{V}^{+}(0,\omega) + \mathbf{Z}_{0s}(\omega)\mathbf{I}(d,\omega) + \mathbf{R}_0\mathbf{I}(d,\omega) \tag{3.22}$$

Switching to the time domain, the inverse Fourier transform of this equation is taken with respect to ω to arrive at

$$\mathbf{V}(d,t) = 2\mathbf{H}(d,t) * \mathbf{V}^{+}(0,t) + \mathbf{Z}_{0s}(t) * \mathbf{I}(d,t) + \mathbf{R}_0\mathbf{I}(d,t) \tag{3.23}$$

where the asterisk denotes convolution and

$$\mathbf{H}(d,t) = \mathfrak{F}^{-1}\{e^{-\Gamma(\omega)d}\}$$

in which $\mathfrak{F}$ denotes the Fourier transform with respect to t. Explicitly showing the convolution integral evaluated at time $t = t_k$ leads to

$$\mathbf{V}(d,t_k) = 2\int_0^{t_k}\mathbf{H}(d,\tau)\mathbf{V}^{+}(0,t_k-\tau)d\tau + \int_0^{t_k}\mathbf{Z}_{0s}(\tau)\mathbf{I}(d,t_k-\tau)d\tau + \mathbf{R}_0\mathbf{I}(d,t_k) \tag{3.24}$$

In the computer implementation of this equation, the integrals must be approximated by finite sums. Rewriting Eq. (3.24) using finite sums results in

$$\mathbf{V}(d,t_k) = 2\sum_{l=0}^{k-1}\mathbf{H}(d,t_l)\mathbf{V}^{+}(0,t_k-t_{l+1})\Delta t + \sum_{l=0}^{k-1}\mathbf{Z}_{0s}(t_l)\mathbf{I}(d,t_k-t_{l+1})\Delta t + \mathbf{R}_0\mathbf{I}(d,t_k) \tag{3.25}$$

The vector $\mathbf{V}^{+}(0,t_l)$, $l=1,\ldots,k$, shown in the first term on the right-hand side of the above equation consists of all of the reflected voltages that have been placed on the line at the near end since the beginning of the simulation. In Eq. (3.24) $\mathbf{H}(d,\tau)$ and $\mathbf{Z}_{0s}(\tau)$ are impulse

response matrices; this means, for instance, that $\mathbf{H}(d,t_l)$, l=0,...,k–1, in Eq. (3.25) is a pulse response matrix. This pulse response matrix takes the pulses $\mathbf{V}^+(0,t_l)\Delta t$, l=1,...,k, that are placed on the line at $x = 0$ and propagates them down the line to the far end; therefore, the summation in the first term is just the positive-going voltage wave vector arriving at $x = d$ at time t_k, that is, $\mathbf{V}^+(d,t_k)$. The second summation on the right-hand side of Eq. (3.25) involves the product of the pulse response matrix $\mathbf{Z}_{0s}(t_l)$, l=0,...,k–1, and a vector of past current pulses at the far end of the line. It results in a "past-history" voltage source that represents, to a certain extent, the history at the boundary between the line and its termination at the far end since the beginning of the simulation. This voltage source will be designated $\mathbf{V}_h(d,t_k)$. Summarizing, the following variables have been defined:

$$\mathbf{V}^+(d,t_k) = \sum_{l=0}^{k-1} \mathbf{H}(d,t_l)\mathbf{V}^+(0,t_k-t_{l+1})\Delta t \tag{3.26a}$$

$$\mathbf{V}_h(d,t_k) = \sum_{l=0}^{k-1} \mathbf{Z}_{0s}(t_l)\mathbf{I}(d,t_k-t_{l+1})\Delta t \tag{3.26b}$$

Substituting these variables into Eq. (3.25) leads to

$$\mathbf{V}(d,t_k) = 2\mathbf{V}^+(d,t_k) + \mathbf{V}_h(d,t_k) + \mathbf{R}_0\mathbf{I}(d,t_k) \tag{3.27}$$

This equation expresses the voltage at the far end at time t_k in terms of the far-end currents, the constant resistance matrix $\mathbf{R}_0$, and two known voltages; it is the time domain counterpart of Eq. (3.19). A similar derivation leads to an equation for the near end of the line. This equation may be written as

$$\mathbf{V}(0,t_k) = 2\mathbf{V}^-(0,t_k) + \mathbf{V}_h(0,t_k) + \mathbf{R}_0\mathbf{I}(0,t_k) \tag{3.28}$$

where

$$\mathbf{V}^-(0,t_k) = \sum_{l=0}^{k-1} \mathbf{H}(d,t_l)\mathbf{V}^-(d,t_k-t_{l+1})\Delta t \tag{3.29a}$$

$$\mathbf{V}_h(0,t_k) = \sum_{l=0}^{k-1} \mathbf{Z}_{0s}(t_l)\mathbf{I}(0,t_k - t_{l+1})\Delta t \qquad (3.29b)$$

A lumped-element companion model for the lossy multiconductor line can now be developed from Eqs. (3.27) and (3.28). The first two terms of the right-hand side of each equation can be represented by a voltage source, while the third term indicates that the currents at each end of the line pass through a system of coupled resistances. The value of the voltage source is the open-circuit voltage at time t_k that results from an incident wave. The set of coupled resistances represented by the matrix $\mathbf{R}_0$ is the instantaneous resistance looking back into an infinite lossy multiconductor transmission line. This justifies the use of the term Thevenin companion model for the equivalent circuit illustrated in Fig. 3.2. In this figure, the resistance matrices are shown in block-diagram form. These matrices can be implemented in a manner identical to the resistance matrix encountered in Chapter 2 for the discretized coupled inductors: the diagonal elements of the matrix can be modeled as two-terminal resistors, and the off-diagonal elements as current-controlled voltage sources. Since the model for the lossy multiconductor transmission line can be expressed as an assemblage of lumped elements, it can be easily included in any circuit analysis program. This has been a major goal of this research.

The element stamp for the far end of the line is shown in Fig. 3.3. Since the model contains voltage sources in each line, the line currents are also introduced as variables via the branch equations, Eq. (3.27). These currents are needed in any case because their values must be saved so that they are available for convolution with $\mathbf{Z}_{0s}(t)$. The topology of the stamp for the near end of the line is identical to that for the far end and, therefore, is not shown.

A Norton companion model for the lossy multiconductor transmission line, consisting of current sources in parallel with coupled conductances, can be derived starting

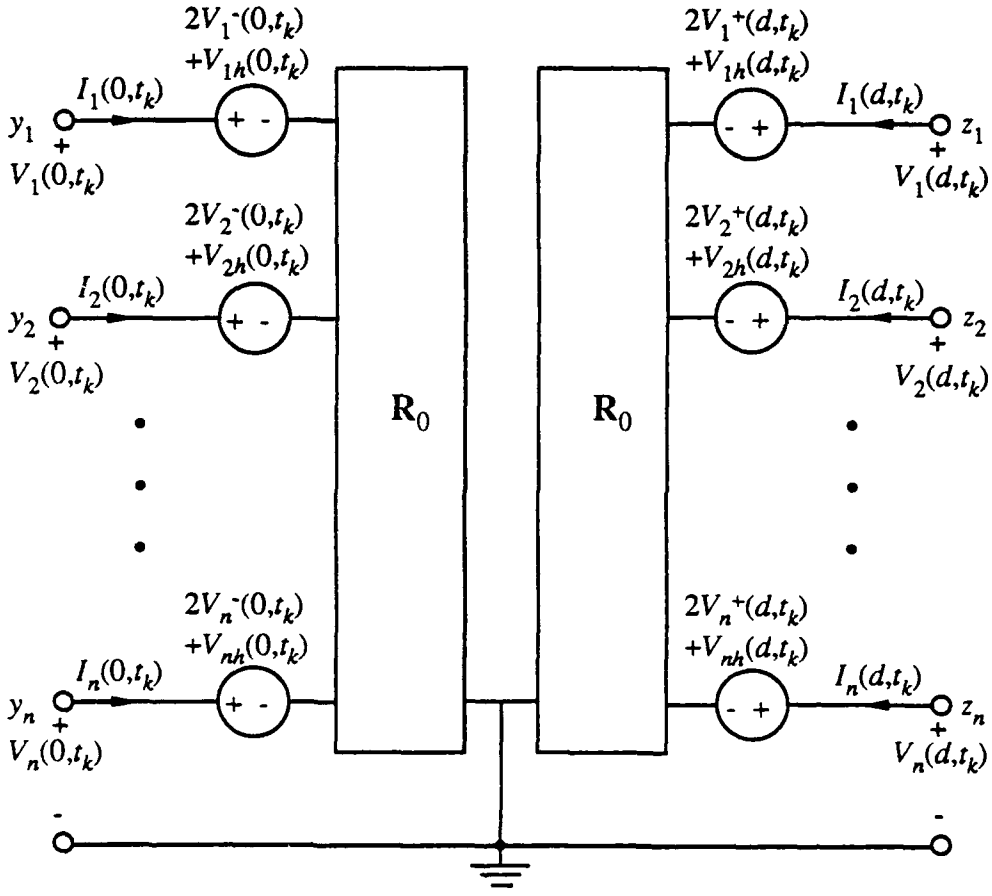

Figure 3.2 Thevenin companion model at time t_k for a lossy $(n+1)$-conductor transmission line of length d.

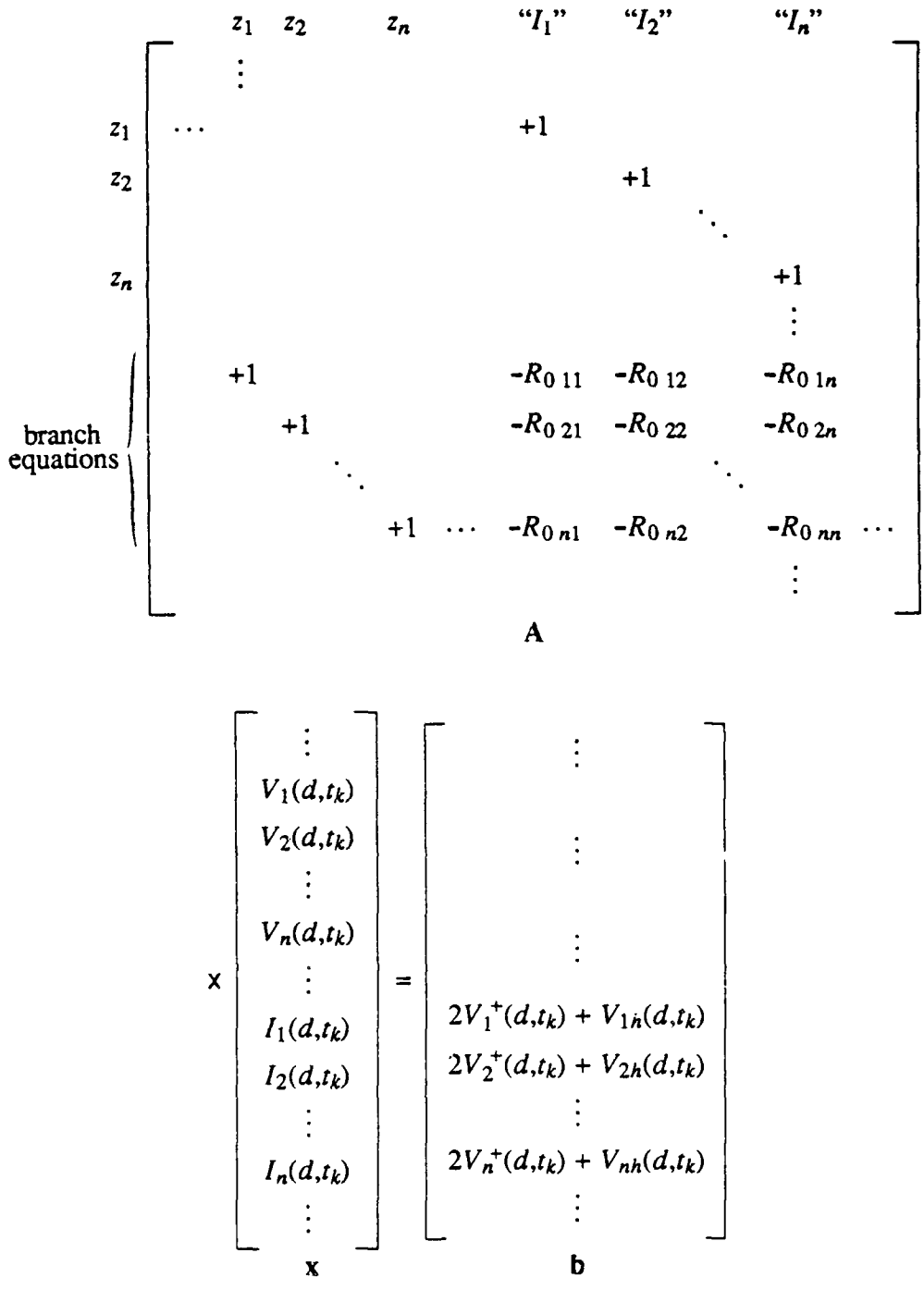

Figure 3.3 Element stamp associated with the Thevenin companion model of Figure 3.2. This stamp is for the far end of the line only.

from Eqs. (3.11a) and (3.11b). These are repeated here for convenience with the independent variables explicitly shown:

$$\mathbf{I}(x,\omega) = e^{-\Gamma^T(\omega)x}\mathbf{I}^+(0,\omega) - e^{\Gamma^T(\omega)x}\mathbf{I}^-(0,\omega) \tag{3.30a}$$

$$\mathbf{Y}_0(\omega)\mathbf{V}(x,\omega) = e^{-\Gamma^T(\omega)x}\mathbf{I}^+(0,\omega) + e^{\Gamma^T(\omega)x}\mathbf{I}^-(0,\omega) \tag{3.30b}$$

Following a development analogous to that conducted for the modal voltage equation, one arrives at the following equations that describe the line-end currents as functions of the line-end voltages, the reflected currents at the opposite end, and the transfer function matrices $\mathbf{Y}_0(\omega)$ and $e^{-\Gamma(\omega)^T d}$:

$$\mathbf{I}(0,\omega) = -2e^{-\Gamma(\omega)^T d}\mathbf{I}^-(d,\omega) + \mathbf{Y}_0(\omega)\mathbf{V}(0,\omega) \tag{3.31a}$$

$$\mathbf{I}(d,\omega) = -2e^{-\Gamma(\omega)^T d}\mathbf{I}^+(0,\omega) + \mathbf{Y}_0(\omega)\mathbf{V}(d,\omega) \tag{3.31b}$$

Transforming these to the time domain and discretizing them in a manner similar to the development of the Thevenin companion model lead to

$$\mathbf{I}(0,t_k) = -2\mathbf{I}^-(0,t_k) + \mathbf{I}_h(0,t_k) + \mathbf{G}_0\mathbf{V}(0,t_k) \tag{3.32a}$$

$$\mathbf{I}(d,t_k) = -2\mathbf{I}^+(d,t_k) + \mathbf{I}_h(d,t_k) + \mathbf{G}_0\mathbf{V}(d,t_k) \tag{3.32b}$$

where

$$\mathbf{G}_0 = \lim_{\omega\to\infty} \mathbf{Y}_0(\omega)$$

$$\mathbf{Y}_{0s}(\omega) = \mathbf{Y}_0(\omega) - \mathbf{G}_0$$

$$\mathbf{I}^-(0,t_k) = \sum_{l=0}^{k-1} \mathbf{H}^T(d,t_l)\mathbf{I}^-(d,t_k - t_{l+1})\Delta t$$

$$\mathbf{I}_h(0,t_k) = \sum_{l=0}^{k-1} \mathbf{Y}_{0s}(t_l)\mathbf{V}(0,t_k - t_{l+1})\Delta t$$

$$\mathbf{I}^{+}(d,t_k) = \sum_{l=0}^{k-1} \mathbf{H}^{T}(d,t_l)\mathbf{I}^{+}(0,t_k - t_{l+1})\Delta t$$

$$\mathbf{I}_h(d,t_k) = \sum_{l=0}^{k-1} \mathbf{Y}_{0s}(t_l)\mathbf{V}(d,t_k - t_{l+1})\Delta t$$

The companion model corresponding to Eqs. (3.32a) and (3.32b) is shown in Fig. 3.4, and the corresponding element stamp for the far end of the line is given in Fig. 3.5. Again, the topology of the stamp for the near end of the line is the same as that for the far end.

3.3.1 Interpretation of the impulse response matrices

It is interesting to consider the physical interpretation of the impulse response matrices $\mathbf{H}(d,t)$ and $\mathbf{Z}_0(t)$ encountered in this section. Referring to Fig. 3.6, a doubly-infinite $(n+1)$-conductor transmission line with a voltage source of value $2\delta(t)$, where $\delta(t)$ is the impulse function, is shown inserted into line j at $x = 0$. Upon application of the impulse at $t = 0$, a voltage of value $\delta(t)$ is introduced on line j at $x = 0^{+}$, and one of value $-\delta(t)$ is introduced at $x = 0^{-}$. The signal at $x = 0^{+}$ will then propagate in the positive x direction. From the solution to the multiconductor transmission line equations given by Eq. (3.8), and making use of the causality condition and the inverse Fourier transform, the value of the voltage at $x = d$ is easily found to be

$$\mathbf{V}(d,t) = \mathbf{H}(d,t) * [0 \cdots 0 \underset{j}{\delta(t)} 0 \cdots 0]^{T} \tag{3.33}$$

where the impulse occurs in the jth row of the vector. From Eq. (3.33) it is seen that $H_{ij}(d,t)$, the ijth entry of $\mathbf{H}(d,t)$, is the voltage at $x = d$ of line i in the circuit of Fig. 3.6.

Similarly, another doubly-infinite $(n+1)$-conductor transmission line is shown in Fig. 3.7, this time with a current source of value $2\delta(t)$ connected between line j and the reference conductor at $x = 0$. Upon application of the impulse at $t = 0$, half the current will travel in the positive x direction and the other half will flow in the negative x direction. The

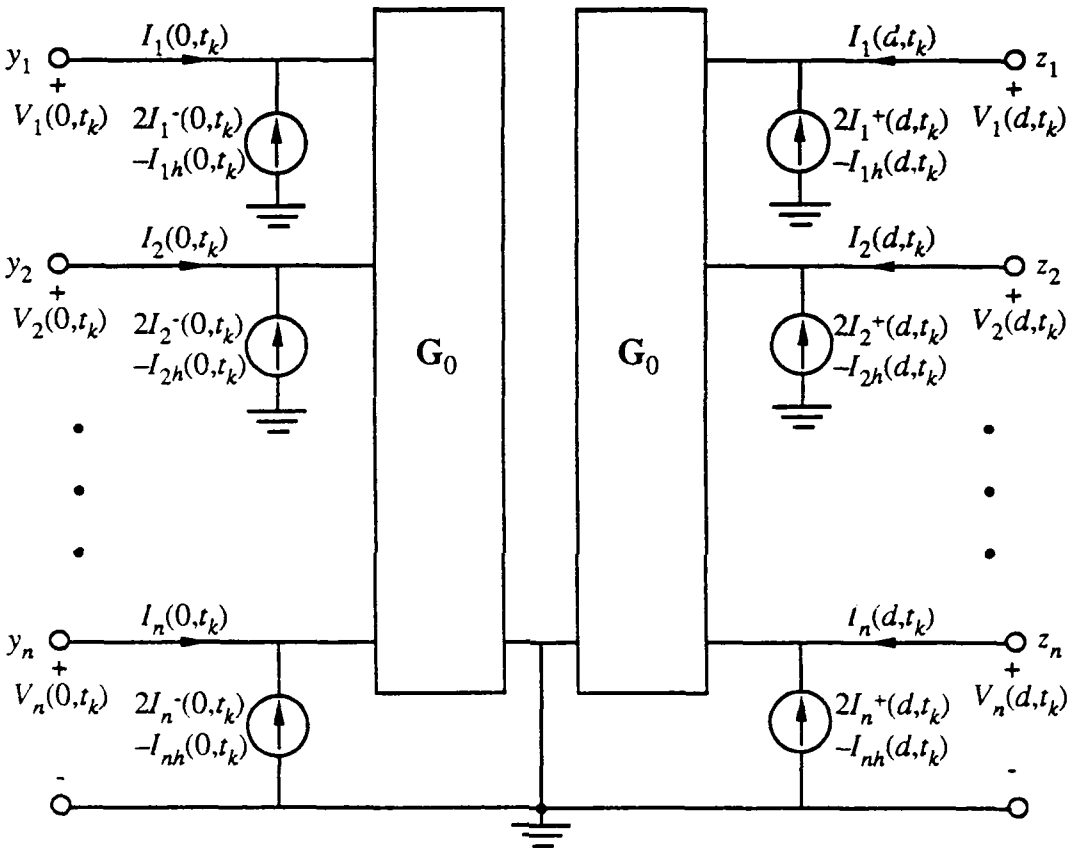

Figure 3.4 Norton companion model at time t_k for a lossy $(n+1)$-conductor transmission line of length d.

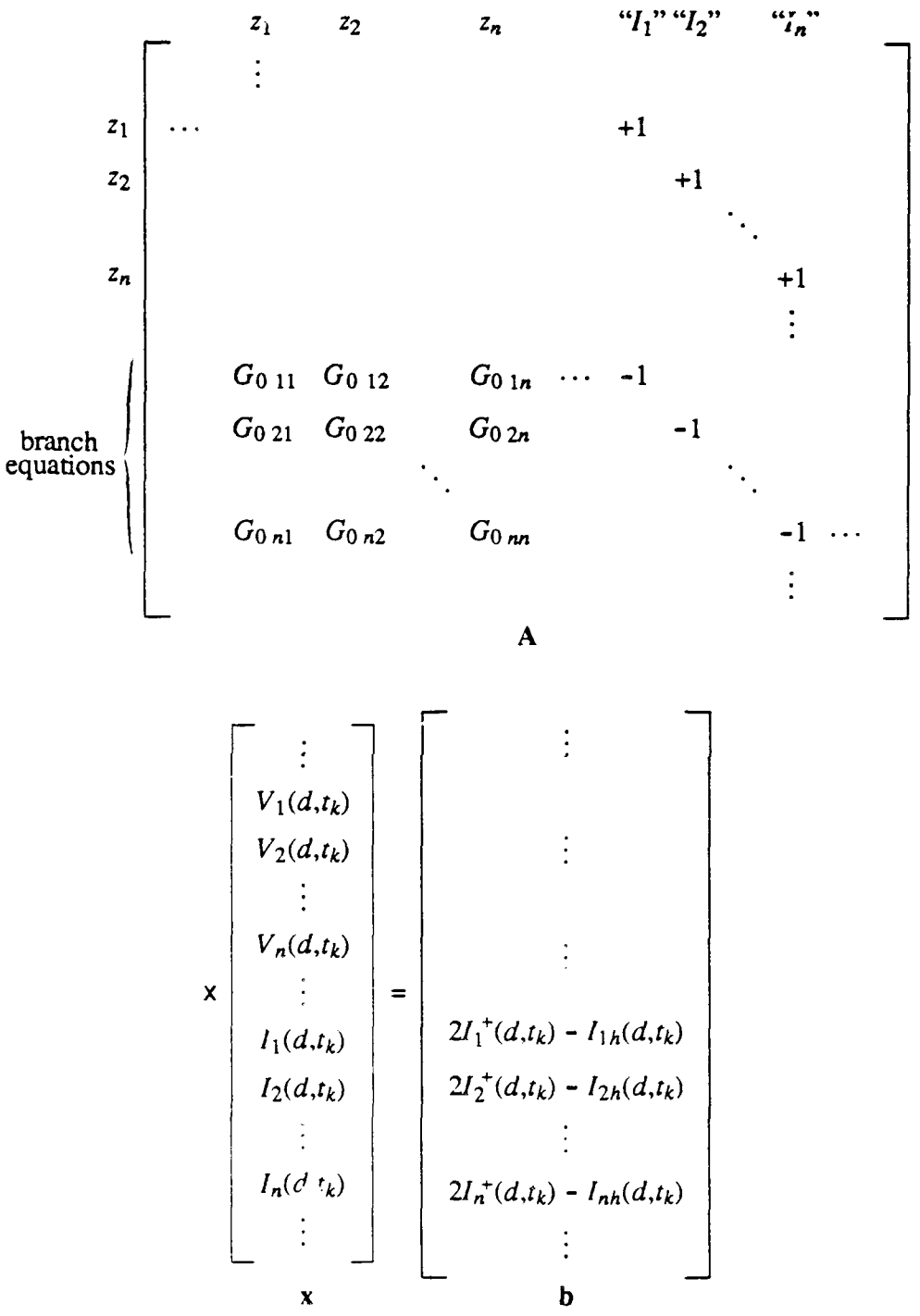

Figure 3.5 Element stamp associated with the Norton companion model of Figure 3.4. This stamp is for the far end of the line only.

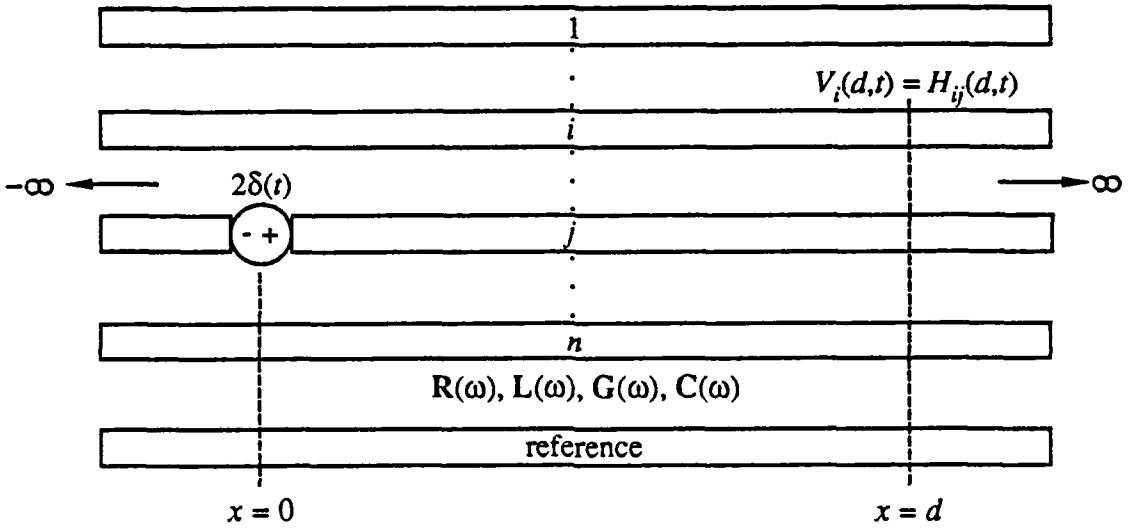

Figure 3.6 Physical interpretation of the impulse response $H_{ij}(d,t)$.

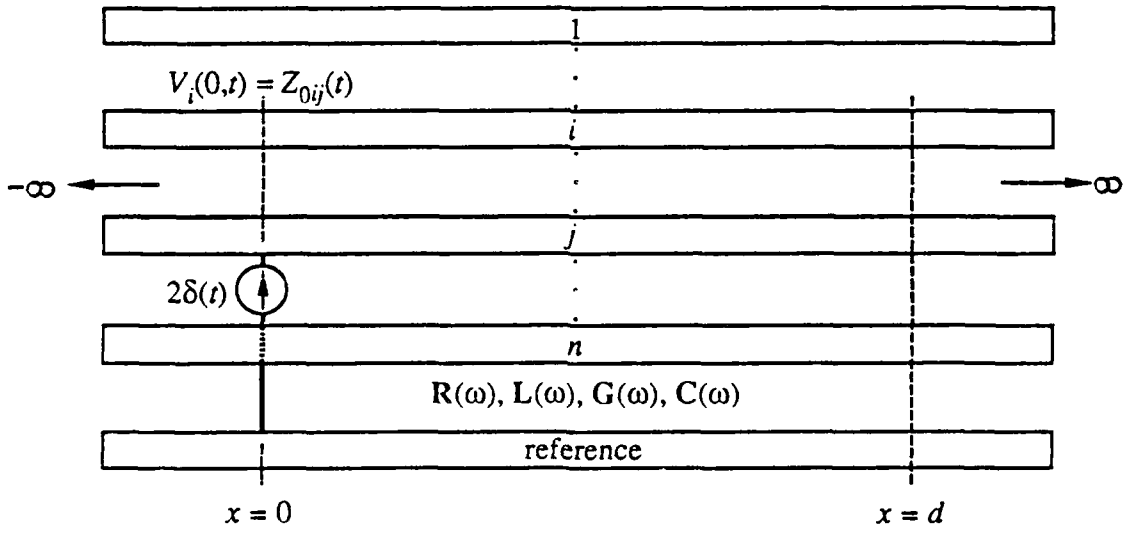

Figure 3.7 Physical interpretation of the impulse response $Z_{0ij}(t)$.

current flowing in the positive direction will see an impedance equal to the characteristic impedance of the line or $\mathbf{Z}_0(\omega)$. Therefore, in the time domain the voltage at $x = 0$ is

$$\mathbf{V}(0,t) = \mathbf{Z}_0(t) * [0 \cdots 0 \underset{j}{\delta(t)} 0 \cdots 0]^T \tag{3.34}$$

where again the impulse occurs in the jth row of the vector. From Eq. (3.34) it is seen that $Z_{0ij}(t)$, the ijth entry of $\mathbf{Z}_0(t)$, is the voltage at $x = 0$ of line i in the circuit of Fig. 3.7.

Since the multiconductor transmission lines in Figs. 3.6 and 3.7 are infinite in each direction, no reflections will occur at any time. In a lossless system, the impulse response is an impulse at $t = 0$ for each entry of $\mathbf{Z}_0(t)$ and the sum of n impulses delayed in time for each entry of $\mathbf{H}(d,t)$. In general, the delays are of different length. Since there are no reflections in the responses, their durations are finite; if the lines had been terminated by an impedance other than $\mathbf{Z}_0(\omega)$, the responses would exist for all time. In the case of lossy lines, each impulse response will have a "tail" that is due to the distortion of the line. In some sense, the length (in time) of this tail, until the value of the response is negligible, is a measure of the severity of the distortion caused by the line. As with the lossless case, the impulse responses will still be relatively short since no reflections occur. The shorter impulse responses make it simpler to carry out the inverse Fourier transform and also decrease the amount of past-history values that need to be stored. This is an inherent advantage of the modeling method presented in this chapter.

3.4 Numerical Considerations

This section contains a discussion of what is involved numerically in calculating and implementing the lossy multiconductor transmission line models in a general circuit analysis program.

The actual calculation of the matrix functions $e^{-\Gamma(\omega)d}$ or $e^{-\Gamma(\omega)^T d}$ and $\mathbf{Z}_0(\omega)$ or $\mathbf{Y}_0(\omega)$ is quite involved. The derivation from Eq. (3.7) to Eq. (3.8) yields the means of computing $e^{-\Gamma(\omega)d}$:

$$e^{-\Gamma(\omega)d} = \mathbf{E}(\omega)e^{-\Lambda(\omega)d}\mathbf{E}(\omega)^{-1}$$

Since $e^{-\Gamma(\omega)^T d} = [e^{-\Gamma(\omega)d}]^T$, it need not be considered further. Recalling the definitions of $\mathbf{Z}_0(\omega)$ and $\mathbf{Y}_0(\omega)$ from Eqs. (3.10) and (3.12):

$$\mathbf{Z}_0(\omega) = \Gamma(\omega)^{-1}\mathbf{Z}(\omega) \qquad \mathbf{Y}_0(\omega) = [\Gamma(\omega)^T]^{-1}\mathbf{Y}(\omega)$$

then making use of Eq. (3.5) and some matrix algebra lead to

$$\mathbf{Z}_0(\omega) = \mathbf{E}(\omega)\Lambda(\omega)^{-1}\mathbf{E}(\omega)^{-1}\mathbf{Z}(\omega)$$

$$\mathbf{Y}_0(\omega) = \mathbf{J}(\omega)\Lambda(\omega)^{-1}\mathbf{J}(\omega)^{-1}\mathbf{Y}(\omega)$$

However, because $\mathbf{Y}_0(\omega)^T = \mathbf{Y}_0(\omega)$ and $\mathbf{Y}(\omega)^T = \mathbf{Y}(\omega)$,

$$\mathbf{Y}_0(\omega) = \mathbf{Y}(\omega)\Gamma(\omega)^{-1} = \mathbf{Y}(\omega)\mathbf{E}(\omega)\Lambda(\omega)^{-1}\mathbf{E}(\omega)^{-1}$$

Consequently, only the voltage eigenvectors need to be calculated no matter which transmission line model is used. Before calculating the inverse transform of the variables above by a fast Fourier transform, values must be computed at discrete frequencies. This is complicated by the fact that, in general, the eigenvalues and eigenvectors of $\Gamma(\omega)$ are frequency dependent. The numerical computation of the eigenvalues and eigenvectors of a complex matrix is a difficult and time-consuming procedure; however, because they remain constant throughout a simulation, the impulse responses need only be calculated once for each lossy multiconductor transmission line of the circuit.

Because the transmission lines dealt with here are linear, the companion model for the lossy $(n+1)$-conductor transmission line need only be updated at each time step of a

simulation and not at each Newton-Raphson iteration. The summations in Eqs. (3.26a), (3.26b), (3.29a), and (3.29b) must be performed at each time step. Over the course of a simulation, each summation constitutes one-half of a convolution integral being performed in the time domain. These convolutions represent the most time-consuming operation of the analysis technique described herein. However, newer computers that use vectorized arithmetic units have the capability of performing multiplications in parallel. The convolution as developed in this investigation is essentially a dot product which is a vectorizable operation. Existing computers have the capability of speeding up this operation by a factor of fifty. In the near future, a speedup of a full two orders of magnitude may be expected.

The calculation of the inverse Fourier transforms is the most difficult numerical procedure involved in the formulation of the time-domain models. In general, each entry of $\mathbf{Z}_0(t)$ or $\mathbf{Y}_0(t)$ contains an impulse and a discontinuity at $t = 0$. The impulse occurs because $\mathbf{Z}_0(\omega)$ and $\mathbf{Y}_0(\omega)$ approach constant nonzero matrices as ω nears infinity. These impulses can be extracted easily enough by shifting the frequency domain counterpart of these matrices as was done in Sec. 3.3. A simple procedure can be used to remove the discontinuity from the shifted response that remains. Since the impulse responses are real, it follows that $\mathbf{Z}_{0s}{}^{*}(\omega) = \mathbf{Z}_{0s}(-\omega)$, for example, where the asterisk as a superscript indicates complex conjugate; then

$$2\,\mathrm{Re}\{\mathbf{Z}_{0s}(\omega)\} = \mathbf{Z}_{0s}(\omega) + \mathbf{Z}_{0s}{}^{*}(\omega) = \mathbf{Z}_{0s}(\omega) + \mathbf{Z}_{0s}(-\omega)$$

Now the inverse Fourier transform of $\mathbf{Z}_{0s}(-\omega)$ is $\mathbf{Z}_{0s}(-t)$; therefore, $2\,\mathrm{Re}\{\mathbf{Z}_{0s}(\omega)\}$ and $\mathbf{Z}_{0s}(t) + \mathbf{Z}_{0s}(-t)$ form a Fourier transform pair. But $\mathbf{Z}_{0s}(t)$ and $\mathbf{Z}_{0s}(-t)$ do not overlap because $\mathbf{Z}_{0s}(t)$ is causal; as a result, $\mathbf{Z}_{0s}(t)$ can be recovered by taking the positive-t portion of the $\mathbf{Z}_{0s}(t) + \mathbf{Z}_{0s}(-t)$ sum. The sum of these two terms is real and even; consequently, the discontinuity at the origin has been eliminated. Similar reasoning applies to the computation of $\mathbf{Y}_{0s}(t)$.

Special problems arise whenever **R** or **G** is zero. In many practical cases, a solution of sufficient accuracy may be obtained by taking **G** to be **0**, the zero matrix. Upon close examination of Eq. (3.10), it is seen that $\mathbf{Z}_0(\omega)$ will then be undefined (infinite) whenever $\omega = 0$. However, $\mathbf{Y}_0(\omega)$ is the inverse of $\mathbf{Z}_0(\omega)$; consequently, $\mathbf{Y}_0(\omega)$ will be equal to zero for $\omega = 0$. Therefore, it would seem to be advantageous to use the second formulation of the time domain model, the one that results in the Norton companion model of Fig. 3.4, whenever **G** is zero or chosen to be so. Likewise, whenever **R** is zero at $\omega = 0$ and **G** is not, it is easier to use the companion model of Fig. 3.2. If **R** and **G** both approach infinity as ω goes to zero, then in real transmission lines, both $\mathbf{Y}_0(\omega)$ and $\mathbf{Z}_0(\omega)$ are also zero and either method may be used.

The inverse transform of the exponential propagation matrix $e^{-\Gamma(\omega)d}$ is slightly more difficult to calculate than that of the impedance or admittance matrix. Imbedded in each element of the exponential matrix are n delays that correspond to the n propagation modes of an n-line system. As the frequency nears infinity, the real part of each entry of $e^{-\Gamma(\omega)d}$ approaches a sum of n sinusoids. As was mentioned in Sec. 3.3.1, this means that $\mathbf{H}(d,t)$ contains a sum of n impulse functions delayed in time by the amount that it takes the corresponding lossless modes to propagate from one end of the line to the other end. Once the modal exponential propagation matrix $e^{-\Lambda(\omega)d}$ has been recombined to the full-matrix form, there is no simple procedure to extract these impulse functions as was done for $\mathbf{Y}_0(\omega)$ and $\mathbf{Z}_0(\omega)$. In $\mathbf{Y}_0(\omega)$ and $\mathbf{Z}_0(\omega)$, these impulse functions all occur at $t = 0$ in both the modal and full-matrix forms. The effect is that $e^{-\Gamma(\omega)d}$ goes to a periodic function as ω approaches infinity. Numerically, the inverse fast Fourier transform must be of finite length; consequently, $e^{-\Gamma(\omega)d}$ must be multiplied by some window function before the transform can be calculated. A number of window functions are available for this purpose. Among these are the rectangular, triangular, von Hann, and Hamming windows. It was found that the Hamming window provided the best results. The Hamming window $w(\omega)$ is shown here to be

$$w(\omega) = 0.54 + 0.46 \cos(\omega \Delta t) \qquad -\pi/(\Delta t) < \omega < \pi/(\Delta t)$$
$$w(\omega) = 0 \qquad \text{otherwise}$$

Therefore, $\mathbf{H}(d,t)$ is calculated as

$$\mathbf{H}(d,t) = \mathbf{0} \qquad t < 0$$
$$\mathbf{H}(d,t) = \mathfrak{F}^{-1}\{2\,\mathrm{Re}\{e^{-\Gamma(\omega)d}\}w(\omega)\} \qquad t \geq 0$$

where the real-and-even scheme discussed earlier in the calculation of $\mathbf{Z}_{0s}(t)$ is also used above. The windowing results in a minor spreading of the final results that are nearly imperceptible.

Each single or multiconductor transmission line represents an inherent delay in the propagation of a signal or signals during a transient simulation. This can be seen in the impulse response matrix $\mathbf{H}(d,t)$. Because of this propagation delay, the value of $\mathbf{H}(d,0)$ is always equal to the zero matrix for any transmission line whether it is lossless or lossy. This means that during any transient simulation, lumped-element networks separated by transmission lines are effectively decoupled; that is, they do not depend upon one another. Consequently, the coefficient matrix **A** can always be reordered into a block diagonal form, and each block solved separately for each iteration of each time step. If the Thevenin companion model of Fig. 3.2 is used, for example, each half of the equivalent circuit can be considered a part of the lumped network to which it is connected. For large networks, a significant savings of computer time may result since the number of multiplications required to solve a system of linear equations varies as the cube of the order of the system. (If sparse matrix techniques are used, the number of multiplications for typical electrical networks still varies at an exponential rate of approximately 1.5.) In the typical circuit analysis program, the user must number the nodes consecutively starting from one with the reference node being zero. In order to ease the implementation of this technique in the program written for this thesis, the user must indicate the number of lumped element

networks involved in the simulation, number the nodes in each of these networks consecutively, and indicate the largest node value for each lumped-element network.

3.5 Conclusions

In the time-domain analysis of nonlinear circuits, lossy multiconductor transmission lines can be represented at each time step by discretized Thevenin equivalent circuits or discretized Norton equivalent circuits. These models contain only lumped elements so they can be easily implemented in a general circuit analysis program. The major obstacles appear to be numerical in nature, but they do not seem to be severe enough to alter the viability of the technique presented.

CHAPTER 4

RESULTS AND ANALYSIS

4.1 Introduction

In order to verify the analytical and numerical techniques developed in Chapter 3, a computer program compatible with the circuit analysis method of Chapter 2 was written incorporating the lossy multiconductor transmission line models [43]. It is an extension of an earlier program written to include lossless multiconductor transmission lines [44]. The new program can be used for the transient analysis of nonlinear circuits containing any number of lossy frequency-dependent multiconductor transmission lines. It can also handle coupled inductors and coupled capacitors of any order, as well as junction diodes and bipolar transistors. As discussed in Chapter 2, the program uses modified nodal analysis to formulate the circuit equations, the trapezoidal algorithm (with a fixed time step) for discrete integration, and the Newton-Raphson algorithm to iteratively solve systems of nonlinear equations. In this chapter, the program is demonstrated for several circuit configurations.

4.2 Simulation Examples

The first example consists of a single transmission line (with ground return) terminated by TI 74S04 (Schottky TTL) inverters. As shown in Fig. 4.1, one inverter is used as the driver of the line, and a fan-out of three inverters is used to terminate the line. The transmission line is 10.0 in. (0.254 m) long with an inductance L of 307.1 nH/m and a capacitance C of 85.3 pF/m. The frequency-dependent skin effect was modeled by a resistance $R = \max\{6.8, 0.26\sqrt{f}/10^3\}$ Ω/in. $= \max\{267.7, 10.24\sqrt{f}/10^3\}$ Ω/m where f is the frequency in Hertz. The conductance G of the dielectric was assumed to be negligible.

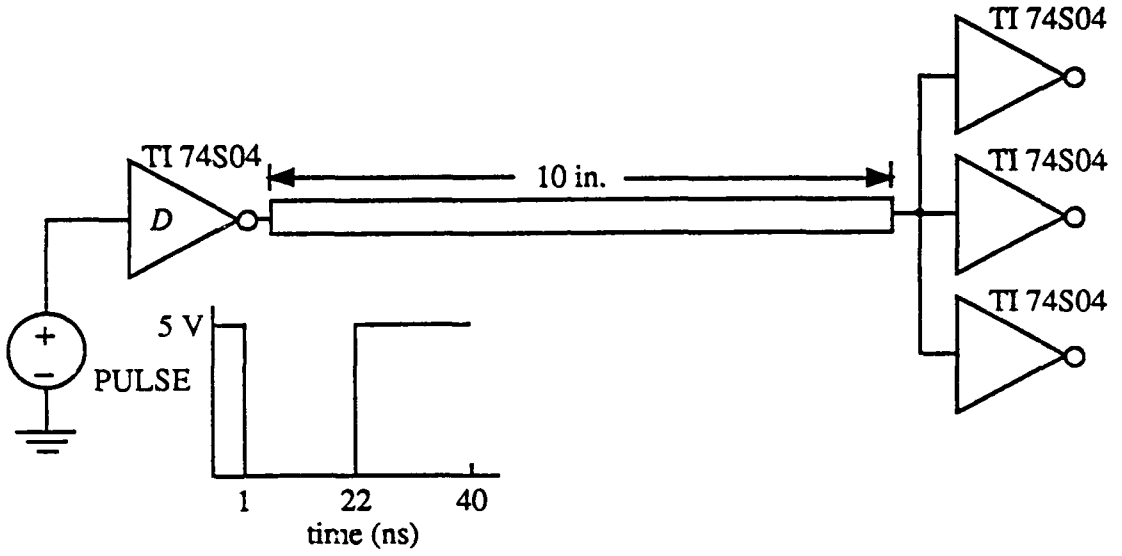

Figure 4.1 Single lossy transmission line interconnecting TI 74S04 inverters. The output of the driver D is made to switch from low to high at 1 ns and then from high to low at 22 ns. For the inverters: rise time = 2.2 ns, fall time = 2.2 ns, C_{in} = 5.4 pF, C_{out} = 5.0 pF. For the transmission line: $R = \max\{6.8, 0.26\sqrt{f}/10^3\}$ Ω/in. = $\max\{267.7, 10.24\sqrt{f}/10^3\}$ Ω/m, L = 307.1 nH/m, G = 0.0 S/m, and C = 85.3 pF/m. When losses are neglected the characteristic impedance is 60 Ω.

These parameters are those of a high-density interconnect used to transmit data in fast computers [45].

For computational efficiency, a simplified model [46] was used to represent the digital devices. When the inverter is used as a load, its input is modeled as a parallel combination of a constant capacitance and a voltage-dependent nonlinear resistor as shown in Fig. 4.2(a). When the inverter is used as a driver, its output is modeled in a manner similar to that of its input, except that now the nonlinear resistor is time varying. This model is shown in Fig. 4.2(b). As an example, the *v-i* curves of the nonlinear resistors used for the TI 74S04 inverter are shown in Fig. 4.3. The input curve is shown in Fig. 4.3(a), and the output curves are shown in Fig. 4.3(b). The input curve, output-low curve, and output-high curve are generated from static measurements [47]. The transition curves between the two output curves are generated by the program.

When the driver is initially triggered by the pulse (see Fig. 4.1), the device is operating on the output-low curve of Fig. 4.3(b). During a period corresponding to the rise time of the inverter, the model passes through the transition curves to the output-high curve where it remains as long as the input to the driver is held low. When the input to the inverter is switched back to high, the output switches back to the low state via the same transition curves during the fall time specified for the device. A number of researchers have had good experimental agreement using a model of this type [40],[46].

The computer simulation of the circuit of Fig. 4.1 was first conducted using the methods developed in Chapter 3 to model the transmission line and then using the lumped delay elements of Fig. 4.4 to model the line. Ten lumped delay elements were used to approximate the line; the low-frequency resistance was used since frequency dependence cannot be modeled by the delay elements. A comparison of the resulting waveforms is shown in Fig. 4.5. In Fig. 4.5(a) the two simulations are compared at the drive end, and in Fig. 4.5(b) they are compared at the load end. Except for a small difference in the steady-state values for the output-high state of the driver, the results are nearly identical.

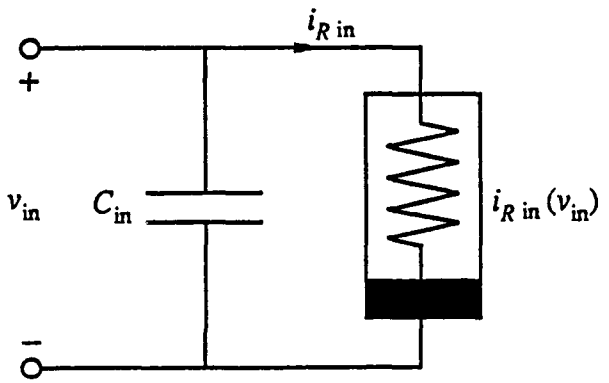

(a)

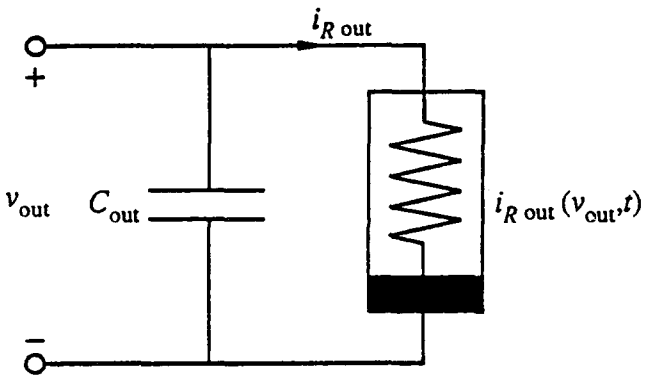

(b)

Figure 4.2 Inverter circuit model: (a) for the input when used as a load, (b) for the output when used as a driver.

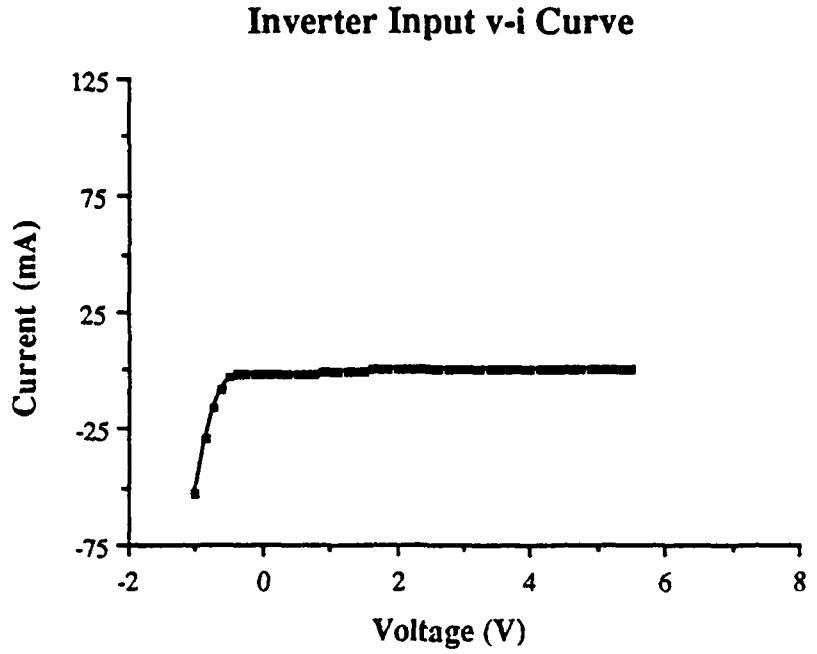

(a)

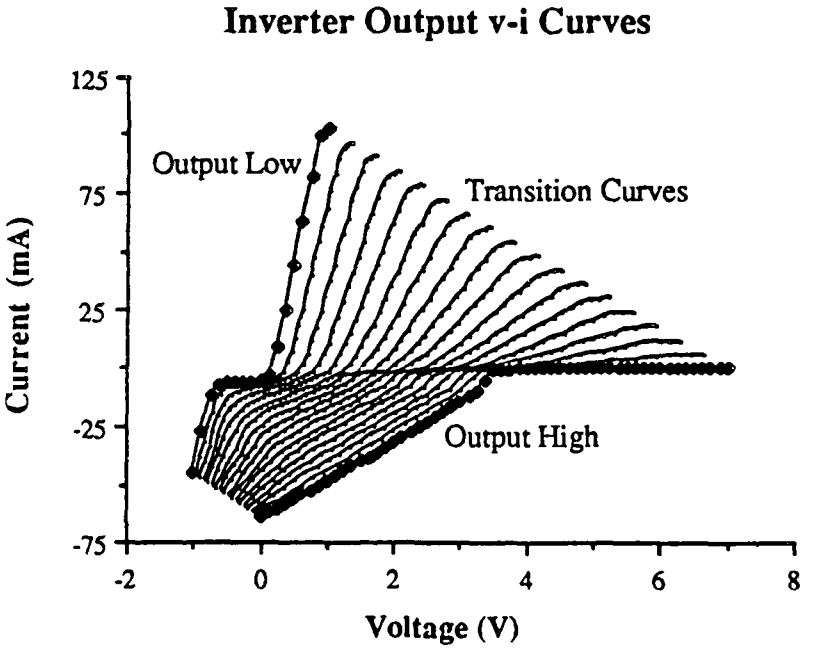

(b)

Figure 4.3 TI 74S04 inverter *v-i* curves.

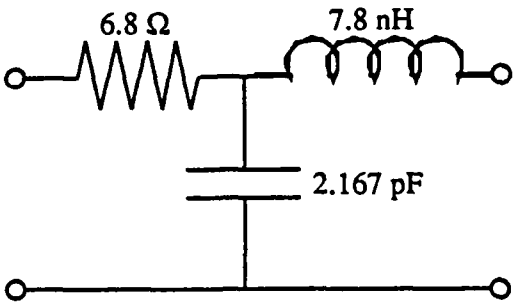

Figure 4.4 Lumped delay element: one of ten cascaded to model the lossy transmission line of Fig. 4.1.

An *RC* effect in the rise and fall times that results from the conductor losses can be seen in the figures. This is a major problem facing users of fast digital chips.

The next example consists of the lossless lines terminated by linear resistors and capacitors as depicted in Fig. 4.6(a). The inductance and capacitance matrices and resulting characteristic impedance matrix for the coupled lossless lines are shown in Fig. 4.6(b). Even though the primary goal of this thesis has been to compute the transient responses of lossy transmission lines with nonlinear terminations, this example can serve as a test for the program since the results will be compared to a Laplace transform solution and an experimental solution [32]. The solution obtained when the method of Chapter 3 is employed is shown in Fig. 4.7(a); the solution by the method of Laplace transforms is shown in Fig. 4.7(b); and the experimental results are shown in Fig. 4.7(c). The two numerical solutions are nearly identical as one would expect. The experimental solutions agree within sufficient accuracy.

The literature is sparse concerning experiments that consist of pulse responses to lossy multiconductor transmission lines. However, the article by Gruodis and Chang [30] contains such an experiment, and the next example compares simulated results using the methods developed in this investigation to their experimental results. The circuit used for

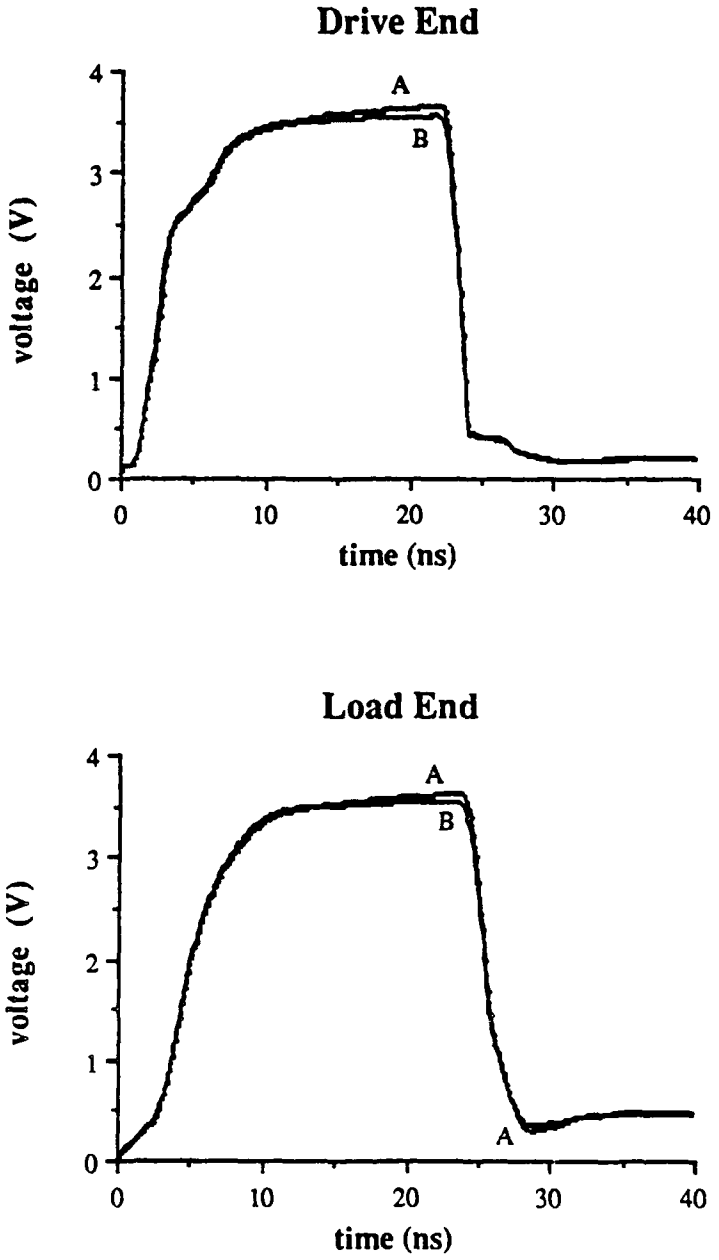

Figure 4.5 Comparison between simulated waveforms for the circuit of Fig. 4.1 when the transmission line is modeled by the method of Chapter 3 with a frequency-dependent resistance (curves A) and when it is modeled by lumped delay elements of the type in Fig. 4.4 (curves B).

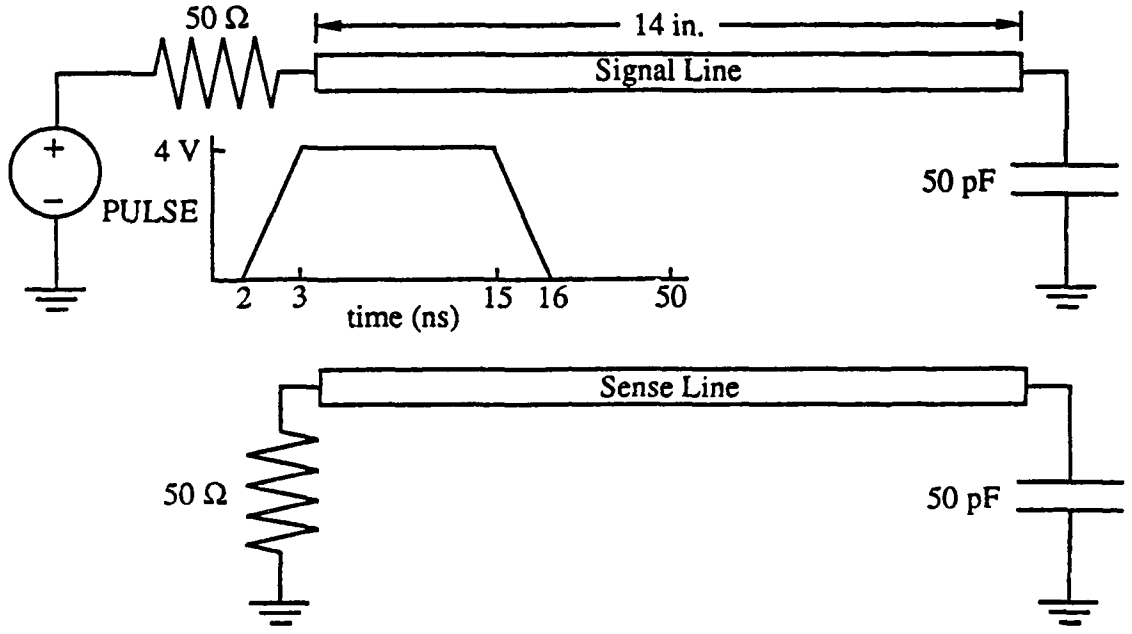

(a)

$$L = \begin{bmatrix} 455 & 147 \\ 147 & 455 \end{bmatrix} \text{ nH/m} \qquad C = \begin{bmatrix} 99 & -22 \\ -22 & 99 \end{bmatrix} \text{ pF/m} \qquad Z_0 = \begin{bmatrix} 69.4 & 19.0 \\ 19.0 & 69.4 \end{bmatrix} \Omega$$

(b)

Figure 4.6 Coupled lossless transmission line with linear terminations for numerical simulations and experimental measurement: (a) circuit configuration, (b) inductance and capacitance matrices and resulting characteristic impedance matrix.

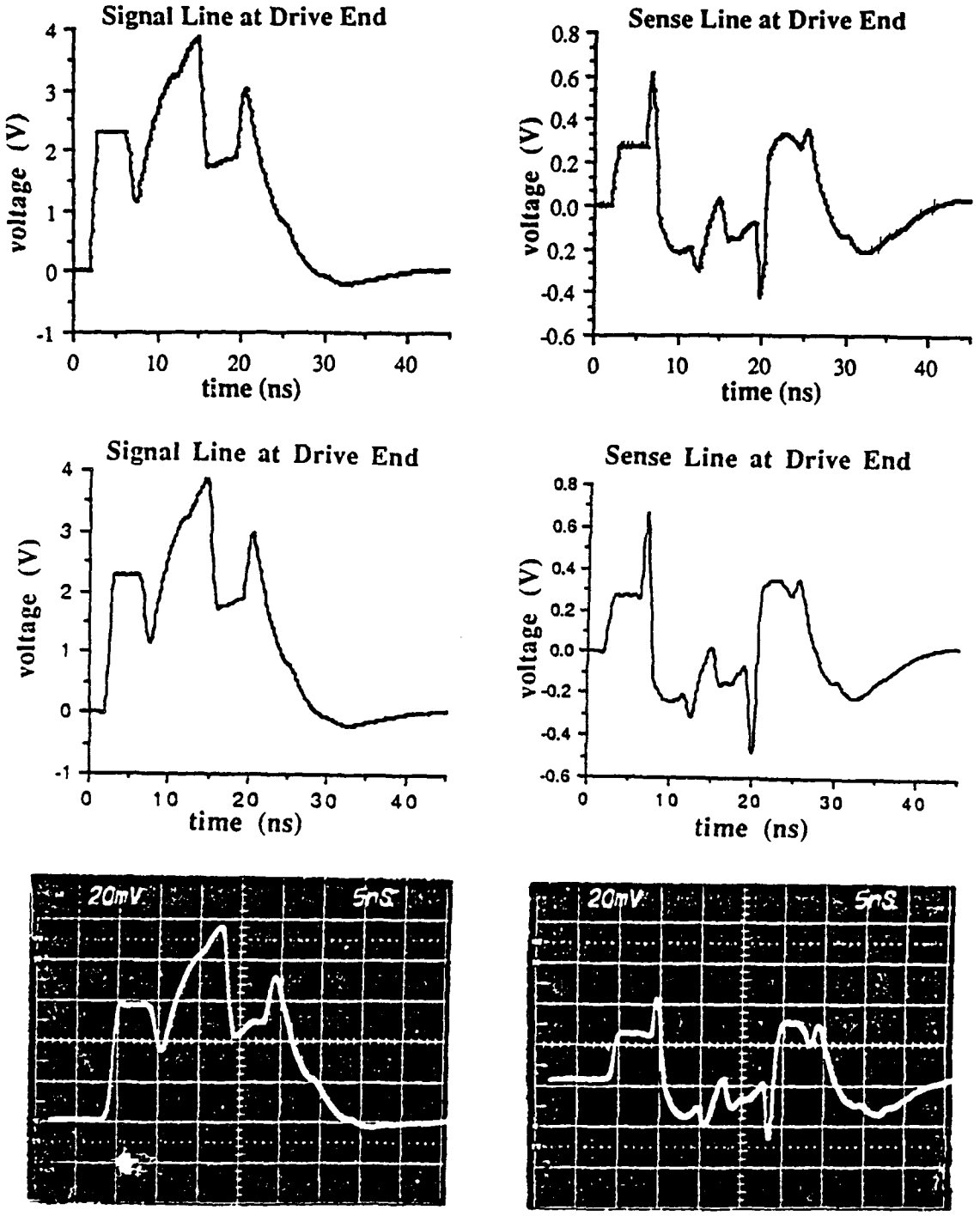

Figure 4.7 Comparison among two types of simulated waveforms and experimental waveforms for the circuit of Fig. 4.6: top, waveforms simulated by the method of Chapter 3; middle, waveforms simulated by the Laplace transform method; bottom, experimental waveforms. For the experimental waveforms, the attenuation is a factor of 40 for the signal line and 10 for the sense line.

the experimental setup is shown in Fig. 4.8. Gruodis and Chang confined their experiment to low frequencies (around 1 MHz) in order to minimize the effects of discontinuities inherent in connecting the line to the signal generator and terminating resistors. The transmission line made use of a commercial telecommunication cable consisting of four #22-AWG conductors. One wire of one of the two twisted pairs of which the cable consisted was used as the signal line. The other wire of the same twisted pair was used as the sense line. The second twisted pair along with the aluminum-coated mylar wrapping and braided shield formed the ground return. The measured parameters of the transmission line are shown in Table 4.1. The experimental results are given in Fig. 4.9(a) and the simulated results are given in Fig. 4.9(b). As can easily be seen, all waveforms are very nearly identical except for the load end of the signal line in which the simulated results do not experience the slight rise-time degradation that occurs in the experimental case. However, the results are well within acceptable limits of accuracy.

Note that for this simple example of two symmetrical lines, the eigenvector matrix **E** turns out to be independent of frequency:

$$\mathbf{E} = \frac{1}{\sqrt{2}}\begin{bmatrix} 1 & 1 \\ 1 & -1 \end{bmatrix}$$

consisting of only the common and differential modes. The method described herein is not limited to this case, and a more general case is considered in the final example.

Of important concern in the transmission of high-speed pulse signals is the effect of discontinuities in the multiconductor lines used to interconnect digital circuits. In Fig. 4.10 a set of FAIR 74F04 (Advanced Schottky TTL) inverters is shown interconnected by two (4+1)-conductor transmission lines joined by a connector. Figure 4.11 shows the microstrip used for the multiconductor transmission lines along with its inductance **L** and capacitance **C** matrices. The **L** and **C** matrices were calculated by the method of Chan and Mittra [41]. The microstrip dielectric had a relative permittivity ε_r of 4.5. The relative width of

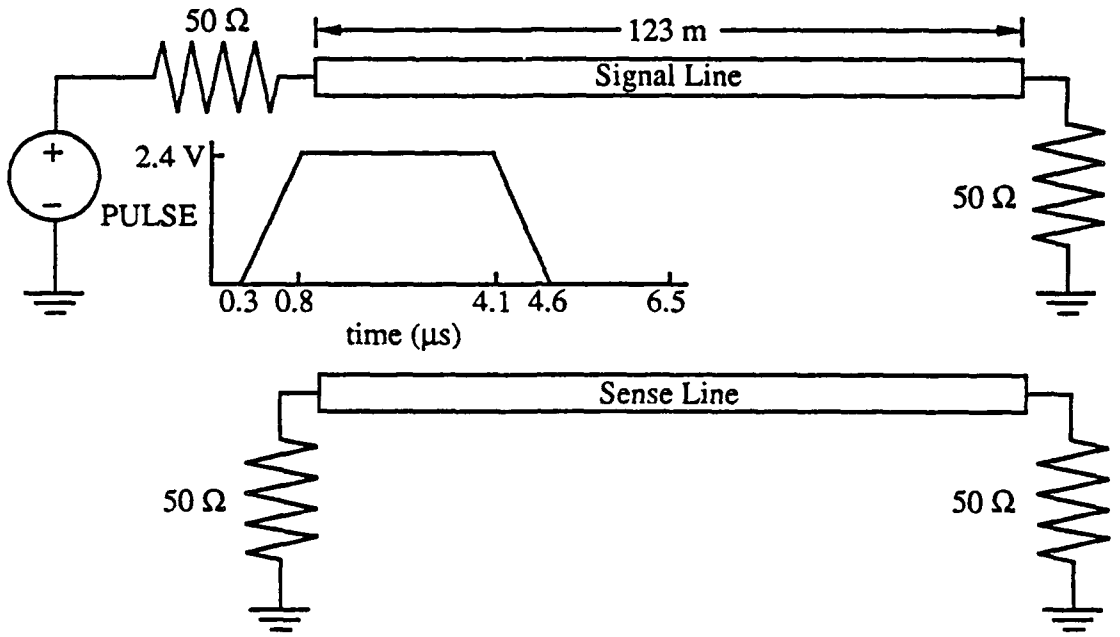

Figure 4.8 Coupled lossy transmission line with linear terminations. A telecommunication cable consisting of four #22-AWG conductors in two twisted pairs is used for the transmission line. The signal line consists of one wire of one of the twisted pairs, and the sense line consists of the other wire of the same twisted pair. The second twisted pair along with the aluminum-coated mylar wrapping and braided shield form the ground return. The measured parameters of the transmission line are shown in Table 4.1.

Table 4.1 Coupled transmission line parameters [30].

	Resistance (Ω/km)		
Freq. (kHz)	R_{11}	R_{12}	R_{22}
0.0	64.06	12.83	64.06
2.0	64.01	12.19	64.01
5.0	63.93	12.26	63.93
10.0	64.90	12.45	64.90
20.0	68.29	13.25	68.29
50.0	77.93	17.36	77.93
100.0	101.47	23.59	101.47
200.0	125.72	26.09	125.72
	Inductance (μH/km)		
Freq. (kHz)	L_{11}	L_{12}	L_{22}
0.0	510.5	99.5	510.5
2.0	510.5	99.5	510.5
5.0	498.0	98.3	498.0
10.0	492.0	96.4	492.0
20.0	477.7	94.3	477.7
50.0	451.1	81.8	451.1
100.0	435.4	81.8	435.4
200.0	402.2	68.8	402.2
500.0	360.1	58.8	360.1
1000.0	340.9	58.0	340.9
	Conductance (S/km)		
Freq. (kHz)	G_{11}	G_{12}	G_{22}
all	0.0	0.0	0.0
	Capacitance (nF/km)		
Freq. (kHz)	C_{11}	C_{12}	C_{22}
0.0	86.2	-14.0	86.2
2.0	74.0	-12.1	74.0
5.0	74.5	-12.7	74.5
10.0	75.0	-14.1	75.0
20.0	75.2	-15.9	75.2
50.0	75.6	-14.0	75.6
100.0	75.4	-15.3	75.4
200.0	76.8	-14.7	76.8
500.0	76.8	-14.2	76.8
1000.0	76.6	-14.6	76.6

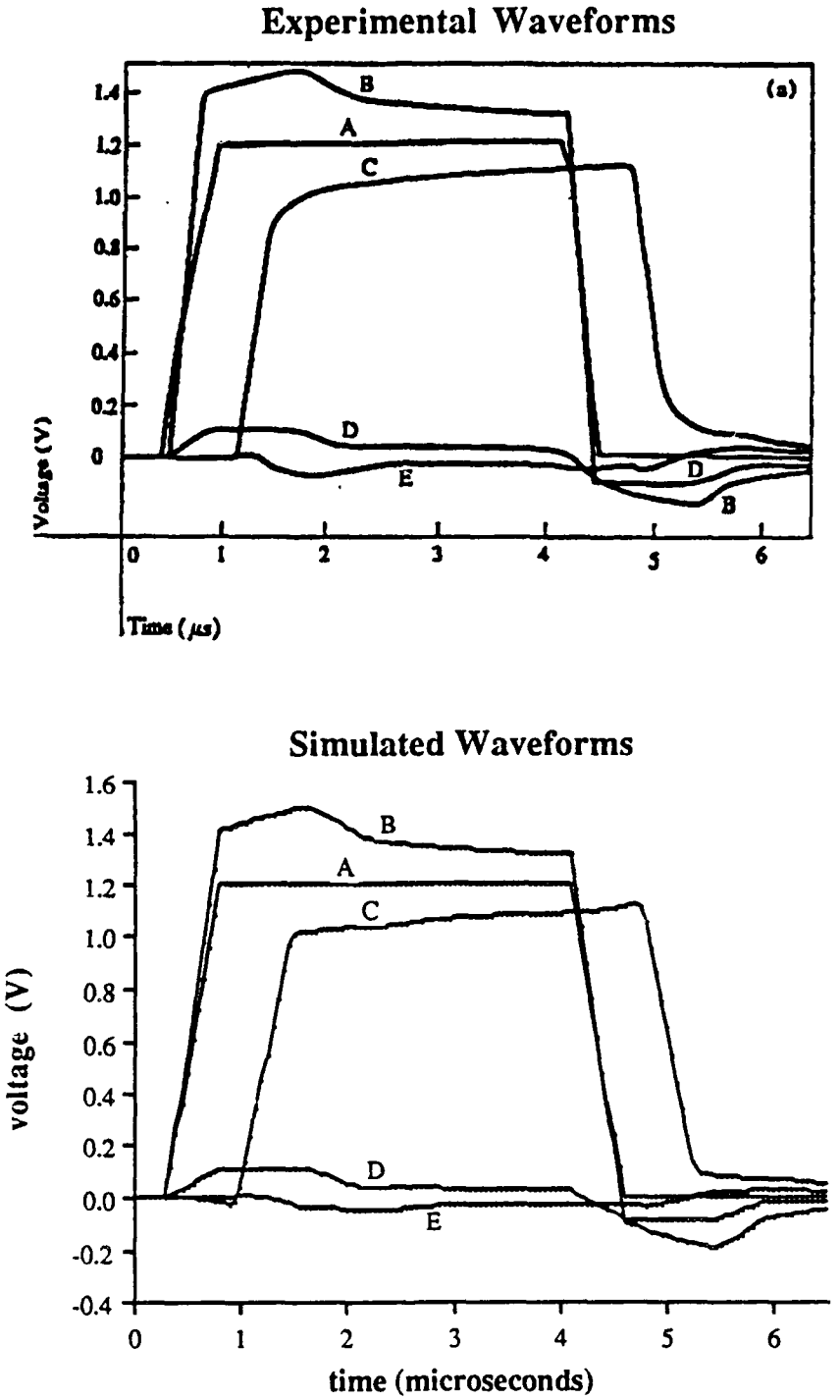

Figure 4.9 Experimental [30] and simulated waveforms for the circuit of Fig. 4.8. Curve A, one-half of drive signal; curve B, drive end of signal line; curve C, load end of signal line; curve D, drive end of sense line; curve E, load end of sense line.

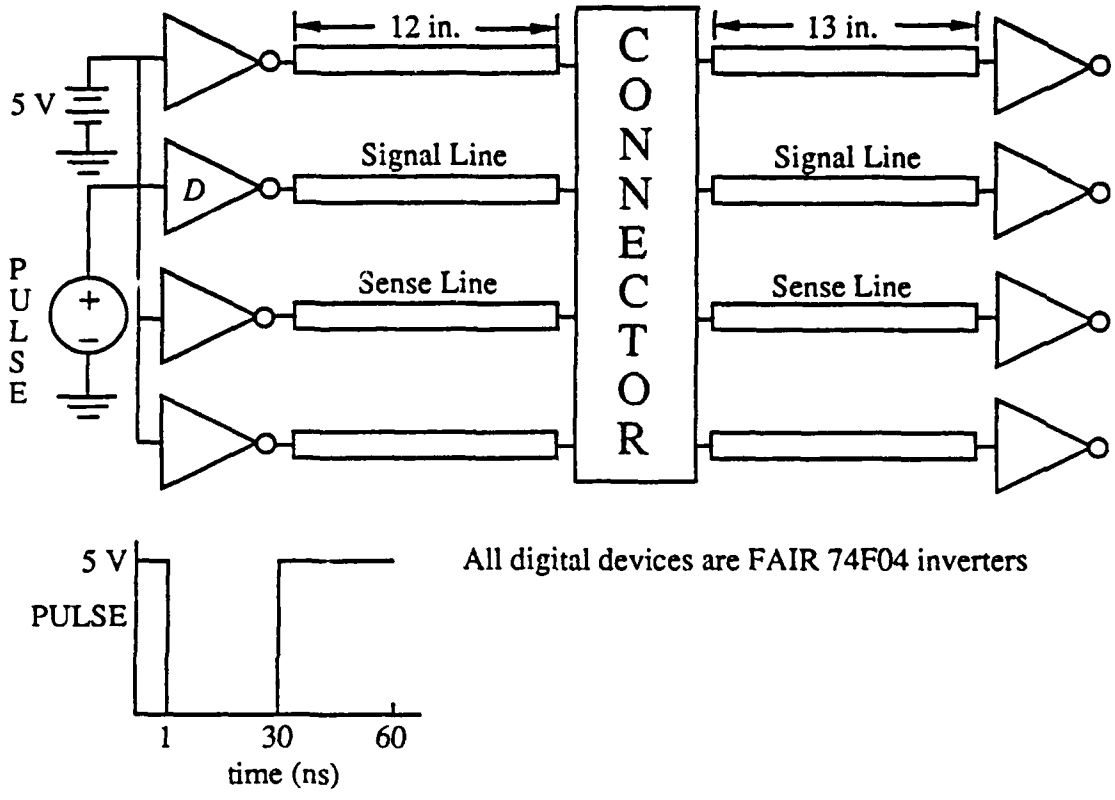

Figure 4.10 Multiconductor transmission lines joined by a connector and terminated by FAIR 74F04 inverters. The output of the driver D is made to switch from low to high at 1 ns and then from high to low at 30 ns. For the inverters: rise time = 2.75 ns, fall time = 1.25 ns, C_{in} = 4.6 pF, C_{out} = 5.0 pF. The geometry of the multiconductor lines is depicted in Fig. 4.11 along with their **L** and **C** matrices. When the lines are lossy, **R** = 50 x **1** Ω/m, where **1** is the identity matrix, and **G** = **0** S/m. The $\mathbf{L}_c$ and $\mathbf{C}_c$ matrices for the connector are given in Fig. 4.12.

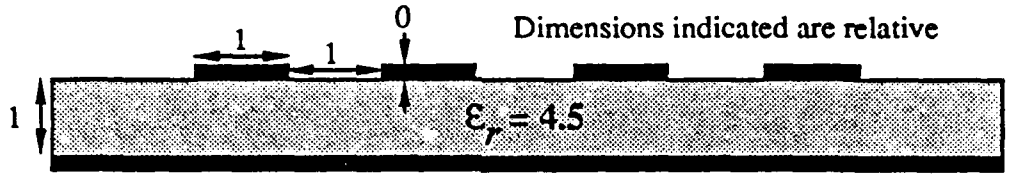

(a)

$$\mathbf{L} = \begin{bmatrix} 422.1 & 75.8 & 25.3 & 11.9 \\ 75.8 & 420.1 & 75.4 & 25.3 \\ 25.3 & 75.4 & 420.1 & 75.8 \\ 11.8 & 25.3 & 75.8 & 422.1 \end{bmatrix} \text{nH/m} \qquad \mathbf{C} = \begin{bmatrix} 85.85 & -8.55 & -0.64 & -0.28 \\ -8.55 & 86.96 & -8.48 & -0.64 \\ -0.64 & -8.48 & 86.96 & -8.55 \\ -0.28 & -0.64 & -8.55 & 85.85 \end{bmatrix} \text{pF/m}$$

(b)

$$\mathbf{Z}_0 = \begin{bmatrix} 70.41 & 9.84 & 2.67 & 1.14 \\ 9.84 & 70.08 & 9.77 & 2.67 \\ 2.67 & 9.77 & 70.08 & 9.84 \\ 1.14 & 2.67 & 9.84 & 70.41 \end{bmatrix} \Omega$$

(c)

Figure 4.11 Microstrip used for the multiconductor transmission lines in the circuit of Fig. 4.10: (a) cross section, (b) inductance and capacitance matrices, (c) characteristic impedance matrix when the microstrip is lossless.

$$L_c = \begin{bmatrix} 27.3 & 16.4 & 15.0 & 16.2 \\ 16.4 & 27.1 & 16.1 & 12.0 \\ 15.0 & 16.1 & 27.3 & 15.9 \\ 16.2 & 12.0 & 15.9 & 27.9 \end{bmatrix} \text{nH} \qquad C_c = \begin{bmatrix} 1582 & -736 & -154 & -520 \\ -736 & 1536 & -727 & -160 \\ -154 & -727 & 1516 & -349 \\ -520 & -160 & -349 & 1589 \end{bmatrix} \text{fF}$$

Figure 4.12 Inductance and capacitance matrices for the connector in the circuit of Fig. 4.10.

the conductors, spacing between the conductors, and the depth of the dielectric were taken to be one. When the lines were lossy, a diagonal resistance matrix with non-zero values of 50 Ω/m was chosen. The conductance of the dielectric was neglected. This is a reasonable assumption for the frequency range (up to a few gigahertz) of digital signal transmission. The connector was modeled by a π-equivalent circuit with inductance L_c and capacitance C_c matrices as shown in Fig. 4.12. (The capacitance matrix was split between the two halves of the π-equivalent circuit.)

Figure 4.13 shows a comparison between simulated waveforms for the signal line of the circuit of Fig. 4.10 when the transmission lines are lossless and when they are lossy; Fig. 4.14 shows the same for the sense line indicated in Fig. 4.10. In general, the losses caused significant attenuation and smoothing in both the signal and sense lines, but only a minor reduction of rise and fall times. Although not obvious from these plots, the effect of the connector is the small extra delay in the propagation time of the signal. This should not be surprising since the model for it is a lumped delay element, albeit one that includes coupled elements.

4.3 Conclusions

A number of simulation examples were presented to exercise the lossy multiconductor transmission line model in circuits that contain linear and nonlinear elements. The

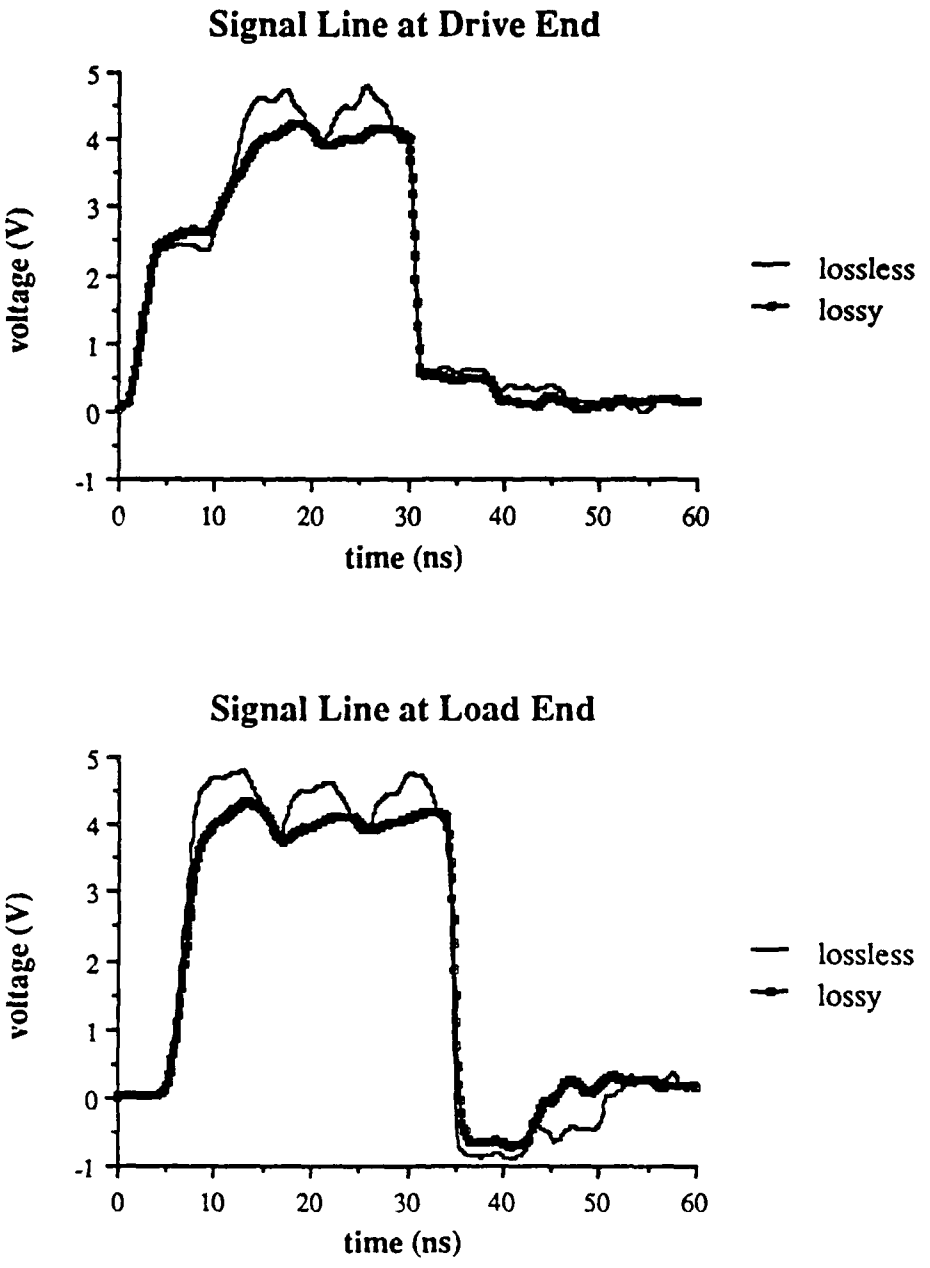

Figure 4.13 Comparison between simulated waveforms for the signal line of the circuit of Fig. 4.10 when the transmission lines are lossless and when they are lossy.

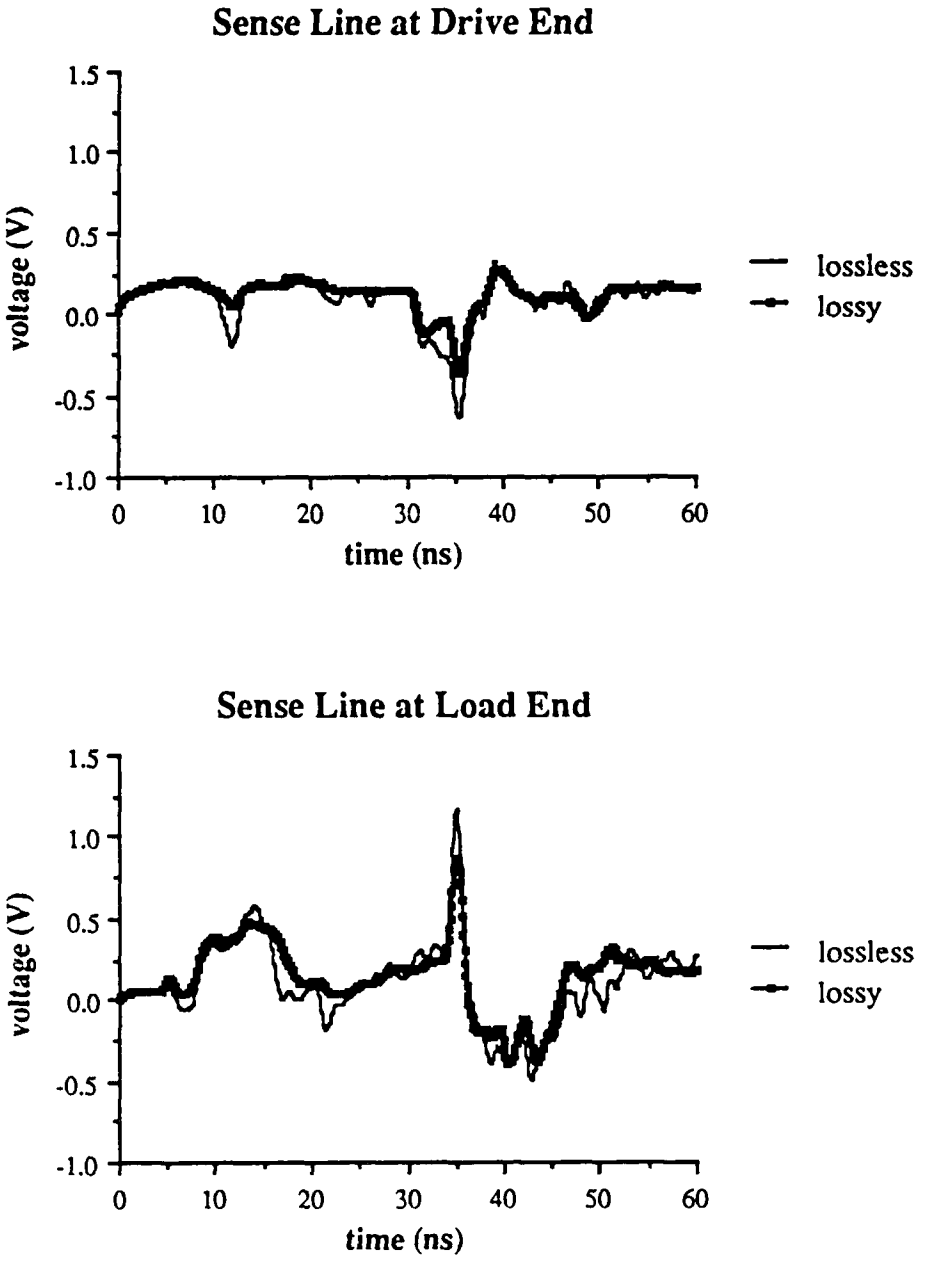

Figure 4.14 Comparison between simulated waveforms for the sense line of the circuit of Fig. 4.10 when the transmission lines are lossless and when they are lossy.

examples highlighted the interconnection of high-speed digital circuits by lossy multiconductor transmission lines with and without discontinuities. Simulation results showed good agreement with experimental results for both lossless and lossy multiconductor transmission lines.

CHAPTER 5

CONCLUSIONS

Using the frequency-dependent transmission line parameters, two time-domain models were developed for lossy multiconductor transmissions lines. It was shown that the endpoints of a lossy multiconductor line could be represented at each time step by discretized Thevenin or Norton equivalent circuits. Because these models contain only lumped elements, they can be easily implemented in a general circuit analysis program for simulating the transient responses of nonlinear circuits. A number of transient simulations were conducted in order to test the viability of the program. The program was found to give good results and to be of a very general nature.

Of particular interest was the interconnection of high-speed digital circuits by lossy multiconductor transmission lines containing discontinuities. The technique was demonstrated for the most general case of lossy multiconductor transmission lines with nonlinear terminations in which the modal transformation matrices were necessarily frequency dependent. This case has been avoided very adroitly in the literature. Results have only been shown for the simplest case of two symmetric conductors over a ground plane [30]-[32]. In this particular case, the modal transformation matrices result in an even and odd mode no matter what the frequency; therefore, the most general case is avoided. Also, the capability of incorporating discontinuities into the transmission line structure was presented for the first time.

A unique feature of the analysis procedure developed in this study was the exclusive use of infinite-line impulse responses in the formulation of the time-domain models. Because infinite lines are matched, there were no reflections in the impulse responses. The result is that these impulse responses are necessarily shorter than those for the quasi-matched case, such as the modified short-circuit parameters of Djordjevic et al. [31] and the

scattering parameters of Schutt-Aine [32]. Shorter impulse responses reduce the problem of aliasing encountered when taking the inverse transform and decrease the amount of computation that needs to be performed in the time domain. Techniques were presented to facilitate the implementation of the fast Fourier transform which is utilized to convert frequency-domain transfer functions to time-domain impulse responses.

The most serious drawback of the proposed technique is that direct integration of the convolution integrals is carried out in the time domain. Since the number of multiplications that must be performed is of the order of N^2, where N is the number of steps in the simulation, this is indeed a very serious consideration. However, newer computers that use vectorized arithmetic units have the capability of performing multiplications in parallel. The convolution as developed in this investigation is essentially a dot product which is a vectorizable operation. Existing computers have the capability of speeding up this operation by a factor of fifty. In the near future, a speedup of a full two orders of magnitude can be expected.

There appears to be two possible solutions to the problem mentioned above. In the first of these, the impulse responses are approximated by sums of exponentials; then, the convolutions can be accomplished recursively. In the second, the transfer functions are approximated by rational polynomials directly in the frequency domain so that state-variable techniques may be used. In both of these methods, the amount of computation needed to calculate the convolutions is greatly reduced and the need to store past-history values of voltage and current eliminated. The second procedure has been attempted by Gruodis and Chang [30] in a method similar to the one presented herein. They use the diagonal form of the exponential propagation matrix. The delays are extracted from the exponential functions, and modal signals are propagated along the transmission line by shifting them at each time step as is standard for lossless-line simulations. The waves are then shaped at the opposite end of the line by the remaining portions of the propagation functions. However, in converting between modal variables and line variables, they neglect the fact that the

transformation matrices are frequency-dependent. A physical interpretation of these transformation functions is not possible; consequently, their approximation is necessarily more difficult since they may be noncausal.

The inclusion of the lossy multiconductor transmission line models into an existing circuit simulator such as SPICE is the most obvious future need. Current computer-aided design tools for nonlinear circuits have the ability to model single lossless lines or use *RC* ladders to model single resistive lines. They cannot accurately portray the multiline coupling and frequency-dependent losses that arise when high-speed signals propagate between digital circuits. The method presented in this study is currently limited to uniform transmission lines. Tapered lines are also used by the computer and telecommunication industries; as a result, the inclusion of nonuniform lines is also of importance. In addition, the inclusion of nonlinear lines may be needed eventually, but a totally new procedure would have to be devised since the Fourier transform could no longer be used. This will probably not be necessary for digital circuit interconnections in the near future.

REFERENCES

[1] J. R. Carson and R. S. Hoyt, "Propagation of periodic currents over a system of parallel wires," *Bell Syst. Tech. J.*, vol. 6, pp. 495-545, July 1927.

[2] L. V. Bewley, *Traveling Waves on Transmission Systems*. New York: John Wiley and Sons, 1933.

[3] L. A. Pipes, "Matrix theory of multiconductor transmission lines," *Phil. Mag.*, ser. 7, vol. 24, pp. 97-113, July 1937.

[4] S. O. Rice, "Steady state solutions of transmission line equations," *Bell Syst. Tech. J.*, vol. 20, pp. 131-178, April 1941.

[5] L. M. Wedepohl, "Application of matrix methods to the solution of travelling-wave phenomena in polyphase systems," *Proc. Inst. Electr. Eng.*, vol. 110, pp. 2200-2212, December 1963.

[6] J. R. Carson, "Wave propagation over parallel wires: the proximity effect," *Phil. Mag.*, ser. 6, vol. 41, pp. 607-633, April 1921.

[7] J. R. Carson, "Wave propagation in overhead wires with ground return," *Bell Syst. Tech. J.*, vol. 5, pp. 539-554, October 1926.

[8] J. P. Bickford and P. S. Doepel, "Calculation of switching transients with particular reference to line energisation," *Proc. Inst. Electr. Eng.*, vol. 114, pp. 465-477, April 1967.

[9] M. J. Battisson, S. J. Day, N. Mullineux, K. C. Parton, and J. R. Reed, "Calculation of switching phenomena in power systems," *Proc. Inst. Electr. Eng.*, vol. 114, pp. 478-486, April 1967.

[10] L. M. Wedepohl and S. E. T. Mohamed, "Multiconductor transmission lines—theory of natural modes and Fourier integral applied to transient analysis," *Proc. Inst. Electr. Eng.*, vol. 116, pp. 1553-1563, September 1969.

[11] D. B. Jarvis, "The effects of interconnections on high-speed logic circuits," *IEEE Trans. Electron. Comput.*, vol. EC-12, pp. 476-487, October 1963.

[12] A. Feller, H. R. Kaupp and J. J. Digiacomo, "Crosstalk and reflections in high-speed digital systems," *AFIPS Conf. Proc.*, vol. 27, part 1, 1965 Fall Joint Computer Conf., pp. 511-525, 1965.

[13] I. Catt, "Crosstalk (noise) in digital systems," *IEEE Trans. Electron. Comput.*, vol. EC-16, pp. 743-763, December 1967.

[14] J. A. DeFalco, "Reflection and crosstalk in logic circuit interconnections," *IEEE Spectrum*, vol. 7, pp. 44-50, July 1970.

[15] H. Amemiya, "Time-domain analysis of multiple parallel transmission lines," *RCA Rev.*, vol. 28, pp. 241-276, June 1967.

[16] H. W. Dommel, "Digital computer solution of electromagnetic transients in single- and multiphase networks," *IEEE Trans. Power Apparatus Syst.*, vol. PAS-88, pp. 388-399, April 1969.

[17] F.-Y. Chang, "Transient analysis of lossless coupled transmission lines in a nonhomogeneous dielectric medium," *IEEE Trans. Microwave Theory Tech.*, vol. MTT-18, pp. 616-626, September 1970.

[18] C. W. Ho, "Theory and computer-aided analysis of lossless transmission lines," *IBM J. Res. Dev.*, vol. 17, pp. 249-255, May 1973.

[19] K. D. Marx, "Propagation modes, equivalent circuits, and characteristic terminations for multiconductor transmission lines with inhomogeneous dielectrics," *IEEE Trans. Microwave Theory Tech.*, vol. MTT-21, pp. 450-457, July 1973.

[20] V. K. Tripathi and J. B Rettig, "A SPICE model for multiple coupled microstrips and other transmission lines," *IEEE Trans. Microwave Theory Tech.*, vol. MTT-33, pp. 1513-1518, December 1985.

[21] M. Silverberg and O. Wing, "Time domain computer solutions for networks containing lumped nonlinear elements," *IEEE Trans. Circuit Theory*, vol. CT-15, pp. 292-294, September 1968.

[22] A. Budner, "Introduction of frequency-dependent line parameters into an electromagnetic transients program," *IEEE Trans. Power Apparatus Syst.*, vol. PAS-89, pp. 88-97, January 1970.

[23] J. K. Snelson, "Propagation of travelling waves on transmission lines—frequency dependent parameters," *IEEE Trans. Power Apparatus Syst.*, vol. PAS-91, pp. 85-91, January/February 1972.

[24] W. S. Meyer and H. W. Dommel, "Numerical modelling of frequency-dependent transmission-line parameters in an electromagnetic transients program," *IEEE Trans. Power Apparatus Syst.*, vol. PAS-93, pp. 1401-1409, September/October 1974.

[25] A. Semlyen and A. Dabuleanu, "Fast and accurate switching transient calculations on transmission lines with ground return using recursive convolutions," *IEEE Trans. Power Apparatus Syst.*, vol. PAS-94, pp. 561-571, March/April 1975.

[26] A. Ametani, "A highly efficient method for calculating transmission line transients," *IEEE Trans. Power Apparatus Syst.*, vol. PAS-95, pp. 1545-1551, September/October 1976.

[27] A. Semlyen, "Contributions to the theory of calculation of electromagnetic transients on transmission lines with frequency dependent parameters," *IEEE Trans. Power Apparatus Syst.*, vol. PAS-100, pp. 848-856, February 1981.

[28] J. R. Marti, "Accurate modelling of frequency-dependent transmission lines in electromagnetic transient simulations," *IEEE Trans. Power Apparatus Syst.*, vol. PAS-101, pp. 147-155, January 1982.

[29] D. M. Triezenberg, "An efficient state variable transmission line model," *IEEE Trans. Power Apparatus Syst.*, vol. PAS-98, pp. 484-492, March/April 1979.

[30] A. J. Gruodis and C. S. Chang, "Coupled lossy transmission line characterization and simulation," *IBM J. Res. Dev.*, vol. 25, pp. 25-41, January 1981.

[31] A. R. Djordjevic, T. K. Sarkar, and R. F. Harrington, "Analysis of lossy transmission lines with arbitrary nonlinear terminal networks," *IEEE Trans. Microwave Theory Tech.*, vol. MTT-34, pp. 660-666, June 1986.

[32] J. E. Schutt-Aine, "Modeling and Simulation of High-Speed Digital Circuit Interconnections," Ph.D. dissertation, University of Illinois, Urbana, IL, 1988.

[33] C.-W. Ho, A. E. Ruehli, and P. A. Brennan, "The modified nodal approach to network analysis," *IEEE Trans. Circuits Syst.*, vol. CAS-22, pp. 504-509, June 1975.

[34] L. O. Chua and P.-M. Lin, *Computer-Aided Analysis of Electronic Circuits: Algorithms and Computational Techniques*. Englewood Cliffs, NJ: Prentice-Hall, 1975.

[35] S. A. Schelkunoff, "Conversion of Maxwell's equations into generalized telegraphist's equations," *Bell Syst. Tech. J.*, vol. 34, pp. 995-1043, September 1955.

[36] F.-Y. Chang, "Computer-aided characterization of coupled TEM transmission lines," *IEEE Trans. Circuits Syst.*, vol. CAS-27, pp. 1194-1205, December 1980.

[37] C. Wei, R. F. Harrington, J. R. Mautz, and T. K. Sarkar, "Multiconductor transmission lines in multilayered dielectric media," *IEEE Trans. Microwave Theory Tech.*, vol. 32, pp. 439-449, April 1984.

[38] R. F. Harrington and C. Wei, "Losses on multiconductor transmission lines in multilayered dielectric media," *IEEE Trans. Microwave Theory Tech.*, vol. MTT-32, pp. 705-710, July 1984.

[39] A. R. Djordjevic and T. K. Sarkar, "Frequency behaviour of multiconductor transmission line inductances and resistances," *Archiv für Elektronik und Übertragungstechnik* (*AEÜ*), Band 40, Heft 4, pp. 254-256, July/August 1986.

[40] S. P. Castillo, "Electromagnetic Modeling of High-Speed Digital Circuits," Ph.D. dissertation, University of Illinois, Urbana, IL, 1987.

[41] C. H. Chan and R. Mittra, "Analysis of MMIC structures using an efficient iterative approach," *IEEE Trans. Microwave Theory Tech.*, vol. 36, pp. 96-105, January 1988.

[42] S. Perlis, *Theory of Matrices*. Cambridge, MA: Addison-Wesley, 1952.

[43] T. S. Blazeck, Computer code MTLTDA, Electromagnetic Communication Laboratory, University of Illinois, Urbana, IL, 1989.

[44] J. R. Sutton, Computer code TDA, Electromagnetic Communication Laboratory, University of Illinois, Urbana, IL, 1987.

[45] Digital Equipment Corporation, Data for high-density interconnects, 1988.

[46] J. R. Sutton, "Computer-Aided Design of Nonlinear Networks with N-Conductor Transmission Line Systems," M.S. thesis, University of Illinois, Urbana, IL, 1987.

[47] GTE Corporation, Data for inverter *v-i* curves, 1984.

APPENDIX C

Scattering Parameter Transient Analysis of Transmission Lines Loaded with Nonlinear Terminations

JOSE E. SCHUTT-AINE, STUDENT MEMBER, IEEE, AND RAJ MITTRA, FELLOW, IEEE

Abstract—This work presents a new approach for the time-domain simulation of transients on a dispersive and lossy transmission line terminated with active devices. The method combines the scattering matrix of an arbitrary line and the nonlinear causal impedance functions at the loads to derive expressions for the signals at the near and far ends.

The problems of line losses, dispersion, and nonlinearities are first investigated. A time-domain formulation is then proposed using the scattering matrix representation. The algorithm assumes that dispersion and loss models for the transmission lines are available and that the frequency dependence is known. Large-signal equivalent circuits for the terminations are assumed to be given. Experimental and computer-simulated results are compared for the lossless dispersionless case, and the effects of losses and dispersion are predicted.

I. Introduction

IN TODAY'S MANY applications of integrated circuits and printed circuit boards, transmission lines and interconnections play an instrumental role at virtually every level of integration. With the design of fast devices having switching times in the picosecond range, transmitting data at high megabaud rates has become very commonplace in modern digital computers and switching networks used for telecommunication. Signal delays and rise times are more and more limited by interconnection lengths rather than by device speed and represent a potential obstacle to the ultimate scaling on VLSI technology. In recent years, modeling interconnections has become a major focus of interest in the implementation of digital and microwave circuits. Shorter rise and fall times as well as higher frequency signals have compelled most transmission lines to operate within ranges where dispersion is no longer negligible. Skin effect and losses contribute to signal corruption leading to waveform attenuation as well as pulse rise and fall time degradations. In wafer-scale integration, these losses can become very significant and may lead to an *RC* type behavior of the lines. Finally, in the case of multiconductor lines, cross-coupling between neighboring lines may increase the level of distortion in excited lines which can initiate false signals in nonexcited lines.

The implementation of a high-density-compatible packaging scheme is essential for the design of high-speed digital systems such as gallium arsenide integrated circuits. For microwave or digital applications, printed circuit boards, chip carriers, and modeling of these networks represent the first step toward implementing reliable design guidelines. A complete CAD tool for studying these effects would require a frequency-domain characterization of the transmission line with higher-order modes included to account for dispersion. Numerous authors have investigated the properties of microstrip lines at high frequencies and derived expressions relating the propagation characteristics to frequency [1]–[10]. Full-wave and simplified models have been proposed to describe these effects and to derive the frequency dependence of the characteristic impedance and the propagation constant. Other geometries, such as stripline, buried microstrip, and coplanar, have thus far received less attention but obey the same restrictions imposed on the electrical performance of microstrip at microwave frequencies.

Of equal importance is the analysis of a high-speed or high-frequency signal propagating on a dispersive and lossy transmission line. Such an analysis requires a complete and accurate frequency characterization of the structure of interest and, for practicality, must implement the nonlinear and time-changing behaviors of the terminations, which are transistors, logic gates, or other types of active devices. Several investigators have attempted to set up analytical models describing wave propagation in such systems. Solutions for lossless lines with arbitrary terminations were obtained by Mohammadian *et al.* [12] using a forward and backward wave approach. Veghte and Balanis [13] have analyzed the distortion of a pulse due to dispersion along a microstrip transmission line. Caniggia [14] combined macromodels for transmission lines and terminations, and Djordjevic *et al.* [11] used a Green's function approach to simulate the time-domain transient on a multiconductor array with nonlinear terminations.

In this study, a combined frequency-domain, time-domain approach is used to formulate the propagation equations on a dispersive and lossy line with nonlinear behavior at the terminations. The novelty of the method resides in the formulation, which separates the linear expressions for the transmission line from the nonlinear expressions for the terminations by means of scattering parameters and the use of an auxiliary reference imped-

Manuscript received August 1, 1987; revised October 4, 1987.

The authors are with the Electromagnetic Communication Laboratory, Department of Electrical and Computer Engineering, University of Illinois, Urbana, IL 61801.

IEEE Log Number 8718865.

0018-9480/88/0300-0529$01.00 ©1988 IEEE

ance. A time-domain flow-graph representation of the solution is also derived. In the lossless case, the solution reduces to very simple expressions which greatly increase computational efficiency.

II. Formulation

Consider an arbitrary transmission line with arbitrary loads at both ends (see Fig. 1). The differential equations relating the voltage V and the current I along the line are expressed by

$$-\frac{\partial V}{\partial x} = L_0 \frac{\partial I}{\partial t} + R_0 I \tag{1a}$$

$$-\frac{\partial I}{\partial x} = C_0 \frac{\partial V}{\partial t} + G_0 V \tag{1b}$$

where L_0, C_0, R_0, and G_0 are the inductance, capacitance, resistance, and conductance per unit length, respectively. The solutions for time-harmonic excitation are usually written in the frequency domain as ($\omega = 2\pi f$ is angular frequency)

$$V(\omega, x) = Ae^{-\gamma x} + Be^{+\gamma x} \tag{2a}$$

$$I(\omega, x) = \frac{1}{Z_0}[Ae^{-\gamma x} - Be^{+\gamma x}] \tag{2b}$$

where

$$\gamma = \sqrt{(R_0 + j\omega L_0)(G_0 + j\omega C_0)} \qquad Z_0 = \sqrt{\frac{R_0 + j\omega L_0}{G_0 + j\omega C_0}}. \tag{3}$$

Here γ and Z_0 are complex, leading to an attenuation of the signal as it propagates through the medium. If the terminations are linear and time-invariant (i.e., $Z_1(t)$ and $Z_2(t)$ are constant with time), the coefficients A and B can be determined by matching boundary conditions at $x = 0$ and $x = l$; next, an inverse Fourier transform approach can be used to solve for the time-domain solution. On the other hand, if the terminations are nonlinear or time-changing, then the boundary conditions must be formulated in the time domain as

$$V_s(t) = V(t,0) + Z_1(t) I(t,0) \tag{4}$$

$$Z_2(t) I(t,l) = V(t,l) \tag{5}$$

where $V_s(t)$ is the source voltage. $Z_1(t)$ and $Z_2(t)$ indicate the time variations of the source and load terminations, respectively. For any time greater than t, $Z_1(t)$ and $Z_2(t)$ are not known, since they depend on the voltage and current solutions at time t. In fact, the evaluation of $Z_1(t)$ and $Z_2(t)$ may involve several iterations that involve solving the terminal network equations with trial values until convergence to the true impedance values. Transforming conditions (4) and (5) into the frequency domain is inappropriate, and a time-domain formulation is thus necessary. Likewise, (2) and (3) cannot conveniently be analytically inverted into the time domain and constrained to satisfy (4) and (5). This limitation arises not only because of the dispersive and frequency-dependent characteristics

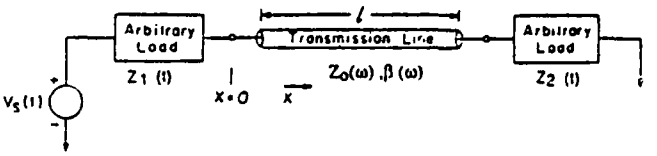

Fig. 1. Transmission line with nonlinear terminations and source generator.

of the line, but also because the evaluation of the coefficients A and B requires an *a priori* knowledge of the time-dependent load functions. A formulation in which the causality of the boundary conditions is implied thus becomes necessary. The use of scattering parameters allows one to define the properties of the transmission line independently from those of the terminations; consequently, by properly combining load and line relations, a simple expression for the solutions can be derived.

III. Scattering Parameter Formulation

Any linear two-port network can be described as a set of scattering parameters (S parameters) which relate incident and reflected voltage waves. These waves are variables which depend on the total voltages and currents at the two-port. If ideal (lossless and dispersionless) transmission lines of known characteristic (reference) impedance Z_{ref} are connected to both ports of a linear network, then the voltage waves on the reference lines (see Fig. 2) a_1, b_1, a_2, b_2 are defined as the incident and reflected waves from port 1 and port 2, respectively. The scattering parameters are then known to satisfy the frequency-domain relation

$$b_1 = \tilde{S}_{11} a_1 + \tilde{S}_{12} a_2 \tag{6}$$

$$b_2 = \tilde{S}_{21} a_1 + \tilde{S}_{22} a_2. \tag{7}$$

$\tilde{S}_{11}$ and $\tilde{S}_{22}$ are regarded as scattering reflection coefficients, whereas $\tilde{S}_{12}$ and $\tilde{S}_{21}$ are the scattering transmission coefficients of the network. The total voltages in ports 1 and 2 are, respectively, given by

$$V_1 = a_1 + b_1 \tag{8}$$

$$V_2 = a_2 + b_2 \tag{9}$$

and the expressions for the currents are

$$I_1 = \frac{a_1}{Z_{ref}} - \frac{b_1}{Z_{ref}} \tag{10}$$

$$I_2 = \frac{a_2}{Z_{ref}} - \frac{b_2}{Z_{ref}}. \tag{11}$$

A relation between the propagation characteristics of a transmission line and the associated scattering parameters can then be easily derived. For a single mode of propagation, it can be shown that for a given transmission line

$$\tilde{S}_{11} = \tilde{S}_{22} = \frac{(1-\alpha^2)\rho}{1-\rho^2\alpha^2} \qquad \tilde{S}_{12} = \tilde{S}_{21} = \frac{(1-\rho^2)\alpha}{1-\rho^2\alpha^2} \tag{12}$$

$$\alpha = e^{-\gamma l} \qquad \rho = \frac{Z_0(\omega) - Z_{ref}}{Z_0(\omega) + Z_{ref}} \tag{13}$$

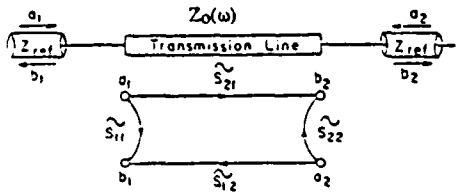

Fig. 2. Transmission line and frequency-domain flow-graph representation using scattering parameters.

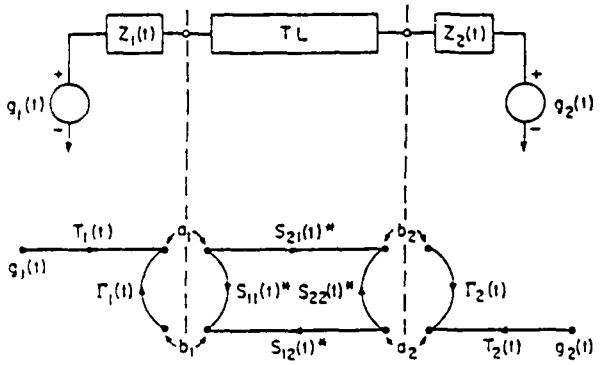

Fig. 3. Time-domain circuit and flow-graph representation of arbitrary transmission line (TL) with nonlinear terminations at time t. The sign * indicates a convolution between time-domain scattering parameters and the independent voltage waves a_1 and a_2 as per (14) and (15).

where $\alpha(\omega)$ and $Z_0(\omega)$ account for the dispersive and lossy behaviors of the line. $Z_0(\omega)$ is the characteristic impedance of the line to be analyzed and must be distinguished from Z_{ref}, the characteristic impedance of the reference lines which support the voltage waves associated with the S parameters. The scattering parameters of a transmission line depend only on its electrical characteristics and are not influenced by the source and load voltages at the terminations; however, the overall response of the system is a combination of line and termination responses and can be obtained by cascading the various sections of the network. We can then write the time-domain equations relating the voltage waves of an arbitrary line terminated with nonlinear loads (Fig. 3). We get (subscripts 1 and 2 refer to near end and far end, respectively)

$$b_1(t) = S_{11}(t)^* a_1(t) + S_{12}(t)^* a_2(t) \tag{14}$$

$$b_2(t) = S_{21}(t)^* a_1(t) + S_{22}(t)^* a_2(t) \tag{15}$$

where * indicates a convolution in the time domain. The scattering parameters $S_{11}(t), S_{12}(t), S_{21}(t), S_{22}(t)$ are the inverse transforms of the frequency-domain S parameters and can be viewed as Green's functions associated with the time-domain response of the transmission line, due to a single frequency source at the terminations. The load conditions at the near and far ends are now directly expressed in the time domain by looking at the flow-graph representation of the system (see Fig. 3)

$$a_1(t) = \Gamma_1(t) b_1(t) + T_1(t) g_1(t) \tag{16}$$

$$a_2(t) = \Gamma_2(t) b_2(t) + T_2(t) g_2(t) \tag{17}$$

in which $\Gamma_1(t), \Gamma_2(t), T_1(t), T_2(t)$ are the reflection and transmission coefficients associated with near and far ends, respectively:

$$T_i(t) = \frac{Z_{ref}}{Z_i(t) + Z_{ref}} \qquad \Gamma_i(t) = \frac{Z_i(t) - Z_{ref}}{Z_i(t) + Z_{ref}} \tag{18}$$

In (14) and (15), each of the convolution terms can be expressed as

$$S_{ij}^* a_j = \int_0^t S_{ij}(t-\tau) a_j(\tau)\, d\tau. \tag{19}$$

Since the algorithm to be derived must be amenable to computer usage, it is desirable to discretize (19) and isolate $a_j(t)$ in a manner analogous to [11, eqs. (12) and (13)]:

$$S_{ij}(t)^* a_j(t) = \sum_{\tau=1}^{t} S_{ij}(t-\tau) a_j(\tau)\, \Delta\tau$$

$$S_{ij}(t)^* a_j(t) = S_{ij}(0) a_j(t) \Delta\tau + \sum_{\tau=1}^{t-1} S_{ij}(t-\tau) a_j(\tau) \Delta\tau \tag{20}$$

or

$$S_{ij}(t)^* a_j(t) = S'_{ij}(0) a_j(t) + H_{ij}(t) \tag{21}$$

where $\Delta\tau$ is the time step and $S'_{ij}(0) = S_{ij}(0)\Delta\tau$. $H_{ij}(t) = \sum_{\tau=1}^{t-1} S_{ij}(t-\tau) a_j(\tau) \Delta\tau$ represents the history of the line and depends on information up to time $t-1$. Causality insures that the a_j's are known for $\tau < t$, which allows the use of this information for the determination of the a_j's at $\tau = t$. We first substitute (21) into (14) and (15) and obtain

$$b_1(t) = S'_{11}(0) a_1(t) + S'_{12}(0) a_2(t) + H_{11}(t) + H_{12}(t) \tag{22}$$

$$b_2(t) = S'_{21}(0) a_1(t) + S'_{22}(0) a_2(t) + H_{21}(t) + H_{22}(t). \tag{23}$$

Combining the above equations with those for the forward waves (16) and (17), one gets

$$a_1(t) = \frac{[1 - \Gamma_2(t) S'_{22}(0)][T_1(t) g_1(t) + \Gamma_1(t) M_1(t)]}{\Delta(t)} + \frac{\Gamma_1(t) S'_{12}(0)[T_2(t) g_2(t) + \Gamma_2(t) M_2(t)]}{\Delta(t)} \tag{24}$$

$$a_2(t) = \frac{[1 - \Gamma_1(t) S'_{11}(0)][T_2(t) g_2(t) + \Gamma_2(t) M_2(t)]}{\Delta(t)} + \frac{\Gamma_2(t) S'_{21}(0)[T_1(t) g_1(t) + \Gamma_1(t) M_1(t)]}{\Delta(t)} \tag{25}$$

$$\Delta(t) = [1 - \Gamma_1(t) S'_{11}(0)][1 - \Gamma_2 S'_{22}(0)] - \Gamma_1(t) S'_{12}(0) \Gamma_2(t) S'_{21}(0) \tag{26}$$

where $M_1(t) = H_{11}(t) + H_{12}(t)$, and $M_2(t) = H_{21}(t) + H_{22}(t)$. The variables $b_1(t)$ and $b_2(t)$ are recovered using (22) and (23), and the total voltages at ports 1 and 2, by using (8) and (9). Fig. 4 shows the flow-graph representation for the transmission line at time t in which the memory of the complete network has been included in the terms $M_1(t)$ and $M_2(t)$. The independent terms are $g_1(t)$

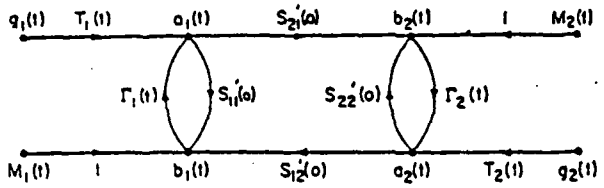

Fig. 4. Equivalent flow-graph representation of arbitrary transmission line with nonlinear time-varying terminations at time t. The history of the network is included via the memory variables $M_1(t)$ and $M_2(t)$. Note that this representation involves only multiplications in the time domain.

and $g_2(t)$. $M_1(t)$ and $M_2(t)$ are also independent and contain the information pertinent to the history of the line. Numerical efficiency is of practical importance for the simulation since it determines the speed of the computations involved. Expressions (24)–(26) can be further reduced by observing that for transmission lines with nonzero length, $S_{12}'(0)$ and $S_{21}'(0)$ must vanish, since a finite duration is required for an arbitrary signal to propagate through the line. The above relations then become

$$a_1(t) = \frac{[1-\Gamma_2(t)S_{22}'(0)][T_1(t)g_1(t)+\Gamma_1(t)M_1(t)]}{\Delta(t)} \tag{27a}$$

$$a_2(t) = \frac{[1-\Gamma_1(t)S_{11}'(0)][T_2(t)g_2(t)+\Gamma_2(t)M_2(t)]}{\Delta(t)} \tag{27b}$$

$$b_1(t) = S_{11}'(0)a_1(t) + M_1(t) \tag{27c}$$

$$b_2(t) = S_{22}'(0)a_2(t) + M_2(t) \tag{27d}$$

with

$$\Delta(t) = [1-\Gamma_1(t)S_{11}'(0)][1-\Gamma_2(t)S_{22}'(0)]. \tag{28}$$

Computational limitations in these expressions are essentially determined by $M_1(t)$ and $M_2(t)$, which contain the history of the network and involve the voltage wave solutions from previous time steps. In the case where losses and dispersion are neglected, the frequency-domain scattering parameters associated with the transmission line become

$$\tilde{S}_{11}(\omega) = \tilde{S}_{22}(\omega) = \frac{(1-e^{-2j\omega l/v})\rho}{1-\rho^2 e^{-2j\omega l/v}} \tag{29}$$

$$\tilde{S}_{12}(\omega) = \tilde{S}_{21}(\omega) = \frac{(1-\rho^2)e^{-j\omega l/v}}{1-\rho^2 e^{-2j\omega l/v}} \tag{30}$$

where

$$\rho = \frac{Z_0 - Z_{\text{ref}}}{Z_0 + Z_{\text{ref}}}. \tag{31}$$

Since Z_0, the characteristic impedance of the line, is constant with time, and since Z_{ref}, the reference impedance, is arbitrary, one can choose $Z_{\text{ref}} = Z_0$, which leads to $\rho = 0$ and

$$\tilde{S}_{11}(\omega) = \tilde{S}_{22}(\omega) = 0 \tag{32}$$

$$\tilde{S}_{12}(\omega) = S_{21}(\omega) = e^{-j\omega l/v}. \tag{33}$$

Therefore, the time-domain Green's functions associated with the scattering parameters are

$$S_{11}(t) = S_{22}(t) = 0 \tag{34}$$

$$S_{12}(t) = S_{21}(t) = \delta\left(t - \frac{l}{v}\right) \tag{35}$$

$$M_1(t) = a_2(t - l/v) \tag{36}$$

$$M_2(t) = a_1(t - l/v) \tag{37}$$

$$\Delta(t) = 1. \tag{38}$$

We then obtain simple expressions for the forward and backward waves:

$$a_1(t) = T_1(t)g_1(t) + \Gamma_1(t)a_2(t - l/v) \tag{39}$$

$$a_2(t) = T_2(t)g_2(t) + \Gamma_2(t)a_1(t - l/v) \tag{40}$$

$$b_1(t) = a_2(t - l/v) \tag{41}$$

$$b_2(t) = a_1(t - l/v). \tag{42}$$

The advantage of the above expressions lies in their computational efficiency, since only a search is involved in the evaluation of the history of the network, and no summations of previously calculated terms are needed.

IV. Models for Terminations and Devices

Thus far, this study concentrated on simulating the time-domain transient response for arbitrary transmission lines terminated with nonlinear devices. In this section, we examine the nature of the terminations and the manner in which they are to be represented in a form consistent with the relations derived. Several techniques are available that convert reactive elements and nonlinear devices to time-varying causal resistances as well as voltage or current sources. We briefly overview two of these techniques, namely, the trapezoidal algorithm and the Newton–Raphson (NR) algorithm. A more detailed development can be found in [15]. Since formulation and solution are in the time domain, every element must have an equivalent network in the time domain. The trapezoidal algorithm is a numerical integration algorithm, and its use in representing reactive elements in the time domain is illustrated below. Consider a capacitor C, with a current–voltage relation given by

$$I = C\frac{dV}{dt}. \tag{43}$$

If we discretize the time variable by choosing a time step h, then the voltage V_{n+1} at time $t_{n+1} = (n+1)h$ can be approximated in terms of variables at $t = nh$ as

$$V_{n+1} = V_n + \frac{h}{2}V_{n+1}' + \frac{h}{2}V_n' \tag{44}$$

where the superscript $'$ indicates a derivative with respect to time. Making use of (43), we get

$$I_{n+1} = \frac{2C}{h}V_{n+1} - \left(\frac{C}{h}V_n + i_n\right). \tag{45}$$

Equation (45) can then be represented by the equivalent

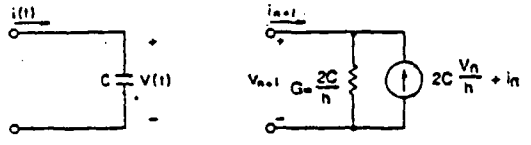

Fig. 5. Linear capacitor and equivalent time-domain trapezoidal algorithm representation.

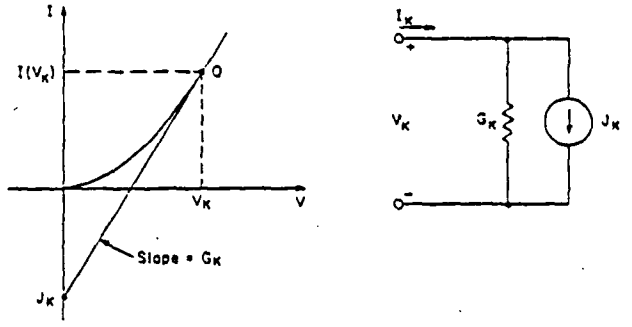

Fig. 6. Geometrical and circuit interpretation of the Newton–Raphson algorithm at the kth iteration.

linear one-port model at time $t_{n+1}=(n+1)h$ (see Fig. 5) with conductance $G=\frac{2C}{h}$ and current source $J_n=\frac{2C}{h}V_n+i_n$. An analogous derivation can be performed for inductances as well. The efficiency of the method depends on a proper choice of the time step which determines the stability of the numerical solution. Several other techniques of numerical integration are also available which offer greater stability at the price of numerical complexity [15].

Nonlinear elements such as diodes and transistors must be reduced to equivalent networks with linear elements at time t. If the nonlinear current voltage relation for these elements is known, then an iterative scheme such as the Newton–Raphson algorithm can be used to seek a solution. The circuit representation of the Newton–Raphson technique is illustrated in Fig. 6. At a particular time, a guess value for the voltage is chosen to which a current is associated via the $I-V$ relations that determine the operating point Q. The next guess is then related to the previous one by

$$V_{k+1}=V_k-\left[\frac{dI}{dV}\right]^{-1}I_k. \tag{46}$$

At each iteration step, the resulting equivalent circuit is composed of a linear conductance of value $G_k=dI/dV$ at V_k and a current source with value given by $J_k=I(V_k)-G_kV_k$. Solving the combined transmission line Newton–Raphson equivalent circuit problem at each iteration step will lead to the actual representation of the termination at time t.

Once linearization and discretization are performed, time-domain values are available for the equivalent resistances or generators. These expressions are causal, since their values at any time t depend on the history of the network which renders impossible an *a priori* knowledge of the time variations of the termination impedance. Nonlinear complex elements can be handled by first using the NR scheme for linearization at a given time, then stepping in the time domain while replacing linear complex elements by time-varying resistances and generators.

V. Applications and Practical Considerations

Many applications in microwave and digital communications require the use of transmission lines terminated with nonlinear devices. Distortion and noise arise when the terminations are not matched to the line impedance. Moreover, if losses and dispersion are present in the line, attenuation and time delay come into account. The combination of these effects needs to be modeled and simulated on a reliable computer-aided design (CAD) tool. Simulations of pulse propagation through lossy transmission lines terminated with active devices can be very useful in predicting signal distortion, attenuation, rise and fall time degradation which occur along the transmission path. The necessary information for such a tool are the line parameters over a wide frequency range and complete device characteristics. The line parameters can be found from a frequency-domain full-wave dispersion analysis which includes the effects of losses. Device data are usually obtained from the current–voltage characteristics provided by the manufacturers.

Several computer simulation programs were developed to simulate waveform distortion on various combinations of transmission lines and terminations. First, a lossless stripline structure terminated with advanced Schottky (AS) TTL inverters was studied (see Fig. 7). The length of the line was 50 in (1.27 m) with $Z_0=73\ \Omega$, $v=0.142$ m/ns. The line was excited by the output of an AS04 inverter (driver). The receiving end of the line was connected to the inputs of eight AS240 inverters. For computational efficiency, a simple dynamic nonlinear equivalent circuit was used to model the output of the driver. The network consisted of a voltage generator in series with a voltage-dependent resistor. An 8 pF capacitor was placed in parallel with the combination to model rise and fall time degradation and RC time delays (see Fig. 7(b)). The generator provided a pulse with a magnitude of 4.2 V. The voltage dependence of the resistance is shown in Fig. 7(b). The quick jump in resistance is used to model the cutoff point of one output transistor of the TTL inverter. The input of each AS240 inverter was modeled as a reverse-biased Schottky diode in parallel with an 8 pF capacitor (see Fig. 7(c)). The simulation process involved first choosing a time interval and then stepping in time and determining the voltage variables as per (39)–(42). The trapezoidal scheme was used to convert capacitors to linear sources and resistances. Likewise, the Newton–Raphson algorithm made it possible to convert the Schottky diodes into a linearized equivalent circuit. The time steps were found to have no significant effects on the accuracy of the solutions due to the good stability properties of the trapezoidal algorithm. Experimental results are compared with the simulations in Fig. 8(a) and (b). Minor discrepancies were attributed to pin and socket inductances, which were not accounted for in the model. Likewise, charge control ef-

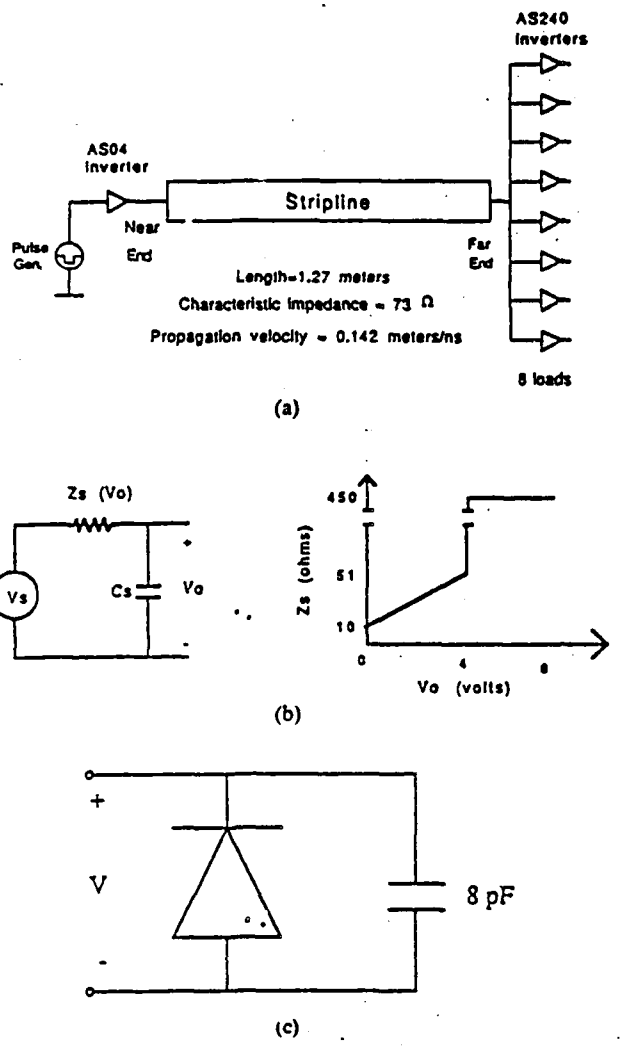

Fig. 7. (a) Configuration used for simulation of transients on a stripline structure with nonlinear loads. (b) Model used for AS04 driver with voltage dependence of impedance, $C_s = 8$ pF. $V_s(t)$ has the following characteristics: width = 108 ns, rise time = 5 ns, fall time = 4 ns. (c) Model used for the input of each AS240 receiver. The diode has a saturation current $I_s = 10^{-12}$ A.

fects, which determine rise and fall time degradation as well as time delay through the inverters, were not modeled. The otherwise overall good agreement indicated the validity of the simplified device models.

Losses were also analyzed using (27). First, the frequency-domain scattering parameters were calculated for the transmission line shown in Fig. 9. Skin effect in the conductor was accounted by a $\sqrt{f}$ behavior of the resistance per unit length. Once the frequency dependence of the scattering parameter was determined, a fast Fourier transform (FFT) algorithm was used to solve for the time-domain Green's functions associated with the S parameters. Then (20)–(28) were used to calculate the voltage waves. Fig. 9 shows the configuration used to predict and compare waveforms on lossless and lossy microstrip lines. The low-frequency characteristics of the line were: $L_0 = 539$ nH/m and $C_0 = 39$ pF/m. The resistance per unit length for the lossy case was $R_0 = \sqrt{f\ (\text{in GHz})}$ 1 kΩ/m. Dielectric losses were neglected

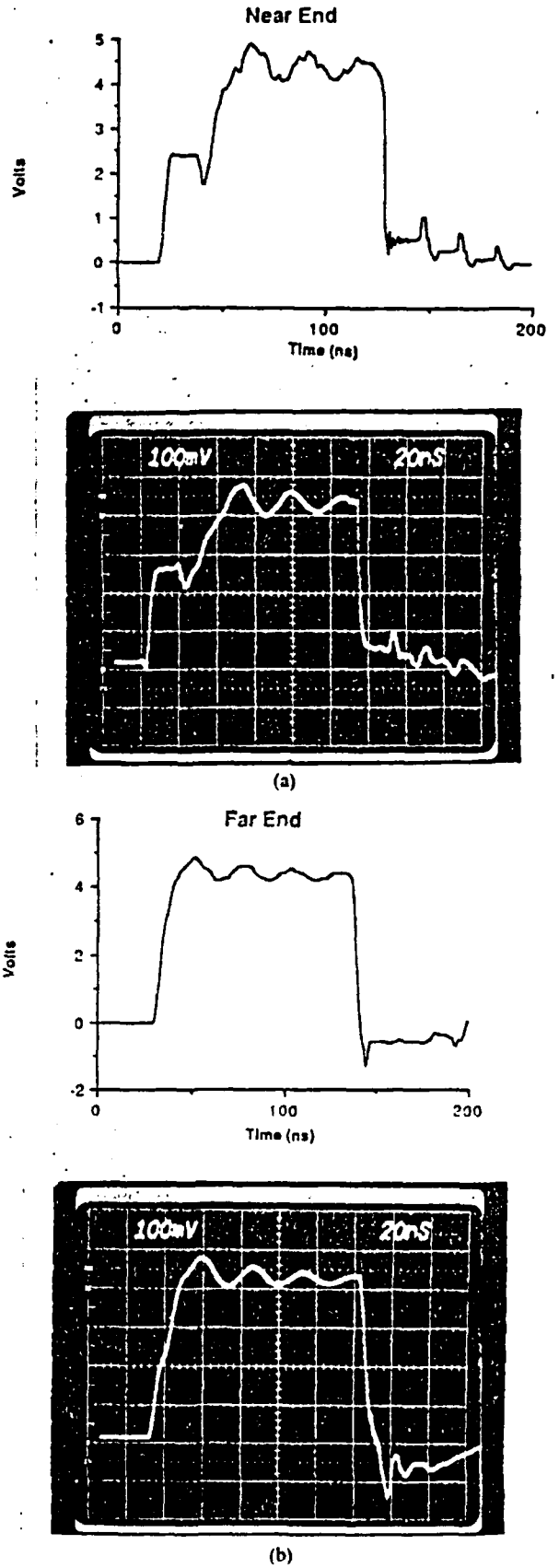

Fig. 8. Comparison of theoretical (plots) and experimental (photographs) simulations for the stripline structure terminated with AS inverters of Fig. 7 at (a) the near end and (b) the far end. Vertical scales in experimental simulations have a probe attenuation factor of 10.

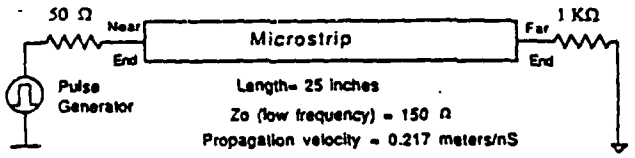

Fig. 9. Microstrip configuration used to simulate the effects of losses. Line length = 25 inches (0.635 meters). Low-frequency electrical characteristics: $L_0 = 539$ nH/m, $C_0 = 39$ pF/m. Loss characteristics: $R_0 = \sqrt{f \text{ in GHz}}$ 1 kΩ/m and $G_0 = 0$ mhos/meter. Pulse characteristics: magnitude = 4 V, width = 20 ns, rise and fall times = 1 ns.

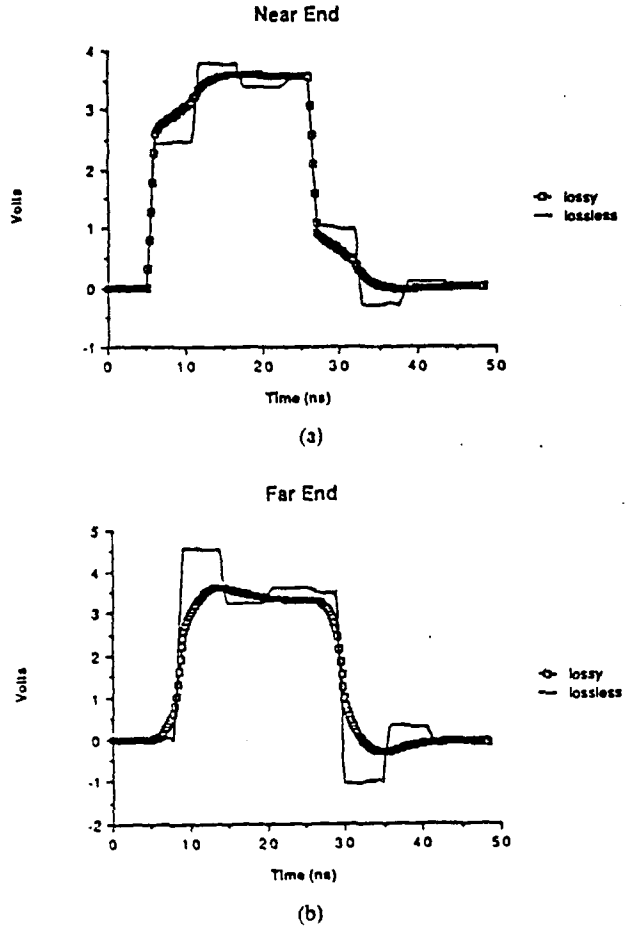

Fig. 10. Comparisons between responses for lossless and lossy cases for the microstrip structure of Fig. 9 at (a) the near end and (b) the far end.

($G_0 = 0$), which is a good representation of many interconnections in integrated circuit design. The above configuration was excited by a 4 V pulse generator with an internal impedance of 50 Ω, and a termination impedance of 1 kΩ. A comparison between lossy and lossless cases is shown in Fig. 10. As anticipated, the introduction of losses led to rise and fall time degradation and waveform attenuation. Experimental simulations were not available due to the lack of reliable measurement techniques for accurately determining the frequency dependence of microstrip loss parameters. Such information is essential in developing models to be used in conjunction with the simulations. Other alternatives would include providing a set of measured scattering parameters for an arbitrary (lossy and dispersive) transmission line over a wide frequency range (up to 18 GHz). Time-domain Green's functions can then be numerically computed and used to calculate the associated response.

VI. Conclusions

This study explored some important aspects of interconnections for digital and microwave applications. The problems of losses, dispersion, and load nonlinearities were analyzed. A simple algorithm was derived for the simulation of an arbitrary time-domain signal on a structure having all the above properties. The algorithm assumed that the frequency-dependent characteristics of the line were available as well as large-signal models for the terminations. Future work includes the derivation of a suitable loss and dispersion model and the extension of the algorithm for modeling n-line multiconductor systems.

References

[1] W. J. Getsinger, "Microstrip dispersion model," *IEEE Trans. Microwave Theory Tech.*, vol. MTT-21, pp. 34–39, Jan. 1973.

[2] W. J. Getsinger, "Measurement and modeling of the apparent characteristic impedance of microstrip," *IEEE Trans. Microwave Theory Tech.*, vol. MTT-31, pp. 624–632, Aug. 1983.

[3] P. Bhartia and P. Pramanick, "New microstrip dispersion model," *IEEE Trans. Microwave Theory Tech.*, vol. MTT-32, pp. 1379–1384, Oct. 1984.

[4] H. J. Carlin, "A simplified circuit model for microstrip," *IEEE Trans. Microwave Theory Tech.*, vol. MTT-21, pp. 589–591, Sept. 1973.

[5] E. J. Denlinger, "A frequency dependent solution for microstrip transmission lines," *IEEE Trans. Microwave Theory Tech.*, vol. MTT, pp. 30–39, Jan. 1971.

[6] T. Itoh and R. Mittra, "Spectral-domain approach for calculating the dispersion characteristics of microstrip lines," *IEEE Trans. Microwave Theory Tech.*, vol. MTT-21, pp. 496–499, July 1973.

[7] R. Mittra and T. Itoh, "New technique for the analysis of the dispersion characteristics of microstrip lines," *IEEE Trans. Microwave Theory Tech.*, vol. MTT-19, pp. 47–56, Jan. 1971.

[8] E. F. Kuester and D. C. Chang, "Theory of dispersion in microstrip of arbitrary width," *IEEE Trans. Microwave Theory Tech.*, vol. MTT-28, pp. 259–265, Mar. 1980.

[9] M. Hashimoto, "A rigorous solution for dispersive microstrip," *IEEE Trans. Microwave Theory Tech.*, vol. MTT-33, pp. 1131–1137, Nov. 1985.

[10] T. C. Edwards and R. P. Owens, "2–18 GHz dispersion measurement on 10–100 Ω microstrip lines on sapphire," *IEEE Trans. Microwave Theory Tech.*, vol. MTT-24, pp. 506–513, Aug. 1976.

[11] A. R. Djordjevic, T. K. Sarkar, and R. F. Harrington, "Analysis of transmission lines with arbitrary nonlinear terminal networks," *IEEE Trans. Microwave Theory Tech.*, vol. MTT-21, pp. 660–666 June 1986.

[12] H. Mohammadian and C. T. Tai, "A general method of transient analysis for lossless transmission lines and its analytical solution to time-varying resistive terminations," *IEEE Trans. Antennas Propagat.*, vol. AP-32 pp. 309–312, Mar. 1984.

[13] R. L. Veghte and C. A. Balanis, "Dispersion of transient signals in microstrip transmission lines," *IEEE Trans. Microwave Theory Tech.*, vol. MTT-34, pp. 1427–1436, Dec. 1986.

[14] S. Caniggia, "EMC design of digital systems using macromodeling procedures for integrated circuits and their interconnections," in *Proc. EMC Symp.*, 1983, pp. 465–470.

[15] L. O. Chua and P. M. Lin, *Computer-Aided Analysis of Electronic Circuits*. Englewood Cliffs, NJ: Prentice Hall, 1975.

[16] D. K. Ferry, J. M. Golio, and R. O. Grondin, "Interconnections and limitations in VLSI," in *Proc. VLSI Multilevel Interconnection Conf.*, 1985, pp. 408–415.

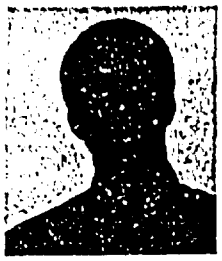

Jose E. Schutt-Aine (S'87) [redacted] He received the B.S. degree in electrical engineering from the Massachusetts Institute of Technology, Cambridge, in 1981. From 1981 to 1983, he worked at the Hewlett-Packard Technology Center in Santa Rosa, CA. He received the M.S. degree in electrical engineering from the University of Illinois, Urbana, in 1984 and is currently pursuing the Ph.D. degree at the same institution.

Raj Mittra (S'54–M'57–SM'69–F'71) is the Director of the Electromagnetic Communication Laboratory of the Electrical and Computer Engineering Department and Research Professor of the Coordinated Science Laboratory at the University of Illinois. He is a Past-President of the IEEE Antennas and Propagation Society. He serves as a consultant to several industrial and governmental organizations in the United States.

His professional interests include the areas of analytical and computer-aided electromagnetics, high-speed digital circuits, radar scattering, satellite antennas, microwave and millimeter-wave integrated circuits, frequency selective surfaces, EMP and EMC analysis, and the interaction of electromagnetic waves with biological media.